



NAVAL
POSTGRADUATE
SCHOOL

MONTEREY, CALIFORNIA

DISSERTATION

**LATTICE BOLTZMANN METHODS FOR FLUID
STRUCTURE INTERACTION**

by

Stuart R. Blair

September 2012

Dissertation Supervisor:

Young Kwon

Approved for public release; distribution is unlimited

THIS PAGE INTENTIONALLY LEFT BLANK

REPORT DOCUMENTATION PAGE			Form Approved OMB No. 0704-0188	
Public reporting burden for this collection of information is estimated to average 1 hour per response, including the time for reviewing instruction, searching existing data sources, gathering and maintaining the data needed, and completing and reviewing the collection of information. Send comments regarding this burden estimate or any other aspect of this collection of information, including suggestions for reducing this burden, to Washington headquarters Services, Directorate for Information Operations and Reports, 1215 Jefferson Davis Highway, Suite 1204, Arlington, VA 22202-4302, and to the Office of Management and Budget, Paperwork Reduction Project (0704-0188) Washington DC 20503.				
1. AGENCY USE ONLY (Leave blank)		2. REPORT DATE September 2012	3. REPORT TYPE AND DATES COVERED Dissertation	
4. TITLE AND SUBTITLE: Lattice Boltzmann Methods for Fluid Structure Interaction			5. FUNDING NUMBERS	
6. AUTHOR(S): Stuart R. Blair				
7. PERFORMING ORGANIZATION NAME(S) AND ADDRESS(ES)			8. PERFORMING ORGANIZATION REPORT NUMBER	
9. SPONSORING/MONITORING AGENCY NAME(S) AND ADDRESS(ES)			10. SPONSORING/MONITORING AGENCY REPORT NUMBER	
11. SUPPLEMENTARY NOTES: The views expressed in this thesis are those of the author and do not reflect the official policy or position of the Department of Defense or the U.S. Government. IRB Protocol Number: NA.				
12a. DISTRIBUTION / AVAILABILITY STATEMENT Approved for public release; distribution is unlimited			12b. DISTRIBUTION CODE A	
13. ABSTRACT (maximum 200 words) The use of lattice Boltzmann methods (LBM) for fluid flow and its coupling with finite element method (FEM) structural models for fluid-structure interaction (FSI) is investigated. A body of high performance LBM software that exploits graphic processing unit (GPU) and multiprocessor programming models is developed and validated against a set of two- and three-dimensional benchmark problems. Computational performance is shown to exceed recently reported results for single-workstation implementations over a range of problem sizes. A mixed-precision LBM collision algorithm is presented that retains the accuracy of double-precision calculations with less computational cost than a full double-precision implementation. FSI modelling methodology and example applications are presented along with a novel heterogeneous parallel implementation that exploits task-level parallelism and workload sharing between the central processing unit (CPU) and GPU that allows significant speedup over other methods. Multi-component LBM fluid models are explicated and simple immiscible multi-component fluid flows in two-dimensions are presented. These multi-component fluid LBM models are also paired with structural dynamics solvers for two-dimensional FSI simulations. To enhance modeling capability for domains with complex surfaces, a novel coupling method is introduced that allows use of both classical LBM (CLBM) and a finite element LBM (FELBM) to be combined into a hybrid LBM that exploits the flexibility of FELBM while retaining the efficiency of CLBM.				
14. SUBJECT TERMS lattice Boltzmann method, fluid-structure interaction			15. NUMBER OF PAGES 161	
			16. PRICE CODE	
17. SECURITY CLASSIFICATION OF REPORT Unclassified	18. SECURITY CLASSIFICATION OF THIS PAGE Unclassified	19. SECURITY CLASSIFICATION OF ABSTRACT Unclassified	20. LIMITATION OF ABSTRACT UU	

THIS PAGE INTENTIONALLY LEFT BLANK

Approved for public release; distribution is unlimited

LATTICE BOLTZMANN METHODS FOR FLUID STRUCTURE INTERACTION

Stuart R. Blair
Commander, United States Navy
B.S., United States Naval Academy, 1994
M.S., Massachusetts Institute of Technology, 2003
Nuclear Eng., Massachusetts Institute of Technology, 2003

Submitted in partial fulfillment of the
requirements for the degree of

**DOCTOR OF PHILOSOPHY IN
MECHANICAL ENGINEERING**

from the

**NAVAL POSTGRADUATE SCHOOL
September 2012**

Author:

Stuart R. Blair

Approved By:

Young W. Kwon
Distinguished Professor
Dept. of Mech. & Aero. Engineering
Dissertation Committee Chair

Garth V. Hobson
Professor
Dept. of Mech. & Aero. Engineering

Joshua H. Gordis
Associate Professor
Dept. of Mech. & Aero. Engineering

Clyde L. Scandrett
Professor
Dept. of Applied Mathematics

Francis X. Giraldo
Professor
Dept. of Applied Mathematics

Approved By:

Knox T. Millsaps, Professor & Chair, Dept. of Mechanical & Aerospace Engineering

Approved By:

Doug Moses, Vice Provost for Academic Affairs

THIS PAGE INTENTIONALLY LEFT BLANK

ABSTRACT

The use of lattice Boltzmann methods (LBM) for fluid flow and its coupling with finite element method (FEM) structural models for fluid-structure interaction (FSI) is investigated. A body of high performance LBM software that exploits graphic processing unit (GPU) and multiprocessor programming models is developed and validated against a set of two- and three-dimensional benchmark problems. Computational performance is shown to exceed recently reported results for single-workstation implementations over a range of problem sizes. A mixed-precision LBM collision algorithm is presented that retains the accuracy of double-precision calculations with less computational cost than a full double-precision implementation. FSI modelling methodology and example applications are presented along with a novel heterogeneous parallel implementation that exploits task-level parallelism and workload sharing between the central processing unit (CPU) and GPU that allows significant speedup over other methods. Multi-component LBM fluid models are explicated and simple immiscible multi-component fluid flows in two-dimensions are presented. These multi-component fluid LBM models are also paired with structural dynamics solvers for two-dimensional FSI simulations. To enhance modeling capability for domains with complex surfaces, a novel coupling method is introduced that allows use of both classical LBM (CLBM) and a finite element LBM (FELBM) to be combined into a hybrid LBM that exploits the flexibility of FELBM while retaining the efficiency of CLBM.

THIS PAGE INTENTIONALLY LEFT BLANK

TABLE OF CONTENTS

I.	INTRODUCTION	1
A.	OBJECTIVES AND ORGANIZATION	1
B.	STATEMENT OF CONTRIBUTIONS	3
II.	LATTICE BOLTZMANN METHOD	5
A.	LITERATURE REVIEW AND INTRODUCTION	6
B.	LATTICE STRUCTURES	7
C.	MULTIPLE RELAXATION TIME COLLISION OPERATOR . .	11
D.	BOUNDARY CONDITIONS	14
1.	Periodic Boundaries	15
2.	Solid Boundaries	16
3.	Moving Solid Boundaries	17
4.	Prescribed Velocity or Pressure Boundaries	18
a.	Zou-He Boundaries	19
b.	Regularized Boundaries	21
E.	BODY FORCES	22
F.	SCALING	23
G.	EXAMPLE	24
1.	Problem Description	24
2.	Scaling and Setup	24
a.	Viscosity Scaling	26
b.	Velocity BC Scaling	26
c.	Pressure BC Scaling	27
3.	Initialization and Lattice Point Classification	27
4.	Time-Stepping	28
III.	IMPLEMENTATION AND VALIDATION	31
A.	POISEUILLE FLOW	31
1.	Solution with On-Grid Bounceback Boundary Conditions .	33
2.	Solution with Half-Way Bounceback Boundary Conditions	33
3.	Stability and Accuracy	36
B.	BACKWARD FACING STEP	39
C.	LID-DRIVEN CAVITY	42
D.	CHANNEL FLOW OVER CYLINDER	46

IV.	LBM IMPLEMENTATION ON GRAPHICS PROCESSING UNITS . . .	51
A.	COMPUTATIONAL REQUIREMENTS FOR THE LBM	51
B.	AN OVERVIEW OF GPUS AND NVIDIA CUDA	53
1.	NVIDIA GPU Architecture	53
2.	CUDA C Programming Model	55
C.	LBM IMPLEMENTATION WITH CUDA	58
1.	Basic Implementation	59
a.	LBM Routine	59
b.	Data Layout	60
2.	Optimization	62
a.	Kernel Structure	62
b.	Registers versus Shared Memory	63
c.	Thread Block Dimensions	64
D.	PERFORMANCE BENCHMARK–3D LID-DRIVEN CAVITY . .	66
E.	HYBRID PARALLEL LBM	68
1.	CUDA with OpenMP	70
2.	CUDA with MPI	70
V.	FLUID-STRUCTURE INTERACTION WITH LBM	75
A.	INTRODUCTION AND LITERATURE REVIEW	75
B.	FORCE EVALUATION	76
1.	Stress Integration Approach	77
2.	Momentum Response Approach	78
C.	COUPLING PROCEDURE	79
D.	FLUID-STRUCTURE INTERACTION IN TWO DIMENSIONS .	80
1.	Structural Model	80
2.	Fluid Models	81
3.	Converging-Diverging Channel	81
4.	Lid-Driven Cavity	86
5.	Cylinder with Fin Benchmark	88
E.	FLUID-STRUCTURE INTERACTION IN THREE DIMENSIONS	90
F.	HETEROGENEOUS PARALLEL IMPLEMENTATION	90
VI.	HYBRID LATTICE BOLTZMANN METHOD	95
A.	INTRODUCTION AND LITERATURE REVIEW	95
B.	FINITE ELEMENT LBM	96
C.	HYBRID CLBM/FELBM METHODOLOGY	98
D.	NUMERICAL RESULTS AND DISCUSSION	101

VII.	LBM FOR MULTI-COMPONENT FLUIDS	109
A.	MULTI-COMPONENT FLUID MODELS	109
1.	Color-Fluid Model	109
2.	Free-Energy Model	110
3.	Mean-Field Theory Model	110
4.	Inter-Particle Potential Model	111
B.	IMMISCIBLE MULTI-COMPONENT LBM PROCEDURES . .	112
1.	Time Stepping	113
2.	Boundary Conditions	114
C.	EXAMPLE APPLICATIONS	115
1.	Component Separation	115
2.	Lid-Driven Cavity	115
a.	Case 1	116
b.	Case 2	117
3.	Lid-Driven Cavity with FSI	117
VIII.	CONCLUSIONS AND FUTURE WORK	125
A.	CONCLUSIONS	125
B.	FUTURE WORK	126
	LIST OF REFERENCES	129
	INITIAL DISTRIBUTION LIST	139

THIS PAGE INTENTIONALLY LEFT BLANK

LIST OF FIGURES

Figure 1.	The D2Q9 lattice.	7
Figure 2.	Commonly used lattice topologies for LBM in three dimensions. . . .	8
Figure 3.	Schematic of lattice point on west domain boundary.	15
Figure 4.	Streaming of f_2 across a North/South periodic boundary.	15
Figure 5.	Application of on-grid bounce-back boundary condition.	16
Figure 6.	Half-way bounceback solid boundary condition schematic.	17
Figure 7.	Groups of density distributions on west boundary lattice point. . . .	19
Figure 8.	Scaling from physical units, to dimensionless units to LBM units. . .	24
Figure 9.	Schematic diagram of channel flow example problem.	25
Figure 10.	LBM time step flowchart.	29
Figure 11.	Velocity magnitude, pressure, and vorticity magnitude for example flow case after 50,000 time steps.	30
Figure 12.	Poiseuille flow configuration.	32
Figure 13.	Poiseuille flow convergence with On-Grid bounce-back boundary con- ditions.	34
Figure 14.	Poiseuille flow convergence with half-way bounce-back boundary con- ditions in single precision.	35
Figure 15.	Poiseuille flow convergence with half-way bounce-back boundary con- ditions in double precision.	35
Figure 16.	Poiseuille flow convergence with half-way bounce-back boundary con- ditions using mixed-precision arithmetic.	36
Figure 17.	Relative performance of single precision (SP), mixed precision (MP) and double precision (DP) computational routines for Poiseuille flow. The lattice refinement parameter refers to the number of lattice points placed across in the dimension of the channel opening.	37
Figure 18.	Stabilization time for Poiseuille flow, $Re=10$, $\frac{1}{\tau} = \omega = 1.3$. Top figure, $N_y=30$, bottom figure, $N_y=480$	38
Figure 19.	Backward step flow separation behavior. Image taken from [34] . . .	40
Figure 20.	Schematic of domain and boundary conditions for Backward-Step benchmark in 2D.	40
Figure 21.	Backward-Step simulation. Step height = 0.25m, outlet width=0.5m, $Re=100$	41
Figure 22.	Comparison of primary vortex re-attachment length normalized by step height with results reported in [35].	41

Figure 23.	Schematic of the two-dimensional lid-driven cavity problem.	42
Figure 24.	Lid-driven cavity in two dimensions with 1600x1600 lattice showing from left-to-right streamlines, vorticity contours and pressure contours for $Re=1000$. Top set of figures is LBM from this work. Bottom set of figures is from [36].	43
Figure 25.	Lid-driven cavity in two dimensions with 1600x1600 lattice showing from left-to-right streamlines, vorticity contours and pressure contours for $Re=5000$. Top set of figures is LBM, bottom set of figures is from [37].	43
Figure 26.	Comparison of velocity, pressure and vorticity to benchmark values for $Re=1000$	45
Figure 27.	Channel with cylindrical obstacle 2D problem.	46
Figure 28.	Streamline visualization of trailing vortex at $Re=20$ (top) and $Re=40$ (bottom).	47
Figure 29.	Vorticity plot for cylinder in 2D flow at $Re=100$	48
Figure 30.	Drag and lift coefficient for cylinder in uniform flow. $Re=100$	49
Figure 31.	Strouhal number computed from the energy spectra of the lift coefficient at $Re=100$	49
Figure 32.	Historical trends for CPU and GPU memory bandwidth and compute performance (From [52]).	52
Figure 33.	Memory bandwidth requirement versus desired computational throughput for a typical LBM implementation. Modern CPU and GPU hardware are memory bandwidth limited for LBM.	53
Figure 34.	Simplified schematic of NVIDIA GPU.	54
Figure 35.	Hierarchy of threads in a CUDA program. Threads are organized into blocks; blocks are organized into a grid (From [52]).	55
Figure 36.	Schematic of data layout schemes. (a) depicts the array of structures (AoS), (b) depicts the structure of arrays (SoA). Superscripts indicate lattice node number, subscripts indicate the lattice velocity.	61
Figure 37.	When using SoA, load instructions executed by consecutive threads read from consecutive locations in memory	61
Figure 38.	Schematic of the dual lattice scheme used to support a unified time step kernel. On even time steps, the Even Lattice is active and it collides and streams to the Odd Lattice; vice versa for odd time steps.	63
Figure 39.	LBM performance on GTX-580 for three-dimension lid-driven cavity as a function of threads per block.	65
Figure 40.	Performance benchmark for lattice Boltzmann method (LBM) on a 3D lid-driven cavity scaled for device memory bandwidth.	67

Figure 41.	LBM on a 3D lid-driven cavity with various number of threads per block.	69
Figure 42.	Lid-driven cavity using a D3Q15 lattice with 500^3 points using CUDA and OpenMP.	71
Figure 43.	Schematic LBM time step for distributed computing with MPI. Scalability is achieved by interleaving communication with computation. .	72
Figure 44.	Weak scaling using MPI for LBM simulation of three-dimensional Poiseuille flow.	73
Figure 45.	Weak scaling using CUDA and MPI for LBM simulation of three-dimensional Poiseuille flow.	74
Figure 46.	Euler-Bernoulli Beam.	80
Figure 47.	Schematic of 2D converging and diverging duct.	82
Figure 48.	Converging and diverging duct displacement, velocity and acceleration at beam midpoint. $Re = 5$, glycerin with cork beam.	83
Figure 49.	Converging and diverging duct with combined beam response. $Re=5$, glycerin with cork beam.	84
Figure 50.	Converging and diverging duct with varying fluid viscosity. Starting from top left, fluid viscosity is $\frac{\nu_{\text{glycerin}}}{4}$, $\frac{\nu_{\text{glycerin}}}{2}$ and ν_{glycerin}	85
Figure 51.	Converging and diverging duct with varying beam elastic modulus. From left to right elastic modulus is $\frac{E_{\text{cork}}}{2}$ and E_{cork}	85
Figure 52.	Schematic diagram of lid-driven cavity FSI problem geometry.	86
Figure 53.	Results for two-dimensional lid-driven cavity.	87
Figure 54.	Final bottom displacement.	88
Figure 55.	Cylinder with elastic fin benchmark	88
Figure 56.	Results for two-dimensional cylinder with elastic trailing fin at $Re=200$. .	89
Figure 57.	Displacement, velocity and acceleration for cylinder with elastic fin. $Re=200$	91
Figure 58.	Illustration of task-level decomposition in parallel implementation of FSI problem. In the lower figure, a further level of task-level parallelism is exploited by overlapping the structural dynamics computation on the CPU with LBM calculations on domain areas remote from the elastic structure on the GPU.	92
Figure 59.	Decomposition of FSI problem domain for task-level heterogeneous parallelism.	93
Figure 60.	Schematic of Hybrid LBM time step. Methodology differs only in implementation of the particle streaming phase.	99

Figure 61.	Schematic Hybrid Lattice on regular domain. Assignment following streaming in the CLBM domain and advection in the FELBM domain is only made to the interior of each respective sub-domain. Data drawn from the lattice points on the halo facilitates communication between each sub-domain.	99
Figure 62.	Interface region for CLBM and FELBM domains on a uniform mesh. Lattice points with both the asterisk and circle belong to the interface.	100
Figure 63.	Mid-channel normalized velocity profile for Poiseuille flow using CLBM, FELBM and HLBM.	102
Figure 64.	Hybrid lattice mesh around a circular obstacle. Lattice points with asterisk are in the CLBM sub-domain, those circled are in the FELBM sub-domain. Those with both markings are members of the interface halo of the two regions.	103
Figure 65.	Normalized velocity contour plot for fluid flow around circular obstacle at Reynolds number = 5 using CLBM	104
Figure 66.	Normalized velocity contour plot for fluid flow around circular obstacle at Reynolds number = 5 using Hybrid LBM.	105
Figure 67.	Normalized velocity profile at 30 percent channel length, Reynolds number = 5.	106
Figure 68.	Normalized velocity profile at 60 percent channel length, Reynolds number = 5.	107
Figure 69.	Schematic Hybrid Lattice on regular domain. Assignment following streaming in the CLBM domain and advection in the FELBM domain is only made to the interior of each respective sub-domain. Data drawn from the lattice points on the halo facilitates communication between each sub-domain.	108
Figure 70.	Illustration of inter-particle forces in the nearest neighborhood of a lattice point.	112
Figure 71.	Two immiscible components. $G = -1.2$	115
Figure 72.	Two immiscible components. $G = -0.2$. Note that the weak interaction parameter renders the fluids miscible.	116
Figure 73.	Density for Fluid 1 of a two-component immiscible fluid flow in a lid-driven cavity. Initial configuration.	117
Figure 74.	Fluid 1 results for a two-component immiscible fluid flow in a lid-driven cavity. Sequence of images shows flow progression from top to bottom corresponding respectively to early in the simulation to its final steady state.	118

Figure 75.	Fluid 1 results for a two-component immiscible fluid flow in a lid driven cavity. The higher viscosity and density of fluid 2 results in its confinement in the bottom-half of the cavity domain.	119
Figure 76.	Fluid 1 results for a two-component immiscible fluid flow in a lid driven cavity. The higher viscosity and density of fluid 2 results in its confinement in the bottom-half of the cavity domain.	119
Figure 77.	Schematic representation of a lid-driven cavity with an elastic beam attached to the lower surface.	120
Figure 78.	Single-component fluid flow in cavity with beam. Streamlines show development of three distinct vortex regions.	121
Figure 79.	Momentum and density fields for fluid 1 at steady-state; $Re=1000$. . .	122
Figure 80.	Plot of displacement, velocity and acceleration at the tip of the elastic beam.	122
Figure 81.	Final beam displacement for multi-component FSI. Beam displacement is magnified 10 times for clarity.	123

THIS PAGE INTENTIONALLY LEFT BLANK

LIST OF TABLES

Table 1.	Geometry and fluid parameters for Poiseuille flow test case.	32
Table 2.	Comparison of trailing vortex length to benchmark values.	46
Table 3.	Comparison of Strouhal number to benchmark values.	48
Table 4.	Memory bandwidth of various CUDA memory spaces on an NVIDIA GTX-580 GPU	64
Table 5.	Properties of GPU devices used in benchmark computations in Figure 40	67
Table 6.	Selected structural material properties used for fluid-structure interaction (FSI) simulations.	81
Table 7.	Selected fluid properties for FSI simulations.	81
Table 8.	Performance improvement from using overlapped execution depicted in lower half of Figure 58 versus the non-overlapped scheme in the top half of Figure 58. The lattice was 22 x 337 x 526 D3Q19 using MRT collision operator. The structural model was a sheer-deformable plate with 2883 degrees of freedom.	94
Table 9.	Performance comparison of CLBM and FELBM.	106

THIS PAGE INTENTIONALLY LEFT BLANK

LIST OF ACRONYMS AND NOMENCLATURE

API	application programming interface
AoS	array of structures
BGK	Bhatnagar-Gross-Krook
CLBM	classical lattice Boltzmann method
CUDA	Compute Unified Device Architecture
DEM	discrete element method
LBM	lattice Boltzmann method
FELBM	finite element lattice Boltzmann method
FEM	finite element method
FSI	fluid-structure interaction
FVM	finite volume method
GB	gigabytes
GFLOPS	billion floating point operations per second
GPU	graphical processing unit
HLBM	hybrid lattice Boltzmann method
IB	immersed boundary
LBGK	lattice Bhatnagar-Gross-Krook
MPI	message passing interface
MRT	multiple relaxation time
SM	Streaming Multiprocessor
SP	Scalar Processors
SoA	structure of arrays
VTK	Visualization Toolkit

c_s	lattice Boltzmann method lattice sound speed
\mathbf{e}_α	lattice velocity
f_α	particle density distribution function
f_α^{eq}	equilibrium density distribution function
\mathbf{M}	particle moment transformation operator
ν	kinematic viscosity
Ω_α	collision operator
p	macroscopic pressure
ρ	macroscopic density
\mathbf{R}	particle moment space
\mathbf{S}	multiple relaxation time relaxation matrix
τ	relaxation time
\mathbf{u}	macroscopic velocity
ω	single relaxation-time relaxation operator
w_α	lattice weight

I. INTRODUCTION

The present thesis investigates the use of the lattice Boltzmann method (LBM) to solve for the flow of viscous, incompressible fluids while accounting for the effect these fluid flows have on surrounding elastic structures. From waves slapping against ship structural members, cooling water passing over heat-exchanger tubes to blood flowing within veins and arteries among many others, FSI has applications that span the engineering and life sciences. Towards the goal of simulating such physical behavior, several intermediate steps were required. These intermediate steps start with the development of a robust and highly capable software tool for simulating and analyzing flow of incompressible viscous fluids and continue through to integration of these tools with structural dynamics solvers.

A. OBJECTIVES AND ORGANIZATION

The first objective is to develop software tools required for a LBM flow solver that can reliably and accurately simulate fluid flow problems of interest. The theory and formulation of the LBM, including detailed considerations of stability, accuracy and proper scaling of simulation variables to allow modeling of specific fluid systems is provided in Chapter II.

With a detailed understanding of the theory, software tools can be developed to simulate fluid flows of interest. Such software is developed and subjected to a collection of validation benchmarks in Chapter III. The second-order convergence of the LBM along with select boundary conditions is demonstrated along with a demonstration of the potential impacts of the wide use of single-precision arithmetic on this convergence rate. A mixed-precision LBM implementation is introduced that provides for second-order convergence for select boundary conditions while retaining some of the performance benefits of using single precision number representation and arithmetic.

In order to increase the accuracy of a LBM simulation, the spatial and temporal discretization is refined. Smaller time steps and a more refined lattice both lead to increased computational demand. In order to execute LBM simulations in a reasonable amount of time, the programs are written to be executed in parallel. In Chapter IV the Compute Unified Device Architecture (CUDA) programming model is introduced and the implementation of the LBM programs for parallel execution on a graphical processing unit (GPU) is described. The achieved performance is compared with recently published benchmarks. Two hybrid programming models are also demonstrated that use a combination of CUDA and OpenMP in one case and CUDA and message passing interface (MPI) in another. Collectively, Chapter IV describes the development of a scalable high-performance LBM solver.

Once reliable fluid simulation tools are in place, the second objective is to couple this fluid solver with an appropriate structural dynamics model. These software components are then used as coupled FSI simulation tools. The key ingredients of computing forces and moments along the fluid-structure interface and accounting for their exchange and integrating with a structural dynamics solver for a coordinated FSI simulation are discussed. The specific methods and algorithms for doing this along with example applications in both two and three dimensions are presented in Chapter V.

The aforementioned software tools were all developed based on the classical LBM theory. A recently developed modification, termed the finite element lattice Boltzmann method (FELBM), allows use of unstructured non-uniform finite element grids in lieu of the regular structured grid from classical lattice Boltzmann method (CLBM). The FELBM gains this flexibility at the expense of some computational efficiency on a per-lattice-point basis. An algorithm and associated software tool has been developed resulting in a hybrid lattice Boltzmann method (HLBM) whereby both CLBM and FELBM are used on disjoint sub-domains of an overall simulation. This hybrid tool leverages the simplicity and efficiency of the CLBM while also benefiting from the geometric flexibility of the FELBM. The overall system is able to simulate fluid flow over the combined domain with less com-

putational effort than the FELBM while reducing the memory requirements of an equivalent simulation using only CLBM. The theory and algorithms for accomplishing this is provided in Chapter VI.

The last objective of this model is to take advantage of the flexible and physically intuitive methods for modeling multi-component fluid systems using LBM. A discussion of the standard LBM theory for multi-component fluids as well as example problems in fluid flow and FSI are demonstrated in Chapter VII.

In Chapter VIII, conclusions and prospects for future research are discussed.

B. STATEMENT OF CONTRIBUTIONS

The principal contributions of this thesis are:

- A body of software tools that provide LBM modeling capability for single-component incompressible viscous flows in two and three dimensions.
- A new mixed-precision LBM implementation that retains most of the accuracy of double precision while requiring only the memory of single precision.
- A GPU-accelerated implementation of LBM with highly competitive performance against recently published benchmarks.
- A new method to simulate two-way FSI that exploits task-level concurrency for a heterogeneous-parallel algorithm using both GPU for the fluid domain and central processing units for the solid domain.
- A novel method for combining CLBM and FELBM into a HLBM.
- LBM flow and FSI modeling capability for multi-component flows in two dimensions.

THIS PAGE INTENTIONALLY LEFT BLANK

II. LATTICE BOLTZMANN METHOD

The LBM is an increasingly popular way to simulate fluid flow. In contrast to more conventional methods such as finite difference methods (FDM) control volume methods (CVM) and finite element methods (FEM), the LBM begins not with the picture of the fluid as a continuous medium, but instead as a collection of particles. These particles move and undergo local interactions with other particles in accordance with simple rules. Macroscopic physical phenomena such as those conservation laws described by the Navier-Stokes equations emerge from the large number of these local interactions. The microscopic level of description provides an intuitive basis for generalization to complex systems such as porous media ([1]-[3]), two-phase flow ([4]-[6]) and magnetohydrodynamics ([7]-[9]) among others. By judiciously altering the formulation, other partial differential equations of interest have been modeled by a similar procedure including the Burgers Equation [10], the Korteweg-de Vries equation [11], the Brinkman equation [12] and the Schrödinger equation [13]. For a concise review of the current state of the art in LBM, an excellent survey can be found in [14] with a recent update in [15]. A recently published analysis of LBM theory, which includes a thorough critique and comparison with traditional computational fluid dynamics techniques, can be found at [16]. In this work, the LBM will be used for the solution of the Navier-Stokes equations for single-component fluid flows as well as a limited number of multi-component fluid flows.

This chapter will start with a brief overview of the historical development of the LBM. This will be followed by a description of each element of a LBM simulation including typical lattice structures with lattice velocities and associated weights, collision operators, boundary conditions, body forces and scaling requirements. The chapter will be concluded with a detailed example application of the LBM to two-dimensional channel flow over a cylindrical obstacle.

A. LITERATURE REVIEW AND INTRODUCTION

Historically, the LBM is derived from the concepts of the cellular automaton [17], [18]. Space is described by a regular array of interconnecting lattice sites and time is divided into equally spaced time-steps. The cellular automata model is specified by stating the rules by which each lattice site shall be updated for the next time step. Depending on these rules, complex physical phenomena emerge [19]. A classical example of complex behavior emerging from simple rules is Conway’s Game of Life. In some cases, the CA with associated sets of update rules have become useful as a model for real physical behavior and have become a means to gaining more fundamental understanding. Examples include traffic flow [20], population dynamics [21], and earthquake prediction [22] to name but a few.

The CA model underlying a fluid dynamics model incorporates movement of particles from one lattice site to another along discrete lattice directions. The rule for lattice site update is applied to all particles arriving at a given lattice site in a given time step and is represented formally in Equation 1,

$$N_{\alpha}(\mathbf{x} + \delta_x \mathbf{e}_{\alpha}, t + \delta_t) = N_{\alpha}(\mathbf{x}, t) + \Omega_{\alpha}(N) \quad (1)$$

where N_{α} is a Boolean variable indicating the presence or absence of a fluid particle traveling along lattice direction \mathbf{e}_{α} at position \mathbf{x} . The rules for update—referred to as the Collision Operator—are formally denoted by $\Omega_{\alpha}(N)$. One advantage of this formulation using Boolean variables is the absence of round-off errors; all arithmetic is exact. Unfortunately, though the mathematical operations are simple and exact, it has been found that they are required in enormous numbers to overcome statistical noise in the results. Additionally, it has been found that further lattice symmetry requirements need to be met in order to provide Galilean invariance.

The LBM emerged from the solutions presented to these difficulties [18], [23]. The LBM seeks to solve the discrete Boltzmann equation which, in the absence of external

forces is:

$$\frac{\partial f_\alpha}{\partial t} + \mathbf{e}_\alpha \cdot \nabla f_\alpha = \Omega_\alpha, \quad \alpha \in [0, \dots, q], \quad \mathbf{e}_\alpha \in \mathbb{R}^d \quad (2)$$

where f_α is the particle velocity distribution function for lattice direction α ; \mathbf{e}_α is the set of lattice velocities; and Ω_α is the collision operator. Additionally, initial values for all f_α must be supplied on the problem domain and boundary conditions must be applied appropriately. In the following sections, each of these issues will be addressed in turn so that a simulation of fluid flow may be undertaken using the LBM.

B. LATTICE STRUCTURES

In the LBM, this solution is sought on a regular lattice. A lattice is defined by a sound speed c_s , a set of d -dimensional lattice velocities \mathbf{e}_α where $\alpha \in [0, \dots, q]$ and a set of weights w_α . The usual notation to specify a lattice is given as $DdQq$. A lattice commonly used in two dimensions has nine velocities and is denoted D2Q9 and is illustrated in Figure 1. The sound speed, weights and lattice velocities for this model are given in Equation 3.

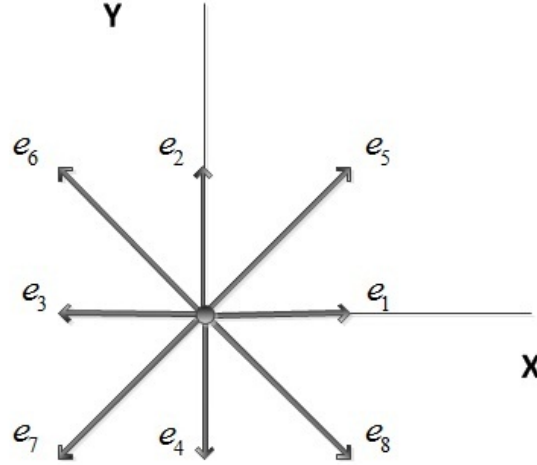


Figure 1: The D2Q9 lattice.

$$\begin{aligned}
c_s^2 &= \frac{1}{3} \\
w_0 &= \frac{2}{9} & w_{1-4} &= \frac{1}{9} & w_{5-8} &= \frac{1}{36} \\
\mathbf{e}_0 &= (0, 0) \\
\mathbf{e}_1 &= (1, 0) & \mathbf{e}_2 &= (0, 1) & \mathbf{e}_3 &= (-1, 0) & \mathbf{e}_4 &= (0, -1) \\
\mathbf{e}_5 &= (1, 1) & \mathbf{e}_6 &= (-1, 1) & \mathbf{e}_7 &= (-1, -1) & \mathbf{e}_8 &= (1, -1)
\end{aligned} \tag{3}$$

Commonly used lattices for three-dimensional problems are shown in Figure 2. Sets of lattice speeds are given for the $D3Q15$ lattice are given in Equation 4, and those for the $D3Q19$ and $D3Q27$ are shown respectively in Equations 5 and 6.

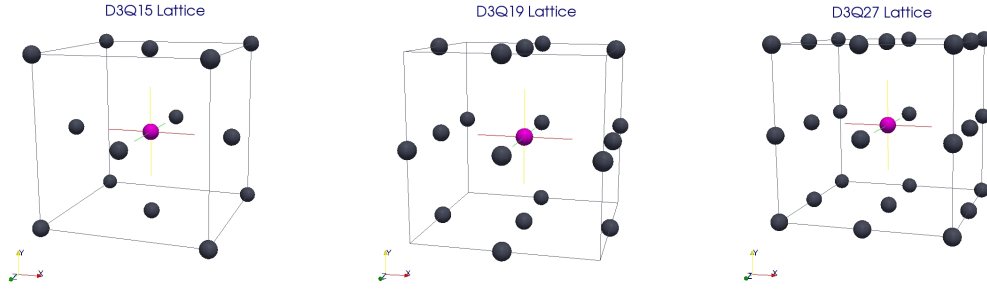


Figure 2: Commonly used lattice topologies for LBM in three dimensions.

$$\begin{aligned}
c_s^2 &= \frac{1}{3} \\
w_0 &= \frac{2}{9} & w_{1-6} &= \frac{1}{9} & w_{7-14} &= \frac{1}{72} \\
\mathbf{e}_0 &= (0, 0, 0) & \mathbf{e}_1 &= (1, 0, 0) & \mathbf{e}_2 &= (-1, 0, 0) & \mathbf{e}_3 &= (0, 1, 0) \\
\mathbf{e}_4 &= (0, -1, 0) & \mathbf{e}_5 &= (0, 0, 1) & \mathbf{e}_6 &= (0, 0, -1) & \mathbf{e}_7 &= (1, 1, 1) \\
\mathbf{e}_8 &= (-1, 1, 1) & \mathbf{e}_9 &= (1, -1, 1) & \mathbf{e}_{10} &= (-1, -1, 1) & \mathbf{e}_{11} &= (1, 1, -1) \\
\mathbf{e}_{12} &= (-1, 1, -1) & \mathbf{e}_{13} &= (1, -1, -1) & \mathbf{e}_{14} &= (-1, -1, -1)
\end{aligned} \tag{4}$$

$$\begin{aligned}
c_s^2 &= \frac{1}{3} \\
w_0 &= \frac{1}{3} & w_{1-6} &= \frac{1}{18} & w_{7-19} &= \frac{1}{36} \\
\mathbf{e}_0 &= (0, 0, 0) & \mathbf{e}_1 &= (1, 0, 0) & \mathbf{e}_2 &= (-1, 0, 0) & \mathbf{e}_3 &= (0, 1, 0) \\
\mathbf{e}_4 &= (0, -1, 0) & \mathbf{e}_5 &= (0, 0, 1) & \mathbf{e}_6 &= (0, 0, -1) \\
\mathbf{e}_7 &= (1, 1, 0) & \mathbf{e}_8 &= (-1, 1, 0) & \mathbf{e}_9 &= (1, -1, 0) & \mathbf{e}_{10} &= (-1, -1, 0) \\
\mathbf{e}_{11} &= (1, 0, 1) & \mathbf{e}_{12} &= (-1, 0, 1) & \mathbf{e}_{13} &= (1, 0, -1) & \mathbf{e}_{14} &= (-1, 0, -1) \\
\mathbf{e}_{15} &= (0, 1, 1) & \mathbf{e}_{16} &= (0, -1, 1) & \mathbf{e}_{17} &= (0, 1, -1) & \mathbf{e}_{18} &= (0, -1, -1)
\end{aligned} \tag{5}$$

$$\begin{aligned}
c_s^2 &= \frac{1}{3} \\
w_0 &= \frac{8}{27} & w_{1-3,14-16} &= \frac{2}{27} & w_{10-13,23-26} &= \frac{1}{54} & w_{4-9,17-22} &= \frac{1}{216} \\
\mathbf{e}_0 &= (0, 0, 0) & \mathbf{e}_1 &= (-1, 0, 0) & \mathbf{e}_2 &= (0, -1, 0) & \mathbf{e}_3 &= (0, 0, -1) \\
\mathbf{e}_4 &= (-1, -1, 0) & \mathbf{e}_5 &= (-1, 1, 0) & \mathbf{e}_6 &= (-1, 0, -1) & \mathbf{e}_7 &= (-1, 0, 1) \\
\mathbf{e}_8 &= (0, -1, -1) & \mathbf{e}_9 &= (0, -1, 1) & \mathbf{e}_{10} &= (-1, -1, -1) & \mathbf{e}_{11} &= (-1, -1, 1) \\
\mathbf{e}_{12} &= (-1, 1, -1) & \mathbf{e}_{13} &= (-1, 1, 1) & \mathbf{e}_{14} &= (1, 0, 0) & \mathbf{e}_{15} &= (0, 1, 0) \\
\mathbf{e}_{16} &= (0, 0, 1) & \mathbf{e}_{17} &= (1, 1, 0) & \mathbf{e}_{18} &= (1, -1, 0) & \mathbf{e}_{19} &= (1, 0, 1) \\
\mathbf{e}_{20} &= (1, 0, -1) & \mathbf{e}_{21} &= (0, 1, 1) & \mathbf{e}_{22} &= (0, 1, -1) & \mathbf{e}_{23} &= (1, 1, 1) \\
\mathbf{e}_{24} &= (1, 1, -1) & \mathbf{e}_{25} &= (1, -1, 1) & \mathbf{e}_{26} &= (1, -1, -1)
\end{aligned} \tag{6}$$

The values of c_s , w_α and the vectors e_α are all selected so as to satisfy a set of symmetry conditions given in Equation 7.

$$\begin{aligned}
\sum_\alpha w_\alpha &= 1 & \sum_\alpha w_\alpha c_{\alpha i} &= 0 \\
\sum_\alpha w_\alpha c_{\alpha i} c_{\alpha j} &= c_s^2 \delta_{ij} & \sum_\alpha w_\alpha c_{\alpha i} c_{\alpha j} c_{\alpha l} &= 0 \\
\sum_\alpha w_\alpha c_{\alpha i} c_{\alpha j} c_{\alpha k} c_{\alpha l} c_{\alpha m} &= 0 \\
\sum_\alpha w_\alpha c_{\alpha i} c_{\alpha j} c_{\alpha l} c_{\alpha m} &= c_s^4 (\delta_{ij} \delta_{lm} + \delta_{il} \delta_{jm} + \delta_{im} \delta_{jl})
\end{aligned} \tag{7}$$

These symmetry conditions play an important roll in the theory of LBM. In particular, they are needed to show the correspondence between the LBM and the incompressible Navier-Stokes equation. It can be shown that all of the lattices introduced satisfy these conditions.

The discrete Boltzmann Equation shown in Equation 2 is in the general form of an advection equation. The momentum space is discretized along the q lattice speeds which, with the advection equation analogy, are the characteristic speeds. The right hand side of Equation 2 is the collision operator Ω_α which determines what happens to the particle populations f_α as they traverse the lattice in their respective characteristic directions. Instead of numerically integrating the temporal and spatial derivative operators, the LBM handles them discretely in time and space by “streaming” particle distributions from a source lattice site to neighboring lattice site in each direction. This process is illustrated schematically with the arrows in in Figure 1 and is formally expressed in Equation 8 where \mathbf{r} is the position vector for a given lattice point and t is the current time in lattice units.

$$f_\alpha(\mathbf{r} + \mathbf{e}_\alpha, t + 1) - f_\alpha(\mathbf{r}, t) = \Omega_\alpha. \quad (8)$$

The simplest and most popular form for the collision operator is the Bhatnagar-Gross-Krook (BGK), shown in Equation 9, which gives a single-parameter relaxation to equilibrium:

$$\Omega_\alpha^{\text{BGK}} = -\frac{1}{\tau} (f_\alpha - f_\alpha^{eq}) \quad (9)$$

where τ is a relaxation parameter, f_α^{eq} is a function of the macroscopic parameters of the fluid represented by f_α given by Equation 10.

$$f_\alpha^{eq} = \rho w_\alpha \left[1 + \frac{(\mathbf{e}_\alpha \cdot \mathbf{u})}{c_s^2} + \frac{(\mathbf{e}_\alpha \cdot \mathbf{u})^2}{c_s^4} - \frac{1}{2} \frac{(\mathbf{u} \cdot \mathbf{u})}{c_s^2} \right] \quad (10)$$

The macroscopic variables of fluid density and velocity, given by ρ and \mathbf{u} , respectively, are

computed as moments of the particle distribution function f_α as shown in Equations 11 and 12. When required for physical modeling, the fluid pressure p can also be obtained from Equation 13.

$$\rho = \sum_{\alpha=0}^{q-1} f_\alpha \quad (11)$$

$$\mathbf{u} = \frac{1}{\rho} \sum_{\alpha=0}^{q-1} f_\alpha \mathbf{e}_\alpha \quad (12)$$

$$p = \rho c_s^2 \quad (13)$$

The relaxation parameter τ can be related to the fluid kinematic viscosity ν . This relationship is given in Equation 14 with all units expressed in lattice units.

$$\tau = \frac{\nu}{c_s^2} + \frac{1}{2} \quad (14)$$

Frequently in the literature, and periodically in this thesis, the inverse of τ is used as the relaxation parameter and is conventionally named ω . Since for real fluids, ν must be non-negative, τ is constrained to be greater than or equal to $\frac{1}{2}$. In notation employing ω , this implies $0 \leq \omega \leq 2$. In a later section of this thesis where dimensional scaling and stability are discussed, it will be demonstrated that the numerical stability of any given LBM simulation can be characterized by the value of τ or ω . Systems where the combined fluid properties, boundary conditions and LBM spatial and temporal discretizations result in the value of ω to be close to 2, or conversely τ approaching $\frac{1}{2}$, tend to become numerically unstable.

C. MULTIPLE RELAXATION TIME COLLISION OPERATOR

While the single relaxation time lattice Bhatnagar-Gross-Krook (LBGK) operator is easy to implement and computationally efficient within the context of a single LBM time

step, it is known to suffer from severe stability problems. When these stability problems can be overcome while still using LBGK, it is often only obtained at the expense of an increase in lattice density and hence, increase in computational effort. The LBGK has other deficiencies including an implied fixed Prandtl number of one and a fixed ratio between kinematic and bulk viscosity. In order to provide a means for tuning the stability properties of a given simulation while also a mechanism for altering more specific fluid properties, alternative collision operators have been developed.

The multiple relaxation time (MRT) collision operator, also referred to as the generalized lattice Boltzmann equation, was first presented in [24]. Its objectives were to resolve the fixed Prandtl number defect of LBGK, and allow for varying kinematic and bulk viscosities as well as introduce a mechanism for increasing simulation stability. The MRT projects the density distribution functions f_α onto an orthogonal vector space of momenta of the vector space using the operator \mathbf{M} . The particular momenta depend on the lattice structure chosen but all include a combination of the mass density, kinetic energy, momentum flux, energy flux and viscous stress tensor. They are expressed in the vector \mathbf{R} . Relaxation occurs over the momentum space using the relaxation times given in \mathbf{S} and the result is transformed back to the density space f_α using the inverse of \mathbf{M} .

For the D2Q9 lattice, the momentum space and transformation matrix are given in Equations 15 and Equation 16, respectively.

$$\mathbf{R}_{\text{D2Q9}} = \begin{bmatrix} \rho & e & \epsilon & j_x & q_x & j_y & q_y & p_{xx} & q_{xy} \end{bmatrix}^T \quad (15)$$

$$\mathbf{M}_{D2Q9} = \begin{bmatrix} 1 & 1 & 1 & 1 & 1 & 1 & 1 & 1 & 1 \\ -4 & -1 & -1 & -1 & -1 & 2 & 2 & 2 & 2 \\ 4 & -2 & -2 & -2 & -2 & 1 & 1 & 1 & 1 \\ 0 & 1 & 0 & -1 & 0 & 1 & -1 & -1 & 1 \\ 0 & -2 & 0 & 2 & 0 & 1 & -1 & -1 & -1 \\ 0 & 0 & 1 & 0 & -1 & 1 & 1 & -1 & -1 \\ 0 & 0 & -2 & 0 & 2 & 1 & 1 & -1 & -1 \\ 0 & 1 & -1 & 1 & -1 & 0 & 0 & 0 & 0 \\ 0 & 0 & 0 & 0 & 0 & 1 & -1 & 1 & -1 \end{bmatrix} \quad (16)$$

where $\mathbf{R} = \mathbf{M}f_\alpha$ and ρ is fluid density, e is the energy, ϵ is related to the square of the energy, j_x and j_y are mass fluxes, q_x and q_y correspond to energy flux and p_{xx} and p_{xy} correspond to the diagonal and off-diagonal components of the viscous stress tensor. The coefficients for relaxation over this momentum space are given in a diagonal matrix as in Equation 17.

$$\mathbf{S} = \text{diag}(0, s_2, s_3, 0, s_5, s_7, s_8, s_9) \quad (17)$$

In [25] it was shown that the same fluid viscosity is given in the fluid flow when $s_8 = s_9 = \frac{1}{\tau}$. The other parameters in Equation 17 can be set as desired so as to promote solution stability or as required to further tailor fluid behavior. If all non-zero coefficients of \mathbf{S} are set to $\frac{1}{\tau}$, LBGK single-relaxation time is recovered. Having specified the coefficients of \mathbf{S} , the LBM collision operator is as shown in Equation 18,

$$\Omega^{\text{MRT}} = -\mathbf{M}^{-1}\mathbf{S}\mathbf{M}(f - f^{eq}) \quad (18)$$

where all values of f_α are relaxed with a single matrix collision operator. In the software developed for this work, it has been observed that use of MRT significantly promotes simulation stability. While the MRT requires more computations per time-step, it has been found

that simulations are able to be conducted with much lower lattice density. Furthermore, fewer time steps are typically required for flows to overcome the noise of nonequilibrium initial conditions and reach accurate flow configurations.

D. BOUNDARY CONDITIONS

The fluid flow problems which we hope to solve using LBM are initial boundary value problems. As such, the handling of initial and boundary conditions should be central to any discourse on numerical solution methods.

One problem with LBM is that the physically relevant and observable macroscopic flow features such as velocity and pressure are not the dependent variables in the governing equation; rather they are functions of the dependent variables. While it is possible to find a reasonable set of f_α corresponding to a particular pressure and velocity there is in general no unique way to do this.

Despite this difficulty, researchers have formulated numerous schemes that try to view the boundary lattice points in a manner consistent with every other lattice point with the exception that, for certain lattice directions there is no updated data streamed in from the previous time step. This condition is illustrated schematically in Figure 3.

The boundary condition schemes described in this section represent answers to the dual questions:

1. What value should be given for each f_α for which there is not a corresponding neighbor?
2. How can this be done so as the desired macroscopic boundary condition will be enforced?

The boundary conditions discussed in this section answer these questions. The discussion will not survey all available methods, but only those implemented for this research. Each method will be examined on the basis of stability and implementation effectiveness.

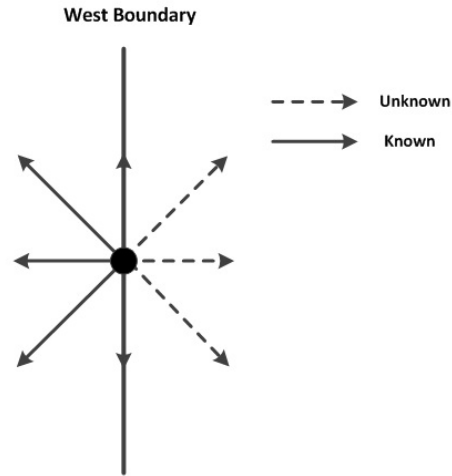


Figure 3: Schematic of lattice point on west domain boundary.

1. Periodic Boundaries

Periodic boundary conditions are a common and easy to implement boundary condition with LBM. For nodes along a periodic boundary, the node along the corresponding periodic boundary is assigned as the nearest neighbor for streaming purposes. The density distribution for that direction is replaced accordingly as is shown in Figure 4.

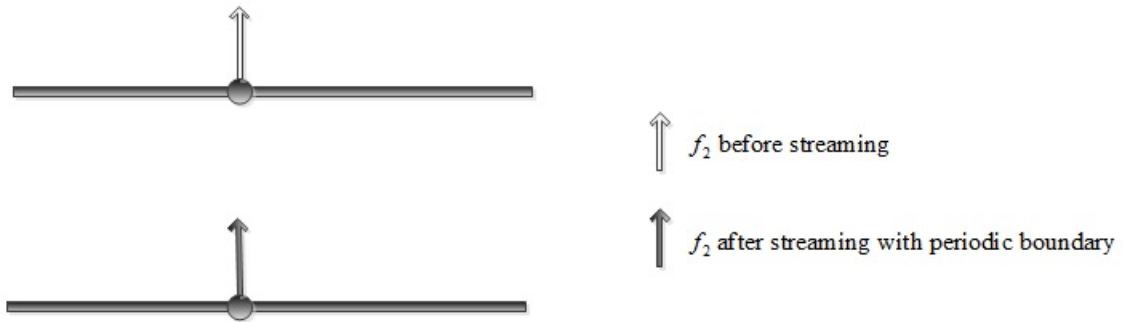


Figure 4: Streaming of f_2 across a North/South periodic boundary.

2. Solid Boundaries

Solid boundaries appear in a wide variety of applications. The LBM solution to a flat no-slip boundary is the so-called “bounce-back” boundary condition in which all unknown values of f_α are replaced with the values that are known, but from the opposite direction. Additionally, directions parallel to the solid boundary are also reversed, resulting in the exchange of density distribution values for all opposing directions. This is illustrated in Figure 5. Solid boundaries implemented in this fashion are often referred to as “dry-nodes” because they do not undergo the collision process. This simplifies implementation and execution efficiency considerably since macroscopic values need not be computed at these nodes nor must the equilibrium distribution be evaluated. This so-called “on-grid” version of the bounce-back boundary conditions has been shown to be first-order accurate in [26].

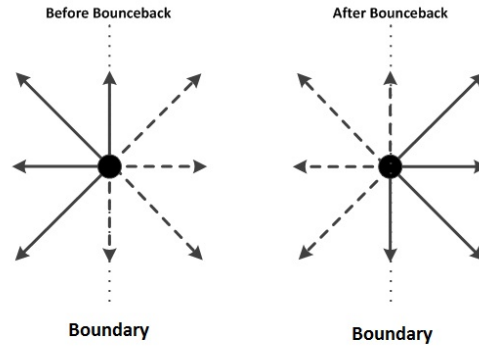


Figure 5: Application of on-grid bounce-back boundary condition.

In [27], Ladd introduced an alternate scheme where the lattice points are arranged so that the physical wall is actually located exactly half-way between the first fluid point inside the domain and the corresponding solid node representing the wall. This scheme is illustrated in Figure 6 and has been shown to exhibit second-order convergence.

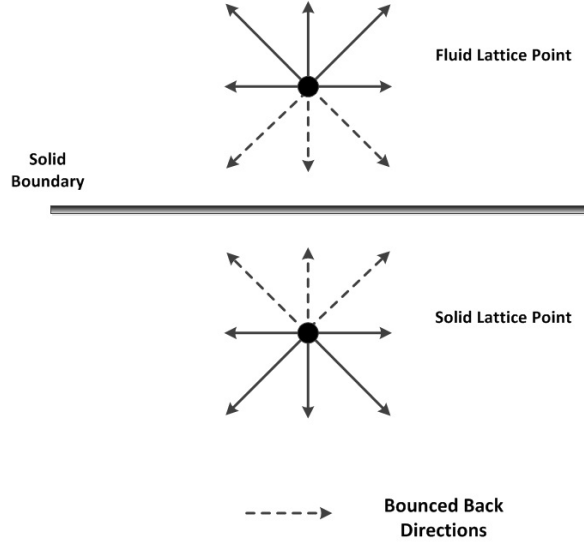


Figure 6: Half-way bounceback solid boundary condition schematic.

3. Moving Solid Boundaries

This boundary condition seeks to apply an appropriate redistribution to the density distribution to achieve a prescribed velocity to the moving solid while maintaining mass conservation. It finds practical application in fluid-structure interaction problems as described in [28] as well as pure benchmark problems such as the lid-driven cavity.

During each collision step, the values of f_α are modified according to Equation 19.

$$f_\alpha = f_\alpha + \frac{\rho w_\alpha \mathbf{e}_\alpha \cdot (\mathbf{u}_{bc} - \mathbf{u})}{c_s^2} \quad (19)$$

Due to the symmetry of the lattice vectors \mathbf{e}_α and weights w_α , the total density at the lattice is invariant through the execution of Equation 19 but the distributions are adjusted to achieve the prescribed boundary velocity \mathbf{u}_{bc} .

To the best of this author's knowledge, no formal analysis has been done regarding the stability or accuracy properties of this procedure. As a heuristic method for achieving a desired momentum input to the fluid system under simulation while maintaining conservation of mass, it is very appealing. It is generally formulated for any lattice structure or

location within the domain and in fluid simulations where it has been used for this work, it has shown excellent stability properties. As for accuracy, it was used in the lid-driven cavity benchmark discussed in Chapter III where it is shown to allow for excellent agreement with both experimental and computational data reported in the literature.

4. Prescribed Velocity or Pressure Boundaries

Prescribed velocity and pressure boundary conditions constitute an indispensable tool for fluid modeling problems. As with other boundary condition schemes, the methods to be described in this section all seek to assign suitable values to f_α for lattice points along a boundary so that the desired macroscopic conditions are realized. An excellent review paper can be found at [29] that formally analyzes several methods. Details included in this section are drawn largely from this reference. A common theme among boundary conditions of this type is that specification of either density—which in the LBM framework is equivalent to pressure by using Equation 13—or velocity, the other macroscopic variable can be determined based solely on the known values of f_α .

Referring to Figure 7, the contributors to the macroscopic density at a lattice point can be grouped into three categories: those stationary or parallel to the boundary $\rho_0 - f_0, f_2$, and f_4 in this case; those known density distributions pointed into the boundary $\rho_+ - f_3, f_6$, and f_7 ; and those pointed out from the boundary $\rho_- - f_1, f_5$ and f_8 . Every straight boundary will have this grouping. Comparing this with Equation 11, it can be seen that Equation 20 is an identity. Additionally, considering the lattice velocities it is easy to demonstrate that the velocity component perpendicular to the straight boundary can be expressed as in Equation 21.

$$\rho = \rho_- + \rho_0 + \rho_+ \quad (20)$$

$$\rho u_\perp = \rho_+ - \rho_- \quad (21)$$

Given Equations 20 and 21, given either the value for the velocity component into the domain, u_\perp or ρ , it is always possible to determine the other using only the density distribution components that are known after streaming - ρ_0 and ρ_+ . These relations are given in

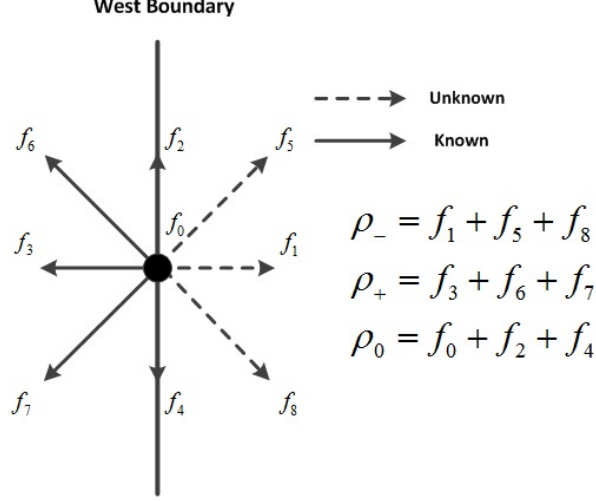


Figure 7: Groups of density distributions on west boundary lattice point.

Equations 22 and 23.

$$\rho = \frac{1}{1 + u_{\perp}} (2\rho_+ + \rho_0) \quad (22)$$

$$u_{\perp} = -1 + \frac{(2\rho_+ + \rho_0)}{\rho} \quad (23)$$

Once the value for ρ and \mathbf{u} are known on the boundary, this information can be used to judiciously assign values either to the unknown density distributions as in the Zou-He type boundary conditions [30] or, in the case of the regularized boundary conditions introduced in [31], to all distributions.

a. Zou-He Boundaries

The Zou-He scheme for prescribed pressure or velocity seek to find suitable values only for the unknown density distributions at the boundary lattice point. For this example, the case of a prescribed-velocity boundary condition on the West domain boundary as depicted in Figure 7 will be used.

For the condition depicted, when accounting for the prescribed velocity on the boundary, there remain four unknowns: ρ , f_1 , f_5 and f_8 . Balanced against these four unknowns is the known relation for density given in Equation 11, and two equations for momentum given by Equation 12. In order to provide closure, a fourth relationship is necessary. The Zou-He boundary conditions develop this relationship by assuming “bounce-back” of the non-equilibrium part of the density distribution directed perpendicular to the boundary. In this case, this gives us Equation 24.

$$f_1 - f_1^{\text{neq}} = f_3 - f_3^{\text{neq}} \quad (24)$$

Applying Equation 10 along with the known ρ and \mathbf{u} and appropriate lattice vectors e_1 and e_3 and weights w_1 , w_3 , the above relation simplifies to Equation 25

$$f_1 = f_3 + \frac{2}{3}\rho u_x \quad (25)$$

In two dimensions, this provides closure and values of the remaining unknown density distribution functions can be determined. For this example, the expressions are given as Equation 26 and Equation 27.

$$f_5 = f_7 + \frac{1}{2}(f_4 - f_2) + \frac{1}{2}\rho u_y + \frac{1}{6}\rho u_x \quad (26)$$

$$f_8 = f_6 - \frac{1}{2}(f_4 - f_2) - \frac{1}{2}\rho u_y + \frac{1}{6}\rho u_x \quad (27)$$

For prescribed pressure, the procedure is the same, except that given ρ , we solve for u_\perp - in this case u_x .

For three dimensions, there are still more unknowns; using the D3Q15 lattice and applying a boundary condition to the west domain boundary, In addition to one of ρ or u_\perp , there are five density distributions that are unknown: f_1, f_7, f_9, f_{11} and f_{13} . In the case of the D3Q27 lattice, there are nine unknown density distribution functions.

The idea demonstrated in [32] is to apply the non-equilibrium bounce-back as used in Equation 24 to *all* unknown density distribution values relative to the known density distribution in the opposite direction. If we adopt the convention that for a given density distribution f_k , $f_{\bar{k}}$ connotes the density distribution traveling in the opposite direction, and f_k is an unknown density distribution, this is shown in Equation 28 for the D3Q15 lattice.

$$f_k = f_{\bar{k}} + (f_k^{eq} - f_{\bar{k}}^{eq}) \quad , k \in \{1, 7, 9, 11, 13\} \quad (28)$$

In order to correct for momenta in the plane of the boundary—for this example, in the y and z directions—an adjustment is applied to the density distributions that are not perpendicular to the boundary, which is shown in Equation 29 for the D3Q15 lattice.

$$f_k = f_{\bar{k}} + \frac{1}{4} [e_{ky} (f_3 - f_4) + e_{kz} (f_5 - f_6)] \quad , k \in \{7, 9, 11, 13\} \quad (29)$$

Putting this all together, we arrive at Equations 30 and 31.

$$f_1 = f_2 + \frac{2}{3} \rho_{in} u_x \quad (30)$$

$$f_k = f_{\bar{k}} + \frac{1}{12} \rho_{in} u_x - \frac{1}{4} [e_{ky} (f_3 - f_4) + e_{kz} (f_5 - f_6)] \quad , k \in \{7, 9, 11, 13\} \quad (31)$$

For other lattice types and other boundaries, the same general prescription is followed.

b. Regularized Boundaries

For regularized boundary conditions, introduced in [31] and discussed in more detail in [29], all particle distribution functions on boundary lattice points are replaced based on values of ρ , \mathbf{u} or $\Pi^{(1)}$ that are either specified by the boundary condition or computed based on known particle distribution values.

In the same fashion as with the Zou-He boundary condition, given either ρ or u_\perp , the other macroscopic variable can be determined based on the known values of f_α . Once this is complete, f_α^{eq} is computed using Equation 10. Values for the unknown density distribution function— f_k —are initially estimated based on bounce-back of the non-equilibrium parts as in Equation 28. Since we cannot know the non-equilibrium portion of f_k , we simply assign it to have the same non-equilibrium component as $f_{\bar{k}}$ as shown in Equation 32.

$$f_k = f_k^{eq} + f_{\bar{k}} - f_{\bar{k}}^{eq} \quad (32)$$

The tensor Π is the second-order moment of the particle density populations and can be expressed as in Equation 33.

$$\Pi = \sum_{\alpha=0}^{q-1} \mathbf{e}_\alpha \mathbf{e}_\alpha f_\alpha \quad (33)$$

Equation 34 is used to reconstruct hydrodynamically consistent values for all f_α on the boundary lattice point,

$$f_\alpha = f_\alpha^{eq} + \frac{w_\alpha}{2c_s^4} \mathbf{Q}_\alpha : \Pi \quad (34)$$

where $\mathbf{Q}_\alpha = \mathbf{e}_\alpha \mathbf{e}_\alpha - c_s^2 \mathbf{I}$, \mathbf{I} being the identity matrix. This method for boundary condition application is appealing for its generality. The superior stability properties of this method is discussed at length in [29] and [31].

E. BODY FORCES

Many physical simulations require the application of a body force. Some simple examples would be a simulation that includes gravity; a simulation with an imposed differential pressure, where the pressure is included as a body force on the fluid particles; or a multi-component model where the interaction between particles of different species are

modeled by nearest-neighbor force inputs. The most common way to incorporate these forces is via an adjustment to the equilibrium velocity as given in Equation 35,

$$\mathbf{u}^{\text{eq}} = \mathbf{u} + \Delta\mathbf{u} \quad (35)$$

where $\Delta\mathbf{u}$ is given by Equation 36.

$$\Delta\mathbf{u} = \frac{\tau\mathbf{F}}{\rho} \quad (36)$$

Equation 36 can be understood heuristically by considering $\mathbf{F} = m\mathbf{a} = m\frac{d\mathbf{u}}{dt}$ with the relaxation parameter τ taking the role of the differential in time.

F. SCALING

The goal of any numeric simulation is to obtain quantitative and qualitative results that can be applied to a particular physical system of interest. Much LBM literature is cast in “LBM units” where the distance between lattice points and the time for each time step is unity. This presents a clean palate on which to develop the theory, but leaves out the crucial details of how to tailor LBM simulation parameters so that the results can be related to a particular set of fluid conditions.

In previous sections, the equations relevant for staging and executing a LBM simulation were presented entirely in lattice units—where every time step is of unit length and the distance between any adjacent lattice sites is also of unit length. Since this basic system of units is generally unsuitable for physical problems, basic physical parameters given in some units of length and time must be re-scaled consistently so that these parameters can be converted into units suitable for incorporation into the LBM algorithm.

As an intermediate step, it is sometimes customary to rescale physical units to non-dimensional units. This is particularly useful in cases where knowledge of the system state in terms of some non-dimensional parameters such as the Reynolds number is needed.

The nondimensionalization and scaling scheme employed for this research is illustrated in Figure 8.

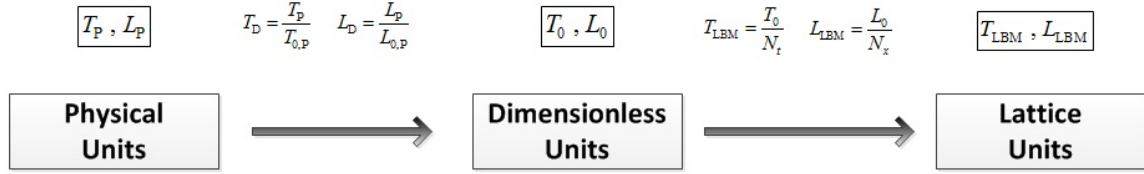


Figure 8: Scaling from physical units, to dimensionless units to LBM units.

G. EXAMPLE

In an attempt to clarify the discussion from this chapter, the LBM formulation of a model problem will be discussed in detail.

1. Problem Description

The procedures discussed in this chapter are summarized in the flowchart appearing in Figure 10. The problem to be considered is illustrated schematically in Figure 9. The problem involves flow within a two-dimensional channel around a cylindrical obstacle. Flow enters from the left boundary with a prescribed parabolic velocity and exits out the right boundary with a prescribed constant pressure. The top and bottom boundary are modeled as no-slip walls.

2. Scaling and Setup

The process of scaling for this example problem will be completed in two steps as described in the section on scaling. First, a characteristic time scale T_0 and length scale L_0 will be identified. For this problem of a cylindrical obstruction in two dimensional channel flow, the natural choice is to use the conventions for Reynolds scaling where the characteristic length is the diameter of the cylinder. Therefore, the characteristic length in physical units $L_{0,p} = 0.2$ m. The characteristic time is assigned to be the time required

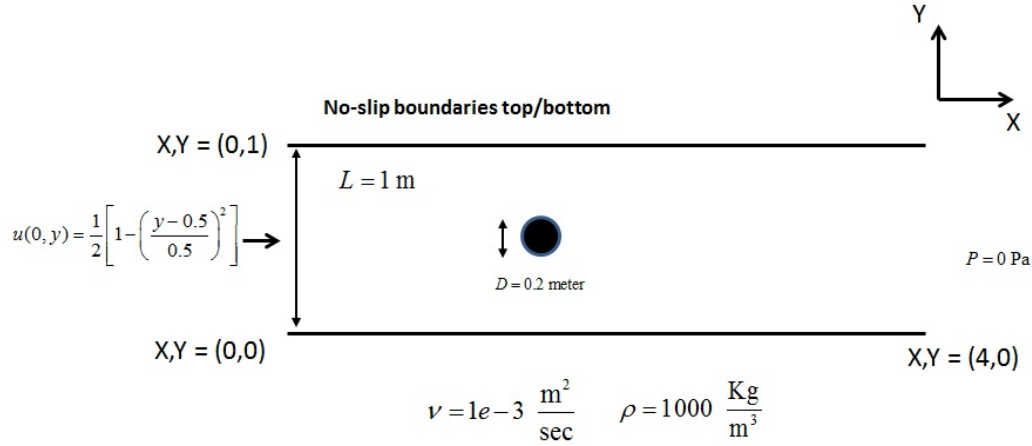


Figure 9: Schematic diagram of channel flow example problem.

for an average fluid particle to traverse the diameter of the cylinder. For the assigned inlet boundary condition, the average fluid velocity is two-thirds of the maximum inlet velocity of $0.5 \frac{\text{m}}{\text{sec}}$ for the parabolic profile. Consequently, $T_{0,p} = \frac{L_{0,p}}{U_{0,p}} = \frac{0.2}{0.5} = 0.4 \text{ sec}$. All of this corresponds to a Reynolds number of 100, which is convenient to know when comparing the output of the LBM simulation against experimental data or benchmark values.

The second step is to decide how finely the reference time and space scales are to be subdivided. For this example, the reference length L_0 will be represented with 25 lattice points, so there are intervals in the reference length. In terms of dimensionless units, $L_0 = 1$. The conversion between dimensionless units and the LBM units is therefore: $L_{LBM} = \delta_x = \frac{1}{25-1} = 0.0417$. To convert between a distance in terms of lattice units and a distance in physical units, one would multiply by both the conversion factors. Therefore, the physical spacing of the lattice points is $\delta_x \times L_{0,p} = 0.0083 \text{ m}$. Similarly the time domain is discretized by deciding how many time steps will be used to traverse a single unit of the reference time T_0 . For this problem, the reference time will be divided by 250 time steps, so $\delta_t = \frac{T_0}{N_t} = \frac{1}{250} = 0.004 \text{ seconds}$. As with the spatial scaling, in order to convert a single LBM time step to physical elapsed time, one must multiply by

the scaling parameters between the Dimensionless units and LBM units in addition to the conversion between Physical and Dimensionless units. For this problem, those conversions are $T_P = T_{\text{LBM}} \times \delta_t \times T_0 = 0.0016$.

Once the spatial and temporal scaling factors are determined, the properly scaled LBM parameters must be determined from the given physical data.

a. Viscosity Scaling

In order to get dynamic LBM behavior that corresponds to the desired physical fluid under the prescribed conditions, the temporal and spatial scaling factors need to be applied to the specified fluid kinematic viscosity ν . Since ν has units of $\frac{\text{m}^2}{\text{sec}}$ the necessary conversion can be accomplished via Equation 37.

$$\nu_{\text{LBM}} = \nu_{\text{Physical}} \times \frac{T_0 \delta_t}{(L_0 \delta_x)^2} \quad (37)$$

Carrying out this conversion for the specified fluid with the chosen discretization results in $\nu_{\text{LBM}} = 0.023$. This is the value that is applied to Equation 14 to find the LBM relaxation parameter. Doing so for this problem results in $\tau = 0.57$ or $\omega = 1.76$

b. Velocity BC Scaling

This problem has a prescribed inlet velocity profile. The velocity is expressed in terms of meters-per-second, which is not compatible with the unit system assumed when the LBM boundary conditions were developed. The velocity is simply scaled in accordance with Equation 38.

$$u_{\text{LBM}} = u_{\text{Physical}} \times \frac{T_0 \delta_t}{L_0 \delta_x} \quad (38)$$

For this problem, this conversion reads:

$$u(0, y) = \frac{3}{4} \left[1 - \frac{(y - 0.5)}{0.5} \right] \times \frac{0.0016}{0.0083} = 0.144 \left[1 - \frac{(y - 0.5)}{0.5} \right].$$

This is the velocity that will be passed to the LBM time-stepping routine in order to set the prescribed velocity at the inlet lattice points.

c. Pressure BC Scaling

For this problem, the prescribed outlet pressure is set to 0 Pa. This is a relative pressure, of course, otherwise the density for lattice points at the outlet would need to be set to zero according to Equation 13. Since the prescribed pressure boundary condition procedures are actually methods for enforcing a specific *density* at the boundary, in order to employ the pressure boundary condition for evaluating pressure on the domain we must:

- Compute the pressure through the domain using Equation 11 and Equation 13 along with the value of c_s applicable for the lattice in use.
- Scale the computed pressure to physical units using Equation 39. In this step, one is simply converting c_s^2 to physical units.
- Adjust the pressure in physical units so that the boundary condition is satisfied as in Equation 40.

$$P_{\text{Physical}} = \rho_{\text{LBM}} c_s^2 \left(\frac{\delta_x L_0}{\delta_t T_0} \right)^2 \quad (39)$$

$$P = P_{\text{Physical}} - P_{\text{Boundary}} \quad (40)$$

3. Initialization and Lattice Point Classification

As final steps before commencing the LBM time-stepping routine, the initial values for f_α must be established for all lattice points. Additionally, all boundary lattice points, solid lattice points, and any other type of lattice point that will require special treatment must be identified. For this problem, we need only identify inlet nodes for the prescribed velocity boundary condition, outlet nodes for the pressure boundary condition as well as

solid nodes for the top and bottom boundary as well as the cylindrical obstruction. Each of these classes of lattice points will be treated with distinction during each time-step.

There is no solidly established means for establishing an initial condition. A common choice for many problems is to simply set the initial set of f_α for each lattice point equal to the equilibrium density distribution as computed with Equation 10 to some pre-determined velocity and density distribution. This is shown in Equation 41 for the D2Q9 lattice.

$$f_\alpha(\mathbf{x}, 0) = f_\alpha^{eq} = \rho w_\alpha \left[1 + 3(\mathbf{e}_\alpha \cdot \mathbf{u}_0) + \frac{9}{2}(\mathbf{e}_\alpha \cdot \mathbf{u}_0)^2 - \frac{3}{2}(\mathbf{u}_0 \cdot \mathbf{u}_0) \right] \quad (41)$$

Similarly, there is no standardized procedure for generating the lattice domain, identifying inlet and outlet lattice points or lattice points along solid boundaries. General-purpose, Open-source lattice-generating software that could carry out tasks such as these on more complex geometries do not seem to exist. For problems with simple geometry, as this example problem does, this task can be executed quite efficiently with simple searches based on lattice point geometric position. (e.g, all of the inlet lattice points can simply be found by identifying all of those points that lie along $x = 0$ and where $y \neq 0$ and $y \neq 1$).

4. Time-Stepping

The basic time-stepping scheme is illustrated in the flowchart shown in Figure 10. Fluid nodes not on a boundary compute values for macroscopic density and velocity using Equation 11 and 12. These values are used to compute f_α^{eq} using Equation 10. Using the scaled relaxation parameter computed using Equations 37 and 14, perform the BGK relaxation using Equation 9. A visualization of the results after 50,000 time steps are shown in Figure 11. This represents approximately 80 seconds of physical time according to our time scaling factor computed above.

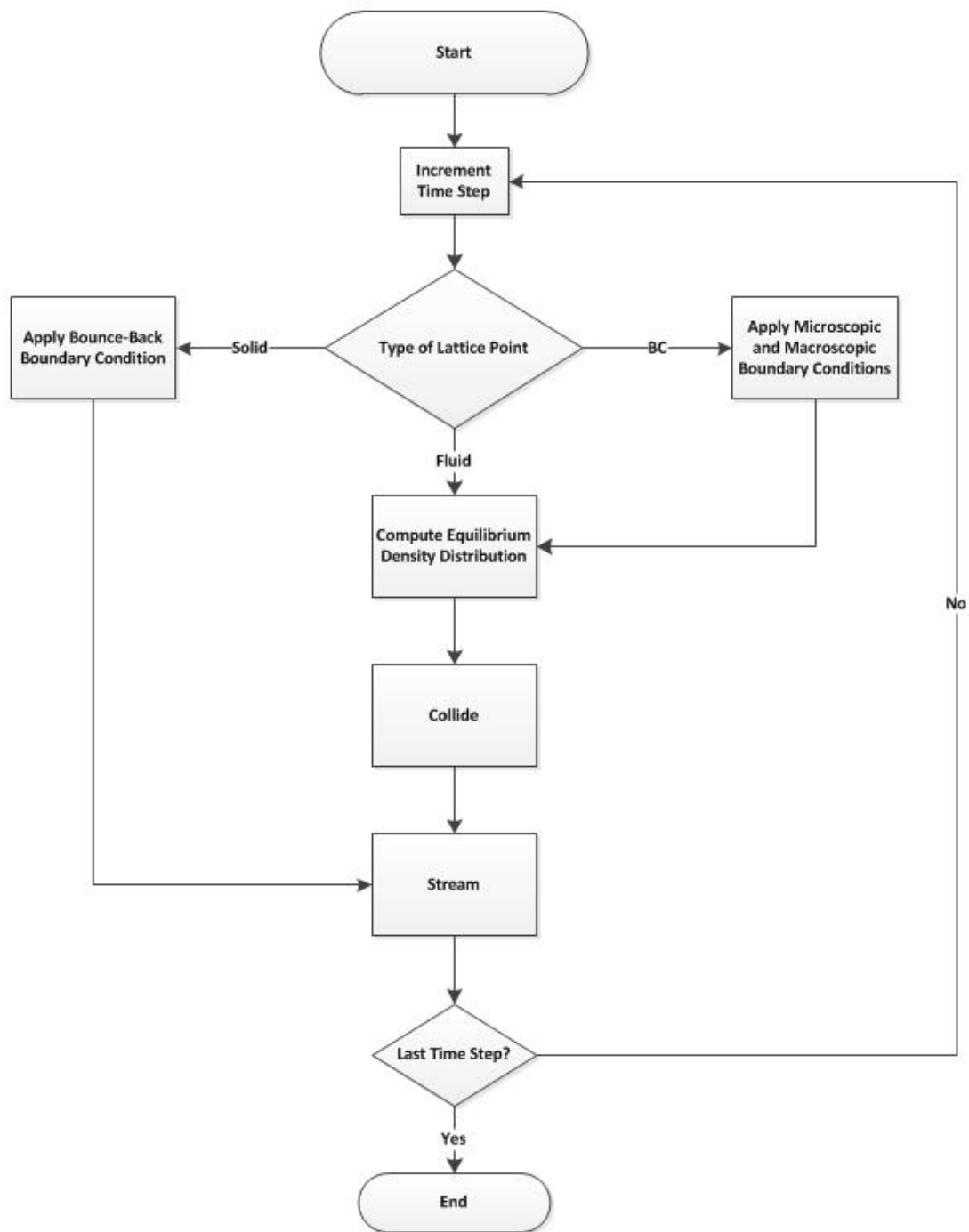


Figure 10: LBM time step flowchart.

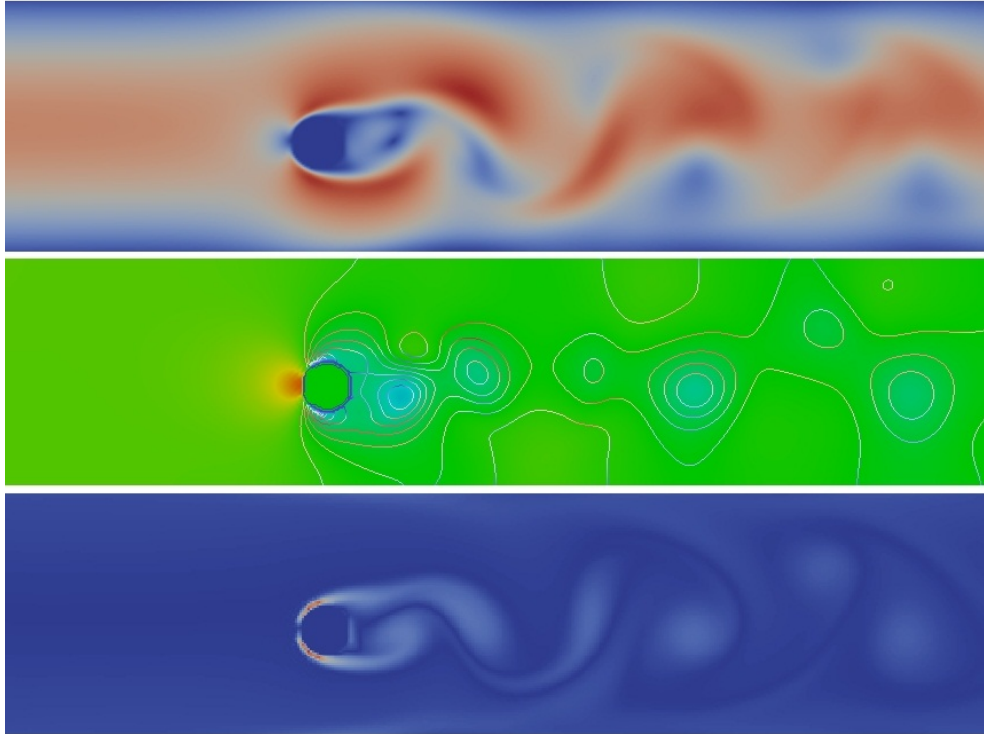


Figure 11: Velocity magnitude, pressure, and vorticity magnitude for example flow case after 50,000 time steps.

III. IMPLEMENTATION AND VALIDATION

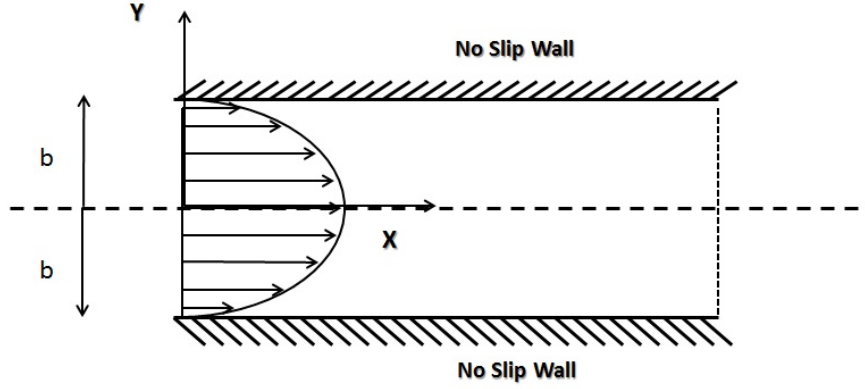
In order to model fluid structure interactions with LBM and FEM, it is necessary to have available a reliable, flexible and powerful implementation of the LBM. It must first be reliable so that we can have some reasonable hope that the results obtained will be comparable to physical reality. It must be flexible so that a wide variety of simulations can be conducted, pertaining to different physical conditions of interest. It must be powerful so that these simulations can be refined for greater accuracy while still able to be completed in a reasonable amount of time.

In this chapter, a body of software tools, designed using the theory presented in Chapter II, is tested against a selection of standard benchmarks first for accuracy and then for performance. The following results are obtained from this work:

- The LBM software as implemented for this work reliably reproduces results obtained Poiseuille flow, lid-driven cavity, flow over a backward step and flow over a cylindrical obstruction for 2D.
- The LBM provides second-order convergence to the 2D Poiseuille flow with appropriate boundary conditions and double precision arithmetic. A mixed-precision algorithm is introduced which allows similar second-order convergence while only storing single-precision data.
- The LBM is benchmarked for performance against recently published implementations for 3D lid-driven cavity flow. It is shown that the software produced for this work has competitive performance with other single-workstation implementations recently produced.

A. POISEUILLE FLOW

The first test case is a two-dimensional flow case between parallel plates. The flow condition is depicted in Figure 12.



$$u(0, y, t) = U_{\max} \left[1 - \left(\frac{y-b}{b} \right)^2 \right] \quad p(L, y, t) = p_{\text{out}} = \text{Constant}$$

Figure 12: Poiseuille flow configuration.

Channel Width ($2 \times b$)	1.0 m
fluid density (ρ)	$1000 \frac{\text{Kg}}{\text{m}^3}$
fluid viscosity (μ)	$1 \frac{\text{N}\cdot\text{s}}{\text{m}^2}$
Maximum inlet velocity (U_{\max})	$0.015 \frac{\text{m}}{\text{s}}$

Table 1: Geometry and fluid parameters for Poiseuille flow test case.

The solution to this problem is known to be a function of y only and is given in Equation 42:

$$u(y) = -\frac{1}{2\mu} \frac{dp}{dx} (b^2 - y^2) \quad (42)$$

with $\frac{dp}{dx}$ given as a function of maximum velocity and fluid viscosity in Equation 43

$$\frac{dp}{dx} = -\frac{2\mu}{b^2} u_{\max}. \quad (43)$$

The maximum velocity is set by the inlet boundary condition. Specific fluid and flow conditions are presented in Table 1.

1. Solution with On-Grid Bounceback Boundary Conditions

For the LBM model of this problem, the D2Q9 lattice with LBGK dynamics was used along with Zou/He boundary conditions for the prescribed velocity on the west boundary and constant prescribed pressure on the east boundary. The initial lattice discretization was set so that 30 lattice points would span the channel entrance. The time step was set to achieve a relaxation parameter ω of 1.30. While refining the grid to test for convergence, the time step was adjusted so as to maintain a constant relaxation parameter for all tests. The results are shown in Figure 13. As expected, first-order convergence is obtained for this style of boundary condition.

2. Solution with Half-Way Bounceback Boundary Conditions

The half-way bounce-back boundary condition was implemented and used in an identical set of tests. The goal of this step, in addition to showing the convergence properties of the boundary condition, is to illustrate the second-order convergence properties of the LBM as a whole. Results for single precision are shown in Figure 14. It is clear from the figure that, for problems with modest accuracy and comparatively coarse lattice densities, second-order convergence is obtained. For more refined lattices, however, the expected convergence rate is lost in single-precision. To investigate the effect of the numerical precision in which the software is written, an alternate implementation was generated utilizing double precision arithmetic for all LBM calculations. Results of this convergence test are shown in Figure 15. In order to avoid the cost of double precision computations a mixed precision LBM kernel was developed. Through an experimental analysis of the sources of error in the LBM computations, it was found that numerical results nearly identical to that obtained with full double precision computations could be obtained by conducting only computation of f_{α}^{eq} and collisions in double precision. Convergence results for this computation are shown in Figure 16.

The mixed precision brings the accuracy of double precision with a lower cost for memory consumption and with better performance than a pure double precision computation. The memory cost for working in double precision is simply twice that of single

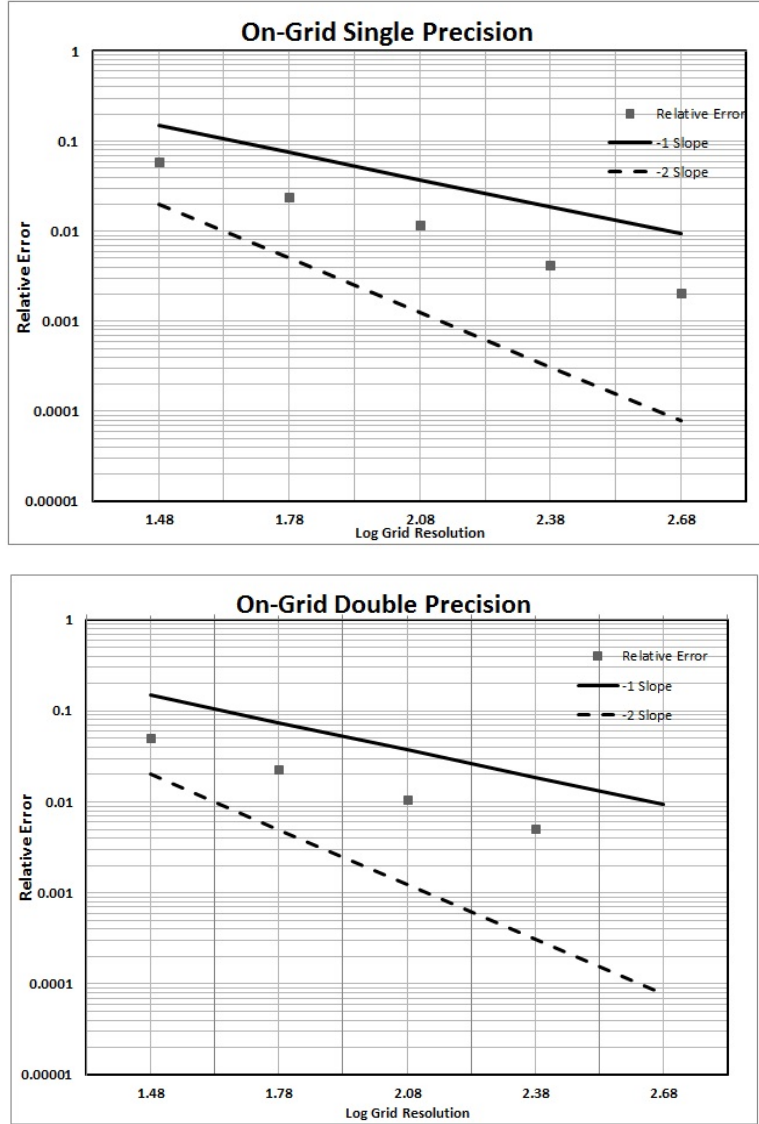


Figure 13: Poiseuille flow convergence with On-Grid bounce-back boundary conditions.

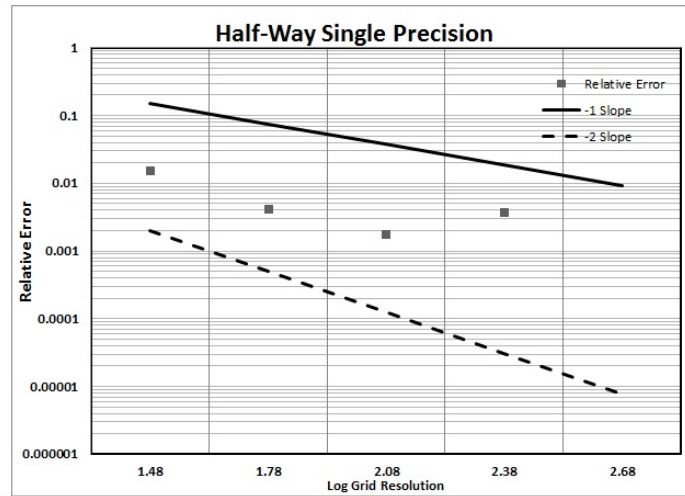


Figure 14: Poiseuille flow convergence with half-way bounce-back boundary conditions in single precision.

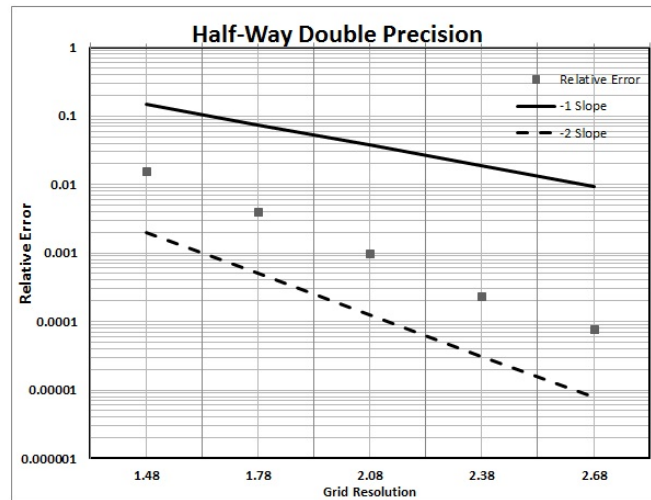


Figure 15: Poiseuille flow convergence with half-way bounce-back boundary conditions in double precision.

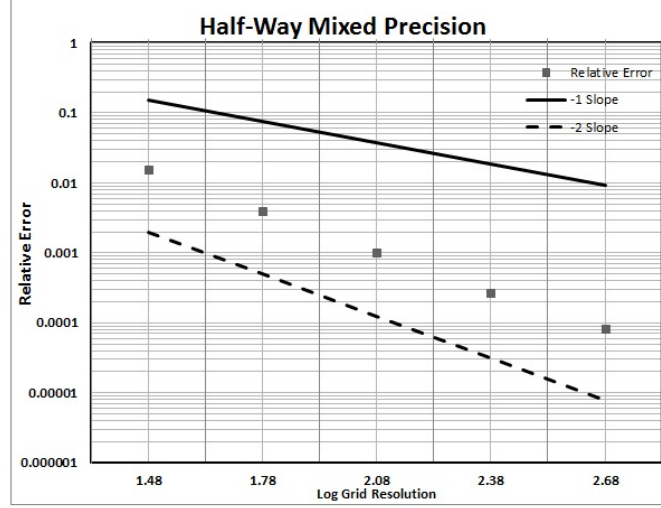


Figure 16: Poiseuille flow convergence with half-way bounce-back boundary conditions using mixed-precision arithmetic.

precision. The relative computational performance of single, mixed and double precision are presented in Figure 17 for two-dimensional Poiseuille flow using the LBGK collision operator. For less refined lattices, the double precision performance is nearly identical to single precision and both are slightly higher than mixed precision. For more dense lattices the additional memory-bandwidth load of passing double precision operands to the computational routines becomes more important than penalties paid for type conversions and mixed precision outperforms double precision.

3. Stability and Accuracy

In the preceding section, it may have seemed arbitrary to have selected a constant relaxation parameter $\omega = 1.25$. This conclusion is partially correct insofar as there is considerable flexibility as to how this value is picked. We recall from Chapter II that, including effects of scaling in time and space, the fluid viscosity in LBM-units scales by $\frac{\delta_t}{\delta_x^2}$ in accordance with Equation 37. Consequently, if δ_x is reduced by a factor of 2, δ_t must be reduced by a factor of 4. With this refined time step, the number of time steps is increased by a factor of 4 for the fluid simulation, including the time required for the LBM simulation

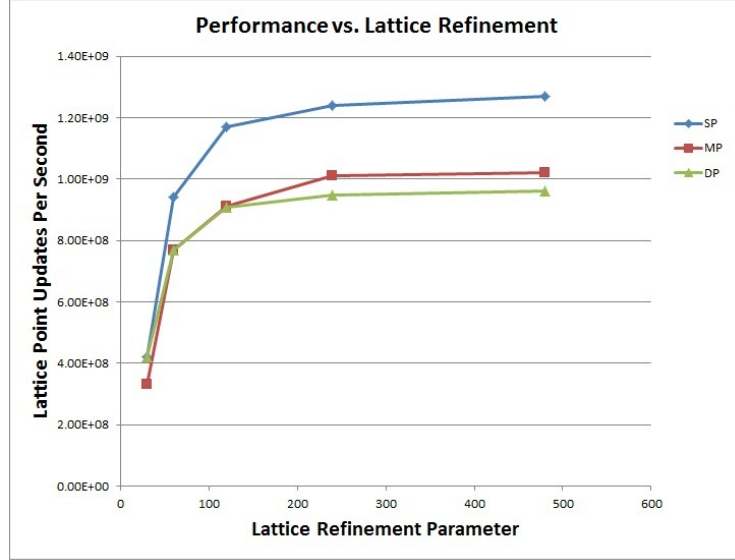


Figure 17: Relative performance of single precision (SP), mixed precision (MP) and double precision (DP) computational routines for Poiseuille flow. The lattice refinement parameter refers to the number of lattice points placed across in the dimension of the channel opening.

to arrive at an equilibrium from non-equilibrium initial conditions.¹ For a given value of ω , this initial instability can last for many time steps. Even for this simple problem geometry, the LBM system does not reach a stable answer for many time steps. An illustration of this is given in Figure 18. This figure shows variation in the horizontal velocity at the center of the channel geometry for lattice density of $N_y = 30$ and 480, respectively. Note the change in time scales for the time-step axis. A more detailed and comprehensive report of the stability properties of LBM along with a comparison between LBGK and MRT collision operators can be found in [33].

¹In this case, transition from zero velocity everywhere in the domain, to the parabolic velocity profile that is the solution.

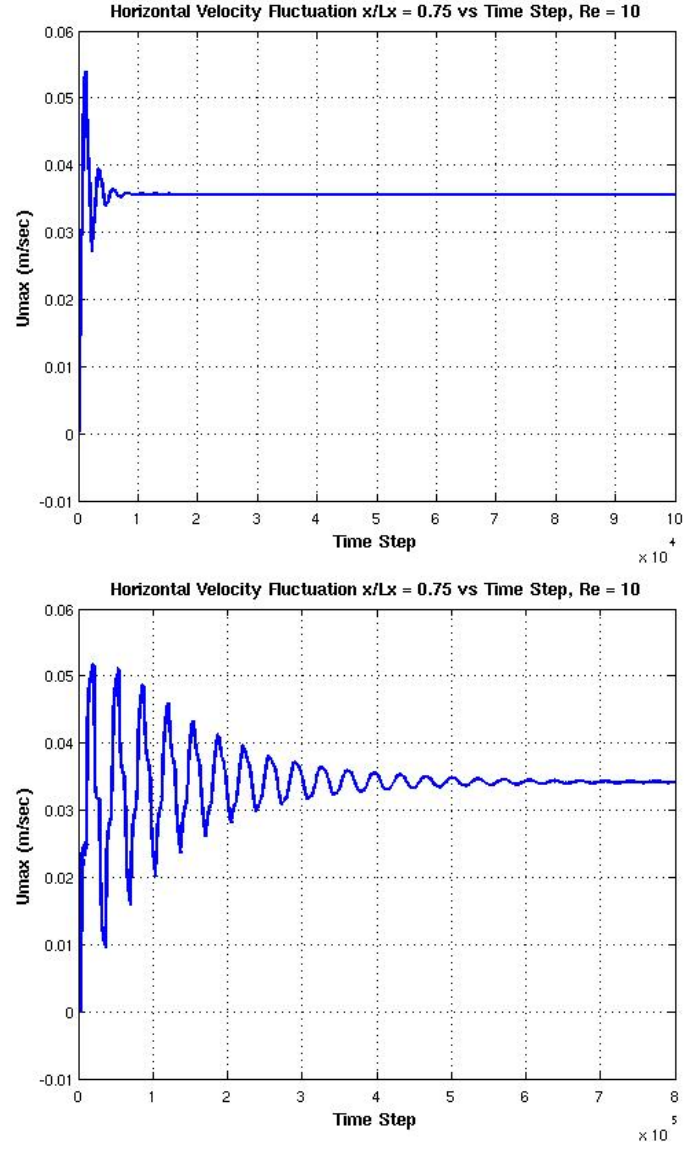


Figure 18: Stabilization time for Poiseuille flow, $Re=10$, $\frac{1}{\tau} = \omega = 1.3$. Top figure, $N_y=30$, bottom figure, $N_y=480$.

B. BACKWARD FACING STEP

The occurrence of flow separation of internal flows by sudden geometric changes is well known and is important to engineering applications; FSI in particular. While the Poiseuille flow test case is convenient for code validation insofar as analytic solutions are known, it does not fully test the ability of the LBM to reproduce correct fluid behavior. It will be shown that for modest Reynolds numbers typical for those that will be used for the FSI applications in this dissertation, the LBM captures flow separation typified by the backward facing step problem accurately.

For this benchmark study, the experimental results presented in [34] will be used. The main benchmark result against which the LBM will be tested is illustrated in Figure 19. The problem set-up is as depicted in Figure 20. For these computations, the inlet boundary conditions are prescribed velocity and outlet is prescribed pressure; both of the Zou/He type. The MRT scheme for D2Q9 is used for bulk dynamics. Measurements were taken based on streamlines computed from the velocity data by Paraview. An example for Reynolds number 100 is provided in Figure 21.

In order to conveniently compare with measured benchmark values, representative data points are pulled from Figure 19 and plotted separately along with the values taken from computed data. For each successively increased Reynolds number, the lattice density and time step were both adjusted so as to maintain a constant relaxation factor $\omega = 1.25$. Results are given in Figure 22. Good agreement can be seen in this case with experimental results.

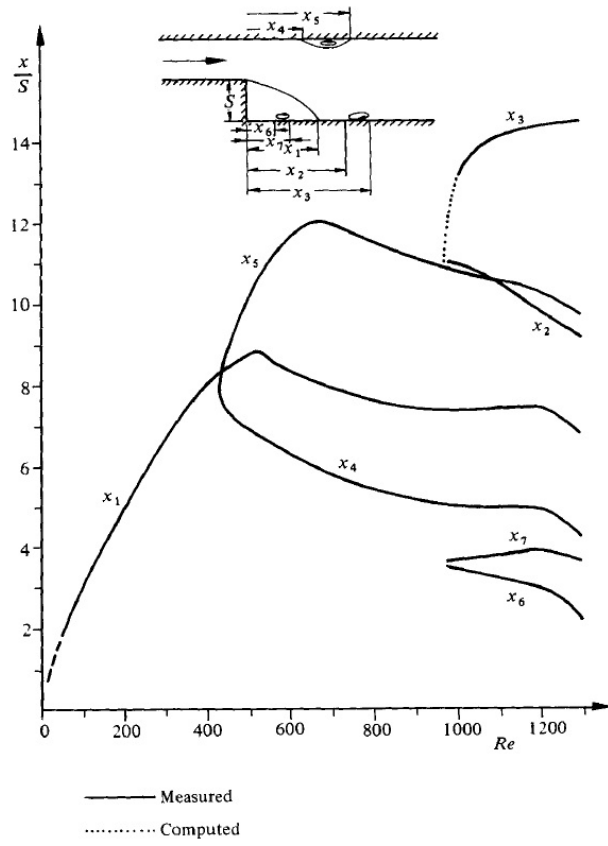


Figure 19: Backward step flow separation behavior. Image taken from [34]

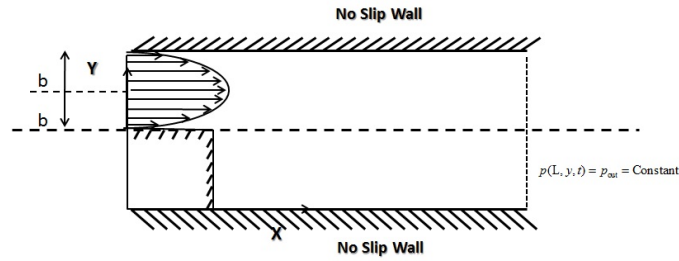


Figure 20: Schematic of domain and boundary conditions for Backward-Step benchmark in 2D.

Backward Step, $Re=100$

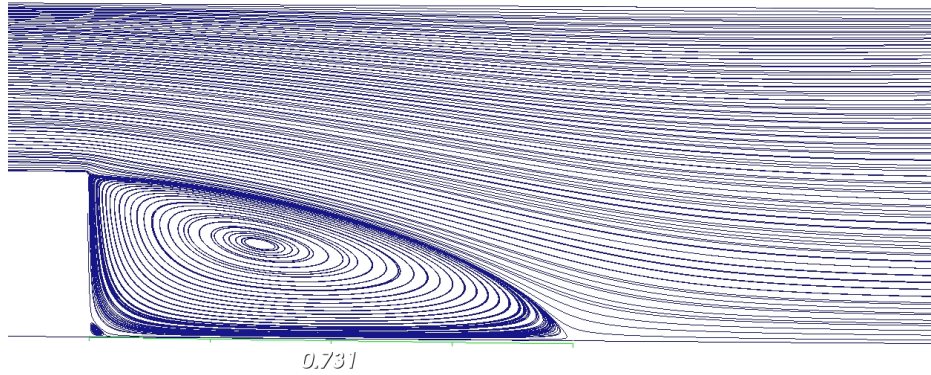


Figure 21: Backward-Step simulation. Step height = 0.25m, outlet width=0.5m, $Re=100$.

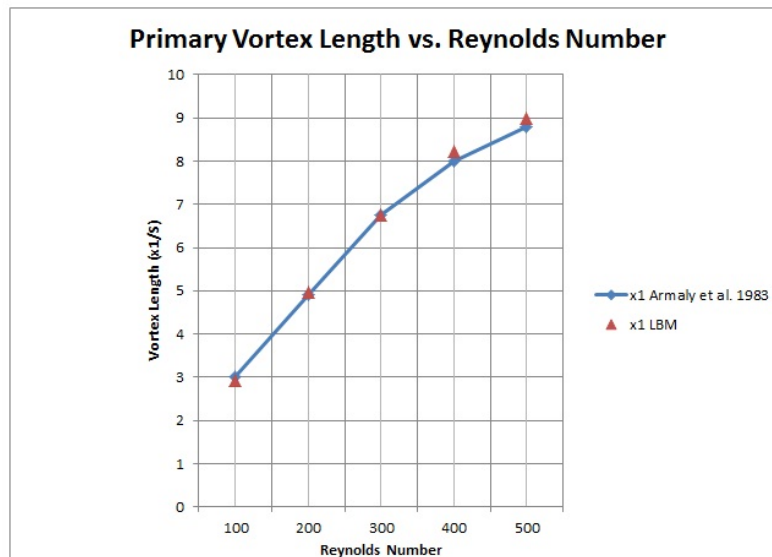


Figure 22: Comparison of primary vortex re-attachment length normalized by step height with results reported in [35].

C. LID-DRIVEN CAVITY

As one validation of the LBM implementation, the software was used to simulate lid-driven flow in two dimensions. A commonly used benchmark for this flow condition is given in [35]. A schematic illustration of the two-dimensional lid-driven cavity problem is given in Figure 23.

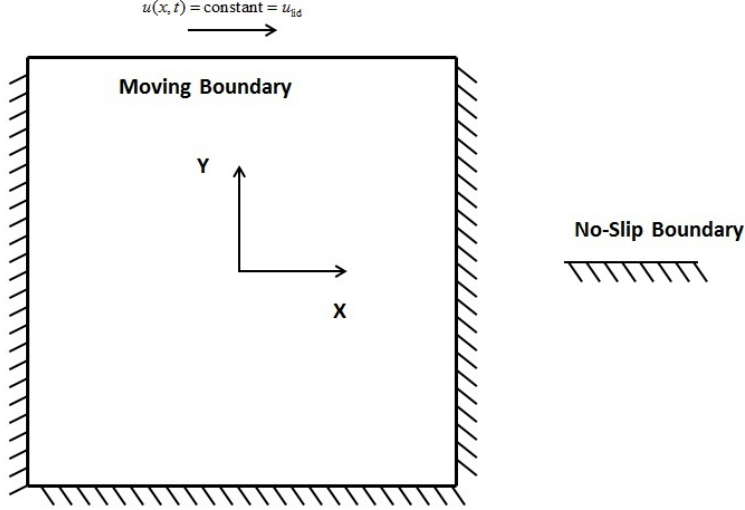


Figure 23: Schematic of the two-dimensional lid-driven cavity problem.

Boundary conditions used for this project are on-grid bounce-back to model no-slip stationary walls. The moving-wall boundary condition is used to model the lid. The lid velocity is set to a constant value in the x direction with the desired speed. The standard benchmark stipulates a Reynolds number of 1000, though other authors have published results at higher Re . In two dimensions, the D2Q9 lattice is used with either LBGK or MRT bulk dynamics.

In Figure 24, a qualitative comparison is made with results reported in [36]. In Figure 25, a qualitative comparison is made of the streamlines, pressure contours and vorticity contours with those published in [37]. Quantitative comparisons are made in the following figures.

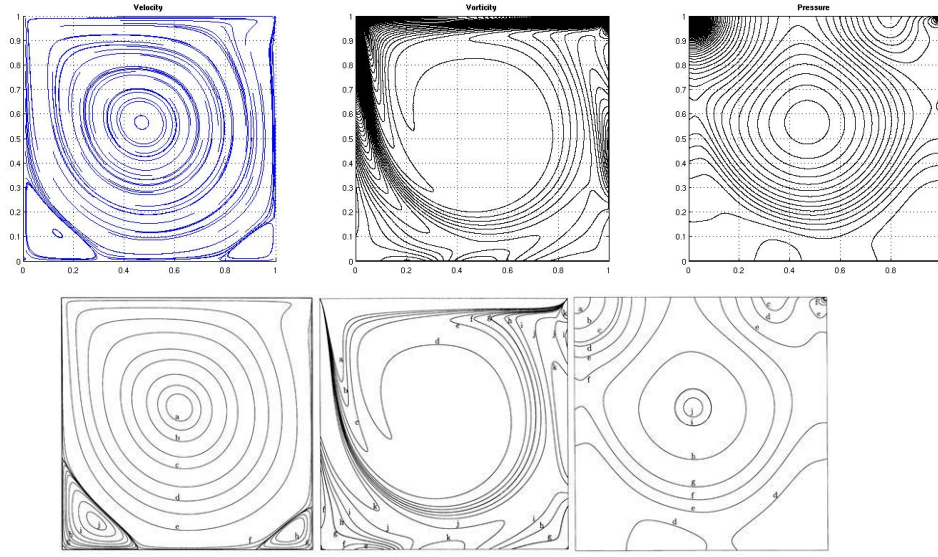


Figure 24: Lid-driven cavity in two dimensions with 1600×1600 lattice showing from left-to-right streamlines, vorticity contours and pressure contours for $Re=1000$. Top set of figures is LBM from this work. Bottom set of figures is from [36].

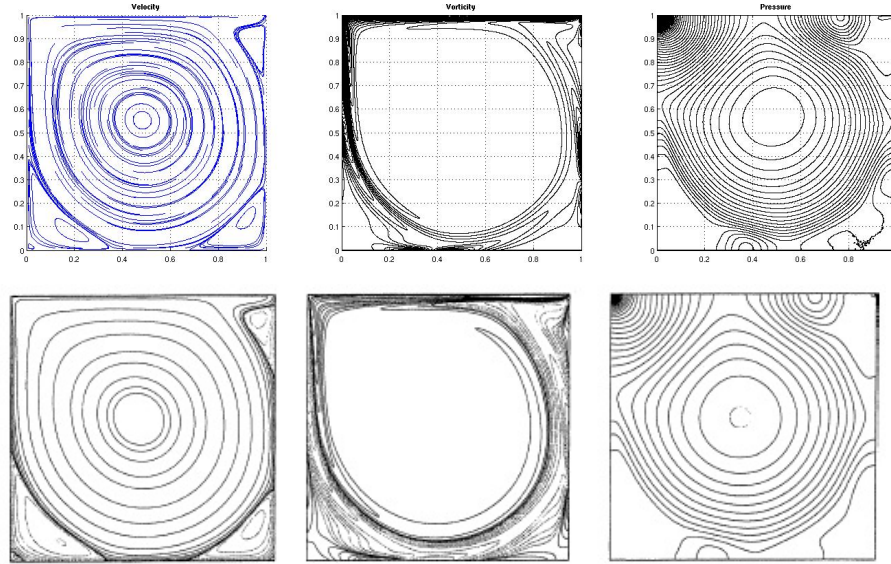


Figure 25: Lid-driven cavity in two dimensions with 1600×1600 lattice showing from left-to-right streamlines, vorticity contours and pressure contours for $Re=5000$. Top set of figures is LBM, bottom set of figures is from [37].

In Figure 26, two samples of velocity are taken in the computed problem domain. The first is the x velocity component sampled along the vertical center-line. As can be seen, good agreement with benchmark values is obtained for all macroscopic fluid parameters.

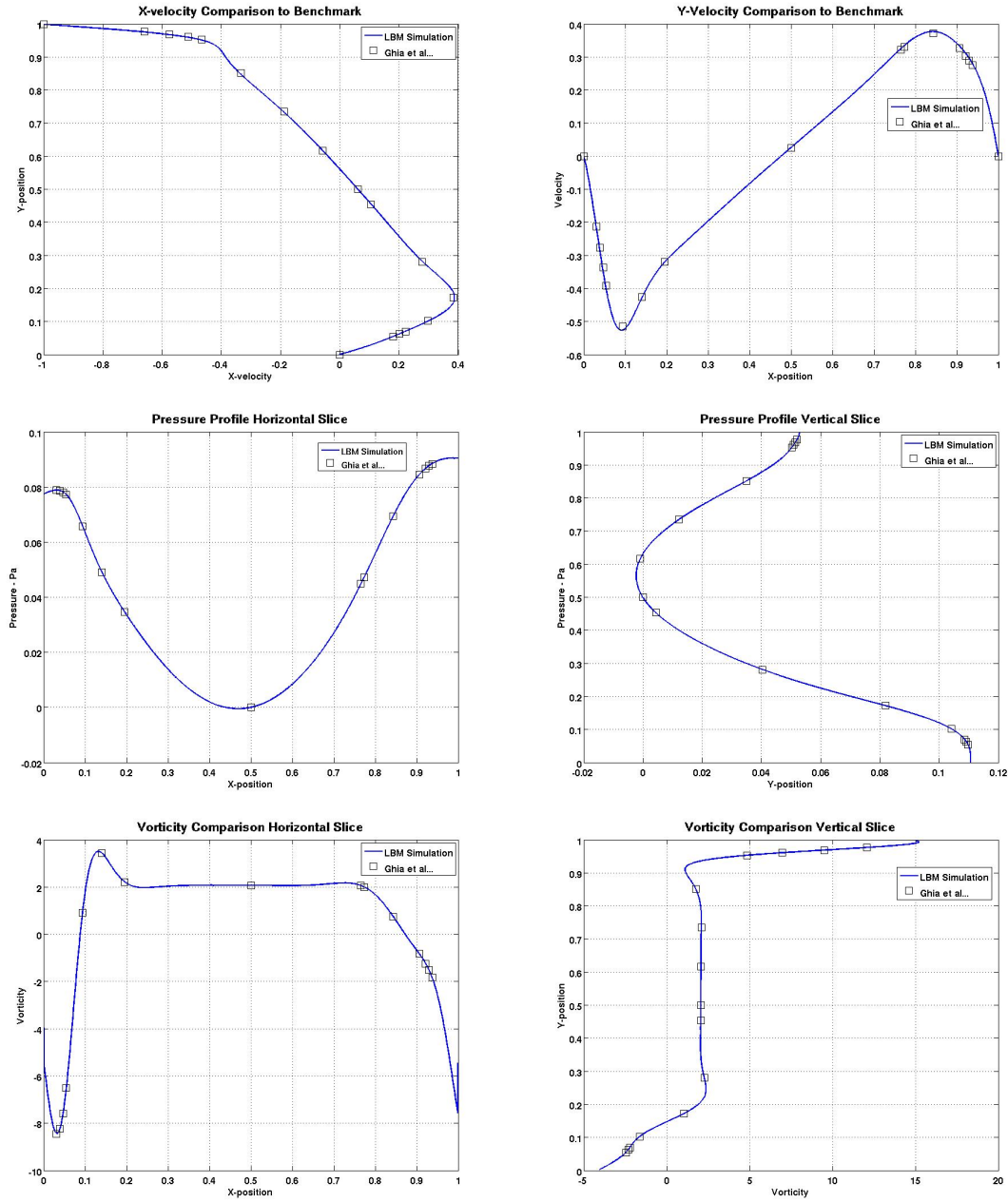


Figure 26: Comparison of velocity, pressure and vorticity to benchmark values for $Re=1000$.

D. CHANNEL FLOW OVER CYLINDER

The flow configuration for this benchmark is illustrated in Figure 27. Constant velocity is specified on the inlet and constant pressure is specified on the outlet. The top and bottom of the domain are simulated as periodic boundaries with the result that the effective domain is a linear array of cylinders in uniform flow. Similar work cited for the benchmarks are published in [38]-[44]. The trailing vortex region for this benchmark was measured visually following flow simulation. Numeric results are given in Table 2 and graphically in Figure 28. It can be seen from the table that the computed values using LBM are comparable to those reported in the literature.

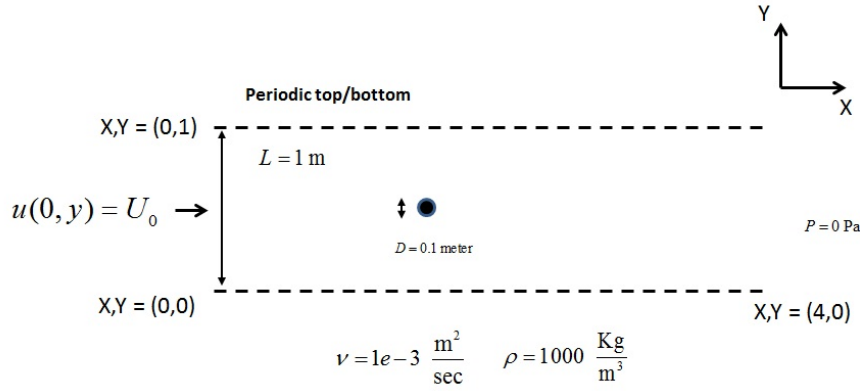


Figure 27: Channel with cylindrical obstacle 2D problem.

Author	Re = 20	Re = 40
Zhou (2012)	0.92	2.20
Calhoun (2002)	0.91	2.18
Rusell (2003)	0.94	2.35
Silva (2003)	1.04	2.55
This work	0.95	2.05

Table 2: Comparison of trailing vortex length to benchmark values.

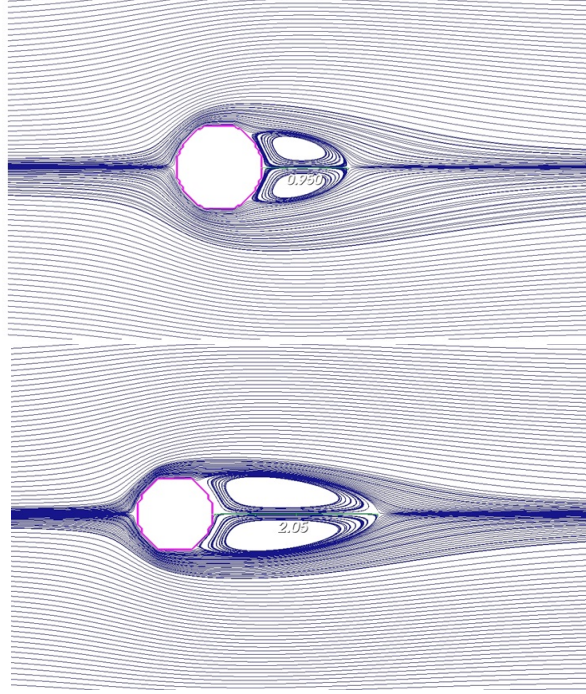


Figure 28: Streamline visualization of trailing vortex at Re=20 (top) and Re=40 (bottom).

Above a Reynolds number of approximately 45, the trailing vortex detaches in an alternating pattern referred to as a Von Karman street. As a last measure, the rate of vortex shedding was measured and the non-dimensional Strouhal number was evaluated with the result compared to the literature. A visualization of the vorticity in the wake of a circular cylinder in channel flow at Reynolds number of 100 is given in Figure 29. Notice the alternating regions of positive and negative vorticity resulting from the vortex shedding alternately from the top and bottom of the cylinder. The equation for the Strouhal number is given in Equation 44,

$$St = \frac{fL_0}{U_0} \quad (44)$$

where St is the non-dimensional Strouhal number, f is the frequency of vortex shedding, L_0 is the characteristic length and U_0 is the characteristic velocity. For this problem, the characteristic length is the diameter of the cylinder and the characteristic velocity is the

average flow velocity. During flow simulation, the drag and lift forces were computed with results presented in Figure 30. The Strouhal number for this simulation was determined by taking the discrete Fourier transform of computed coefficient of lift data and applying this along with U_0 and L_0 in Equation 44. The resulting spectrum is presented in Figure 31. The result is compared with others reported in the literature and shows good agreement.

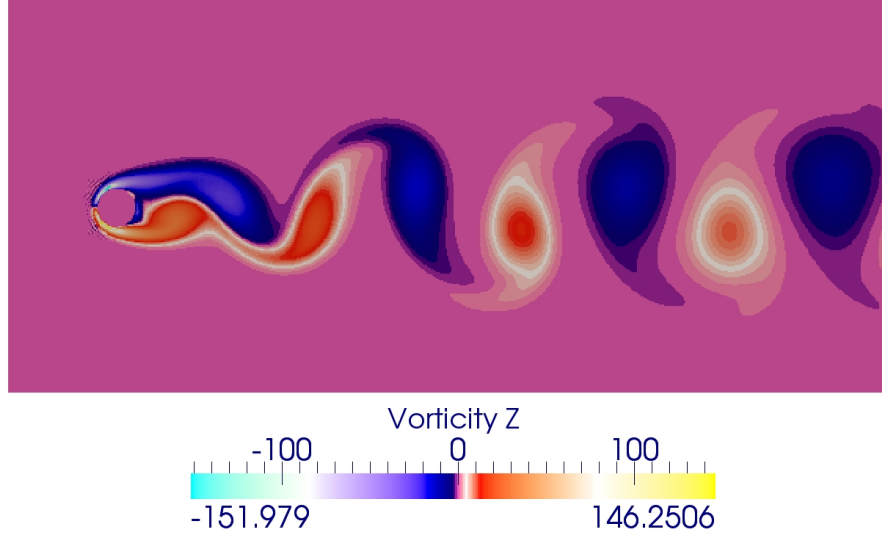


Figure 29: Vorticity plot for cylinder in 2D flow at $Re=100$.

Author	Strouhal number (St)
Williamson (1996)	0.166
Lai (2000)	0.165
Silva (2003)	0.16
Xu (2006)	0.171
Zhou (2012)	0.172
This work	0.169

Table 3: Comparison of Strouhal number to benchmark values.

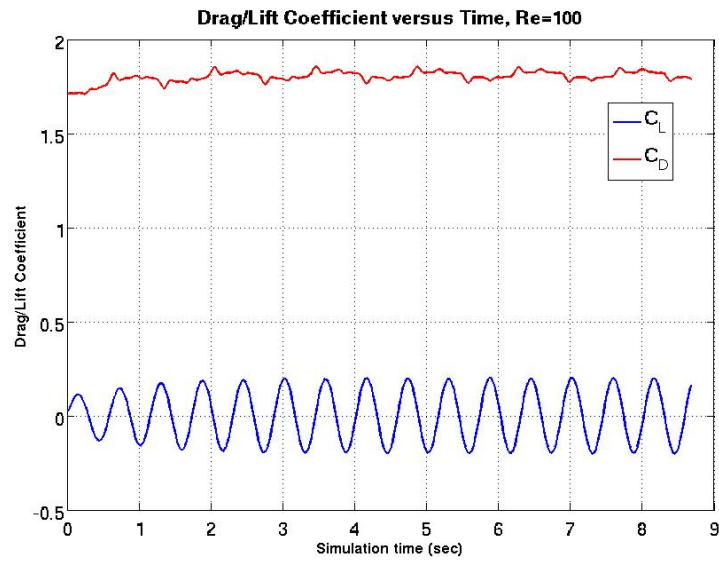


Figure 30: Drag and lift coefficient for cylinder in uniform flow. $Re=100$.

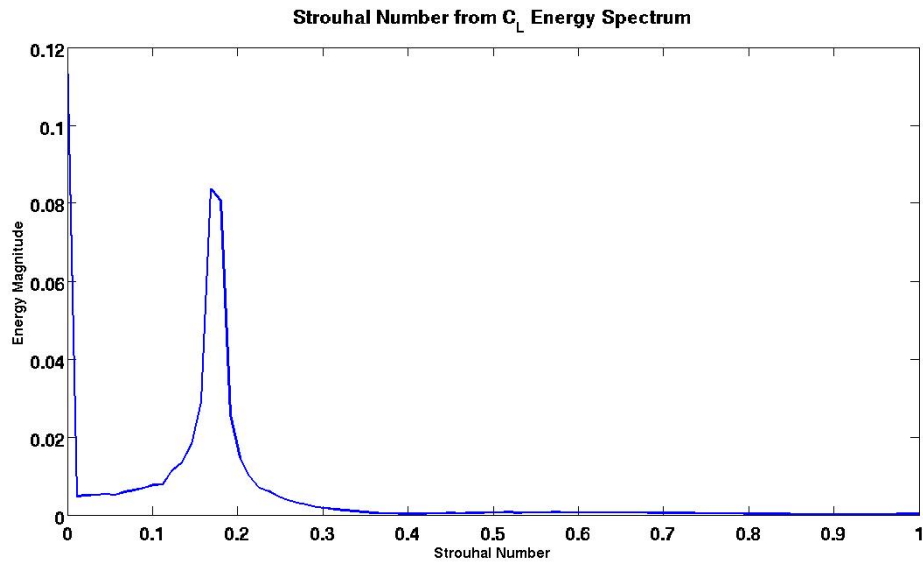


Figure 31: Strouhal number computed from the energy spectra of the lift coefficient at $Re=100$.

THIS PAGE INTENTIONALLY LEFT BLANK

IV. LBM IMPLEMENTATION ON GRAPHICS PROCESSING UNITS

With recent advances in modern GPUs the interest in using these devices for scientific calculations has been growing. In particular, the memory-bandwidth and compute capability of GPUs compared to contemporary CPUs has made their use for LBM applications particularly appealing. Implementations of the LBM using CUDA and the C programming language have been published and the viability of the GPU as an effective platform for executing the LBM has been demonstrated extensively [45]-[50].

In this chapter, the computational requirements for the LBM will be reviewed. Next the NVIDIA CUDA GPU computing platform is introduced and its use for the LBM simulations presented in this work is outlined. Comparisons are made to recently published performance benchmarks for systems with a single GPU. Lastly, multi-GPU implementations of the LBM in hybrid parallel schemes employing CUDA with OpenMP as well as CUDA with MPI will be presented. Performance of these codes are compared with a more conventional parallel implementation with MPI.

A. COMPUTATIONAL REQUIREMENTS FOR THE LBM

Though the operations to be executed for each lattice point during each time step are conceptually straightforward and easy to implement on a computer, it has been well recognized in the literature that the LBM is particularly computationally intensive and memory demanding [51]. Considerations for precision and stability combine to dictate a requirement that a large number of lattice points are needed to effectively discretize a problem domain. Within the classical LBM formulation, all lattice points must be equally spaced implying that LBM solutions for problems with widely varying length and time scales of interest would perform worse than an equivalent finite element method (FEM) or finite volume method (FVM) code where non-uniform meshes may be used. In addition to the large number of lattice points, each lattice point in the domain requires storage for each

value of f_α ; 9 values for the popular D2Q9 lattice, 13–27 values for most commonly used three-dimensional lattices. This is roughly double the requirement for a more traditional solver for the incompressible Navier-Stokes equation [16].

In addition to ample memory and computational capability, the LBM requires very great memory bandwidth so that data can be streamed into the computing cores. For each time step, each value of f_α must be loaded from memory and stored again at least once. The number of floating point operations needed depends upon the choice of boundary conditions and collision operator, but as a rule of thumb, roughly 20 floating point operations are required for every value of f_α . This implies that in order to achieve a computational performance of a high-end CPU, say 500 billion floating point operations per second (GFLOPS), with single-precision arithmetic, the computing device would require a memory bandwidth of at least 200 gigabytes (GB) per second.

The memory-bandwidth and theoretical computational capabilities of selected CPUs and GPUs is depicted in Figure 32. The relationship between achievable computational per-

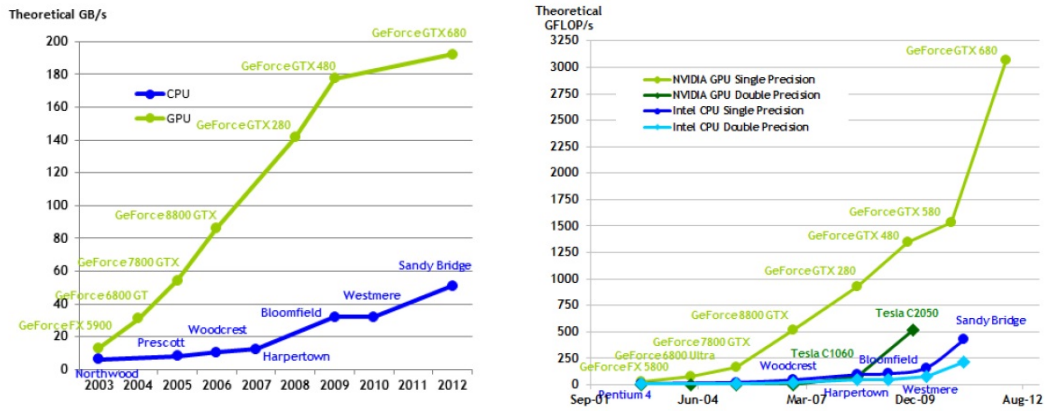


Figure 32: Historical trends for CPU and GPU memory bandwidth and compute performance (From [52]).

formance versus memory bandwidth available for a typical LBM problem is illustrated in Figure 33 along with the computing and memory bandwidth capability of representative hardware. As can be seen, for current CPU and GPU systems, LBM implementations tend

to be memory bandwidth bound rather than computationally bound. This observation has also been reported in the literature [53].

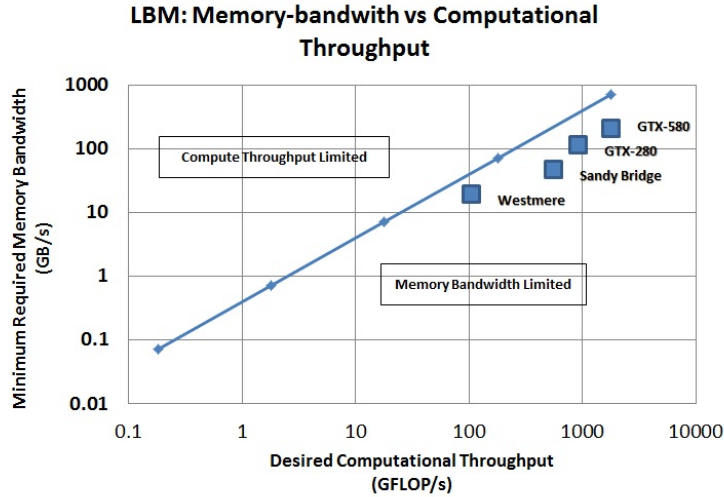


Figure 33: Memory bandwidth requirement versus desired computational throughput for a typical LBM implementation. Modern CPU and GPU hardware are memory bandwidth limited for LBM.

B. AN OVERVIEW OF GPUS AND NVIDIA CUDA

The purpose of this section is to familiarize the reader with the basic concepts of GPU architecture and CUDA programming. The treatment is not comprehensive but is intended to be sufficient so that implementation details and design decisions made in the LBM implementation for this work can be understood within the context of programming on NVIDIA GPUs with CUDA. For a more detailed treatment, the reader is directed to [54]-[56].

1. NVIDIA GPU Architecture

A simplified schematic of the architecture of an NVIDIA GPU is shown in Figure 34. The GPU device is attached to the computer and communicates with external components via the PCIe bus. Within each device is a number of streaming multiprocessors SMs

and within each SM is a number of scalar processors (SPs). The number of SMs per device and the number of SPs per SM varies between generations of GPUs and among particular models in a given generation. Each SM contains a register file used by the SPs as well as a memory space that serves partly as a level 1 cache and a user-managed shared memory. The device also contains a bank of level 2 cache as well as a bank of device memory that is characterized by greater capacity but slower access.

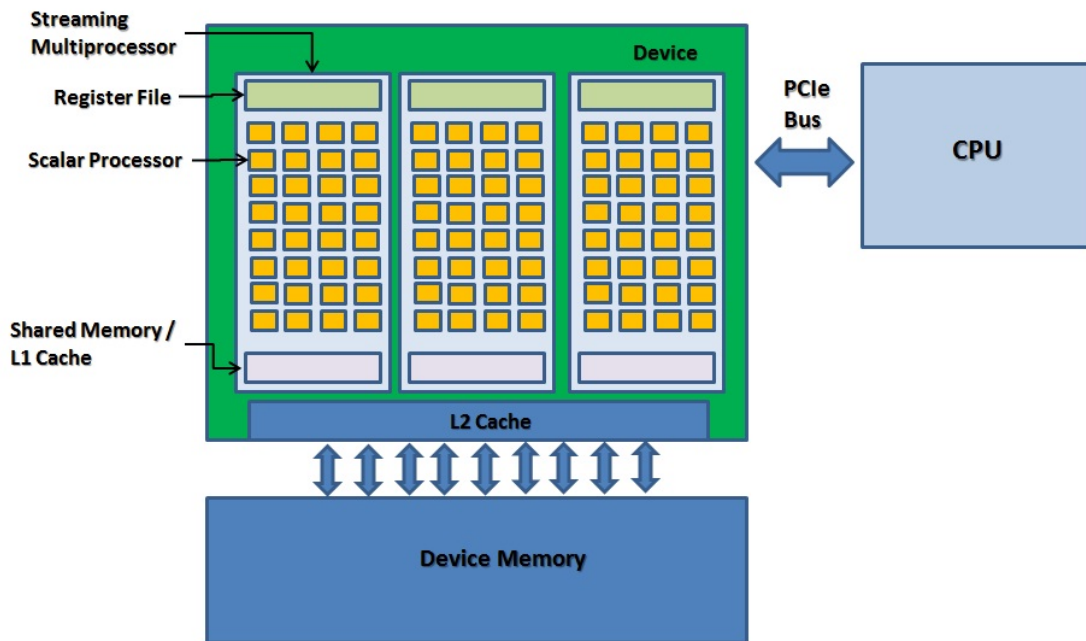


Figure 34: Simplified schematic of NVIDIA GPU.

The NVIDIA GPU is designed for highly multithreaded high-throughput computing. Each scalar processor is assigned a thread for execution. Threads are organized in a hierarchical way into blocks and grids as illustrated by Figure 35. Multithreaded programs executing on the GPU are “launched” as a grid of thread blocks. Grids of threads are composed of a three dimensional array of blocks. The blocks, in turn, are composed of a three dimensional array of threads. The blocks are distributed among the SMs for execution. Each of the SMs execute the threads contained within each thread block independently

and in parallel in groups called thread *warps* comprised of 32 threads each. The individual warps are sent as a group among the SPs contained within an SM for execution. All threads within a warp must execute the same instruction, so the smallest discrete unit of parallelism is the thread warp. Once all of the thread warps in a block are complete, the SM is available to be assigned more blocks. This process repeats until all of the blocks contained in a grid have executed.

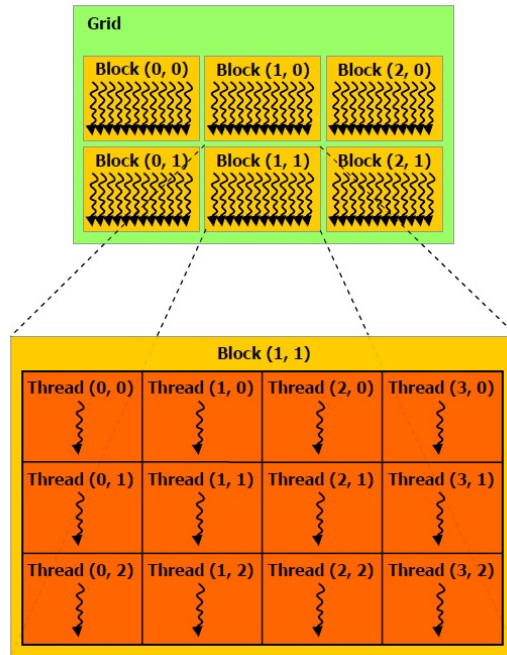


Figure 35: Hierarchy of threads in a CUDA program. Threads are organized into blocks; blocks are organized into a grid (From [52]).

2. CUDA C Programming Model

The CUDA programming model is designed to provide the programmer a way to express their algorithms in a program that can execute on the multithreaded hardware described in the previous section. The complete program is decomposed into those functions that are to be executed on the GPU which are called *kernels*, and the remainder of the program which is simply written in the chosen programming language. The CUDA program-

ming model augments the C programming language with additional syntax and keywords along with an extensive application programming interface (API) enabling the programmer to to effect common programming tasks targeted for the GPU such as device selection, memory allocation, memory transfer and memory de-allocation. Functions that are written for execution on the GPU are denoted with the `__global` qualifier as illustrated in the code listing below.

```
__global void myKernel(float * arg1, const int arg2){  
    //...kernel body...  
}
```

Within the C source code, the kernels are invoked with a special syntax in which the programmer specifies the dimensions of the grid (i.e., configuration of block array within the grid and configuration of the thread array within each block). The syntax is illustrated in the code listing below:

```
dim3 BlockSize(ThreadX,ThreadY,ThreadZ);  
dim3 GridSize(BlockX,BlockY,BlockZ);  
myKernel<<<GridSize,BlockSize>>>(arg1,arg2);
```

where `dim3` is an integer vector defined as part of the CUDA API that is used to express the grid and block dimensions.

From the programmer's perspective, scaling of thread execution among SMs and SPs is transparent. It is not even necessary for the programmer to be aware of how many SMs or SPs are present in a system. Code written for one GPU with a given number of SMs and SPs will run without modification or even recompilation on a GPU with twice as many of each; it will just run faster.

Some restrictions exist in the CUDA programming model. The programmer has no control over the order in which the thread blocks will execute. Additionally, no global thread synchronization within the context of a single kernel is possible. Once started each thread block runs to completion; the programmer can only enforce barrier synchronization for threads within an individual thread block.

Like other shared-memory programming models such as OpenMP, CUDA does facilitate shared variables between individual threads. For CUDA, this is only possible for threads within a single thread block. This is done using the shared memory block within each SM. Any data that must be exchanged with threads outside of the thread block must be done via global memory and, since execution of distinct thread blocks cannot be scheduled by the programmer, it must be done asynchronously.

A programmer planning to use CUDA to obtain high performance must design their programs so as to make maximum use of computing resources while not overloading the available memory bandwidth. Maximizing use of the computing resources means mapping the most fine-grained level of parallelism within the algorithm to the grid structure provided in the CUDA programming model to generate as many threads as possible. Using LBM as an example the choice almost universally made is to assign all of the computations required for a single lattice point to a unique CUDA thread. All of the threads for all of the lattice points would then be mapped into blocks and ultimately a thread grid for execution. For simulations with many lattice points, this will generate sufficient parallelism to keep many of the SMs and their associated SPs busy doing productive work.

Conservation of global memory bandwidth is done in two ways: first, by minimizing the number of global memory transactions; second, by ensuring that the global memory transactions are as efficient as possible by ensuring load and store operations to global memory are coalesced. For GPU programming of the LBM, there is much less agreement in how best to achieve the goal of making best use of available memory resources. This is not surprising since efficient use of memory bandwidth is the most important determiner of program performance. Some of the design alternatives will be discussed in the section on LBM implementation with CUDA.

A great deal of effort is made among researchers to ensure that their programs make the most effective use possible of their GPUs. The resulting codes and algorithms are somewhat more complex than what will be described in this work. Instead of employing every last arcane trick to squeeze the last epsilon of efficiency from the GPU, this work

will demonstrate the effectiveness of straight-forward though efficiently written code that seeks first to embody the most important GPU programming best practices. A collection of these high-level CUDA programming best practices is provided by NVIDIA in [57]. Some of these guidelines are repeated here:

1. Minimize data transfer between the host and the device. Data transfer should be avoided even if it means running some kernels on the device even when they do not show significant performance gains compared to running those functions on the CPU.
2. Ensure global memory accesses are coalesced whenever possible. Sequences of threads in a warp should, whenever possible, access sequential locations of memory. When this is done the reading/writing operations can be done in a single memory access.
3. Minimize the use of global memory. Prefer shared memory access where possible.
4. Avoid different execution paths within the same warp. Use of if-then-else control structures result in the requirement for warps to traverse code segments multiple times as threads within the warp take different control paths. This is termed *thread divergence*.

C. LBM IMPLEMENTATION WITH CUDA

In this section, the implementation strategy employed for this work will be outlined. A great deal of software was written for this work, mainly comprising the multitude of experiments in data layouts, grid setups and register usage strategies aimed at obtaining high performance while maintaining some modicum of code flexibility. In the following sections, both the basic implementation as well as steps taken towards optimization will be reviewed in turn.

1. Basic Implementation

The basic implementation of the LBM on the GPU is discussed in this section. The discussion is broken up into two parts. First, the essential calculations required for the LBM routine are considered. Second, the question of how to best arrange the main LBM variables— f_α for all of the lattice points—in memory.

a. LBM Routine

Every LBM routine must provide for certain identifiable milestones. These are briefly listed below:

- Problem initialization.
- Computation of macroscopic flow properties such as ρ and \mathbf{u} .
- Enforcement of boundary conditions to force the proper flow and solve the correct problem.
- Collision to relax towards equilibrium.
- Streaming to propagate information across the LBM grid.
- Exporting of data to allow post-processing.

Several methods for initializing the values of f_α at each lattice point have been analyzed in the literature [58]. For this work, all lattice points are initialized by setting $\mathbf{u} = 0$ and ρ equal to the nominal density of the fluid to be used in the simulation. Then f_α^{eq} is computed using Equation 10. These tasks can either be done with the CPU prior to copying the lattice data to the GPU or it can be implemented in a separate kernel prior to commencing time stepping.

Computing of macroscopic properties and enforcement of boundary conditions are frequently done in conjunction with the collision step. This is done because the macroscopic properties are often only required, within the context of the LBM simulation, for calculation of f_α^{eq} which is required for collision and, for some schemes, boundary

condition enforcement. To compute macroscopic properties separate from either boundary condition enforcement or collision would require storing the values in global GPU memory. For this reason, in light of the CUDA programming guidance to minimize global memory transactions, the steps of computing macroscopic flow properties, boundary condition enforcement and collision are always done in the same kernel.

The streaming step for the classical LBM is simply a data copy operation. While this is simple to implement, it is the subject of much research as to how to best execute the streaming step in a way that memory accesses are coalesced.

Lastly, any simulation is pointless if there is no way to evaluate the results. For this work, intermediate values for the fluid velocity and pressure field were periodically transferred from the GPU to CPU and written to disk using Visualization Toolkit (VTK) file formats. For FSI computations, displacement, velocity and acceleration data was similarly stored for later post-processing.

b. Data Layout

The two principal alternative data layouts for LBM computations are the so-called AoS or SoA. The two alternatives are illustrated schematically in Figure 36. In AoS, the density distribution values f_α for a given lattice point are assigned in consecutive memory locations. In SoA, the density distribution for all of the lattice points for a given lattice speed are assigned consecutive memory locations; these are followed by the density distribution function for the next velocity and so-on until all of the data has a location.

For LBM calculations conducted on the CPU, it is most appealing use the AoS since this will allow the CPU to access sequential memory locations while accessing the data for a particular lattice point. This will allow for efficient memory transfers as well as effective use of the memory cache hierarchy. In contrast, most LBM implementations on the GPU use the SoA approach. With the SoA, when data is loaded from memory within a kernel, each thread in a given warp reads from consecutive memory locations as illustrated in Figure 37. When loads are coalesced in this fashion, the data is transferred from memory in a single transaction. A similar condition exists during store operations as

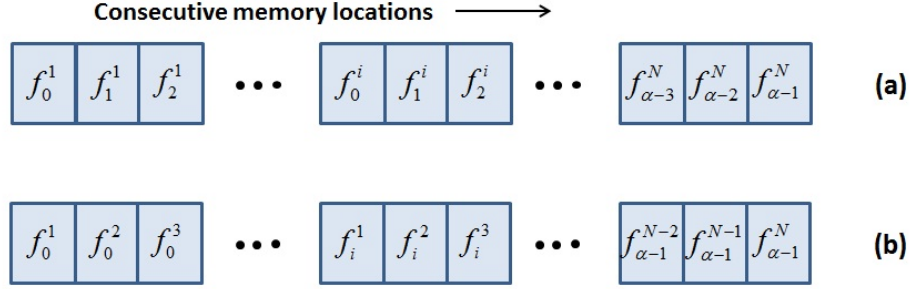


Figure 36: Schematic of data layout schemes. (a) depicts the AoS, (b) depicts the SoA. Superscripts indicate lattice node number, subscripts indicate the lattice velocity.

well. This is in conformance with the guidance to ensure coalesced memory access. As a rule of thumb, using the AoS approach on the GPU penalizes achievable performance by a factor of approximately two.

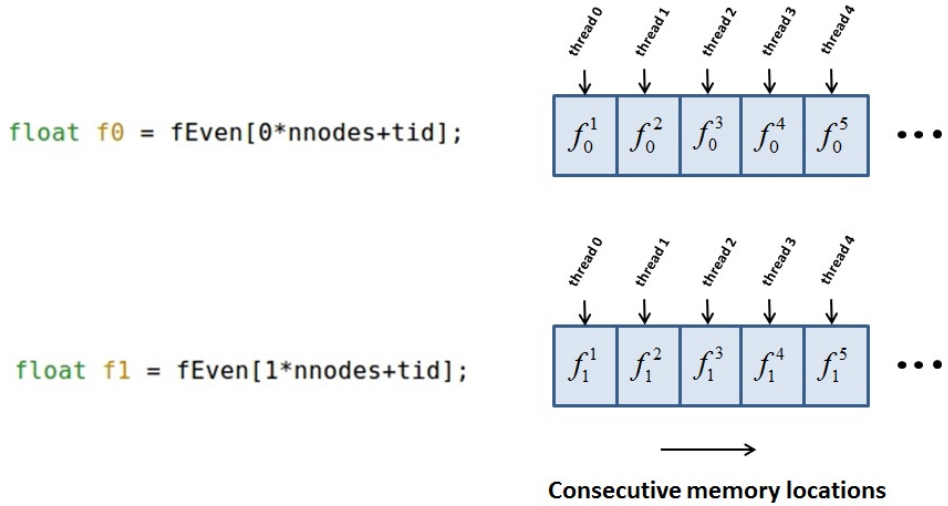


Figure 37: When using SoA, load instructions executed by consecutive threads read from consecutive locations in memory

2. Optimization

Once a basic implementation has been prepared, tested and validated, it is time to look for ways to improve performance. For this work, the optimization strategies taken resulted in a four-fold increase in performance over the baseline GPU-accelerated implementation. The principal optimization strategies fall in the following categories:

- Kernel structure
- Register versus shared memory trade-offs; and
- Thread block dimensions.

The details are discussed in the subsections below.

a. Kernel Structure

For this work, all computations required to execute a single time step on each lattice point are collected into a single kernel. This implies a number of compromises. First, since the order of execution of blocks of threads is outside of programmer control, a second lattice is used so that one lattice is active with each time step. The LBM collision and boundary conditions are enforced on the active lattice and the result is streamed to the alternate lattice. This results in a reduction of memory bandwidth demand by a factor of two from the naive implementation while paying the cost of doubling the memory consumption.

Second, this unified times step kernel structure also imposes a penalty on the modularity of the LBM code. Any alternative selection of boundary conditions or relaxation schemes necessitates construction of a new kernel. This penalty is emphasized by some authors in the literature [50]. It was found during this work that the structure of the kernel itself is modular, and amenable to systematic construction. Individual components of the kernel time-step could be “cut-and-paste” into a basic kernel to provide the desired customization. This is a dubious software engineering practice when done manually; if automated through meta-programming, however, it can become a powerful tool.

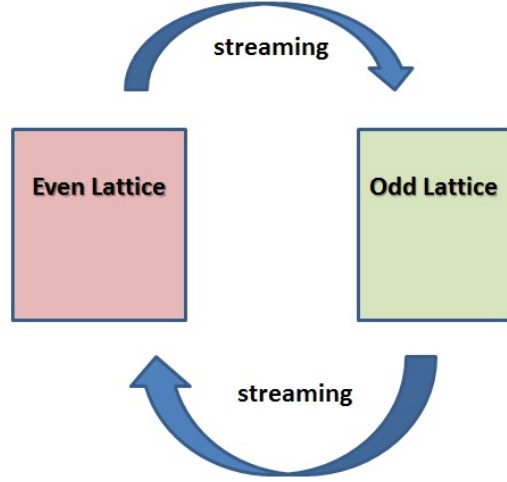


Figure 38: Schematic of the dual lattice scheme used to support a unified time step kernel. On even time steps, the Even Lattice is active and it collides and streams to the Odd Lattice; vice versa for odd time steps.

b. Registers versus Shared Memory

The kernels used in this research made heavy use of registers. Every density distribution function for a given lattice point was assigned its own register value. Additional sets of registers were used for f_{α}^{eq} and any other temporary value needed. The result was that the global arrays holding the values for f_{α} were only accessed at the beginning of the time step as the data is loaded into the SM and at the end of the time step for streaming to the alternate array. This practice resulted in some awkward program structures; since register variables cannot be indexed, all loops were completely unrolled. This negatively impacts program maintainability, however as mentioned previously, these steps are amenable to automation. This register use is a key element to the strategy to minimizing global memory accesses.

An alternate strategy would be to store the density distribution values in shared memory instead of registers. This practice is avoided in this work for several reasons. First, for the NVIDIA GPU architecture has a relatively large 32K register file. Sec-

Memory Type	Bandwidth ($\frac{\text{GB}}{\text{s}}$)
Register Memory	$\approx 8,000$
Shared Memory	$\approx 1,600$
Global Memory	192
Mapped Memory	8 (one-way)

Table 4: Memory bandwidth of various CUDA memory spaces on an NVIDIA GTX-580 GPU

ond, use of shared memory incurs an overhead of integer arithmetic for shared memory array indexing. Third, though the memory bandwidth between shared memory and the SPs is an order of magnitude faster than global memory, it is much slower than the bandwidth between the register files and the SPs [56]. The bandwidth of various CUDA memories is summarized in Table 4. Despite the speed of shared memory, when combined with the integer arithmetic overhead and limited bandwidth, it has been shown that contemporary GPUs are unable to achieve peak performance when using shared memory [56].

The last reason is that shared memory is not used simply because individual values of f_α are often not shared between threads. Shared memory should be utilized for variables that are shared such as $\rho(\mathbf{x}, t)$ in multi-component models, or the relaxation matrix in MRT collision models. In these cases, shared memory is the only option for efficiently exchanging information between threads and this resource should not be squandered when more efficient mechanisms for storing intermediate non-shared data like registers are available.

c. Thread Block Dimensions

Programs written for execution on the GPU are typically very sensitive to the specific layout of the thread grid. The three-dimensional array of thread blocks can have as many as 65,535 blocks in any dimension. The three-dimensional thread blocks are somewhat more limited; for Fermi-class NVIDIA GPUs, the maximum thread block dimension is 1024 and the product of all thread dimensions must be less than 1532 [52].

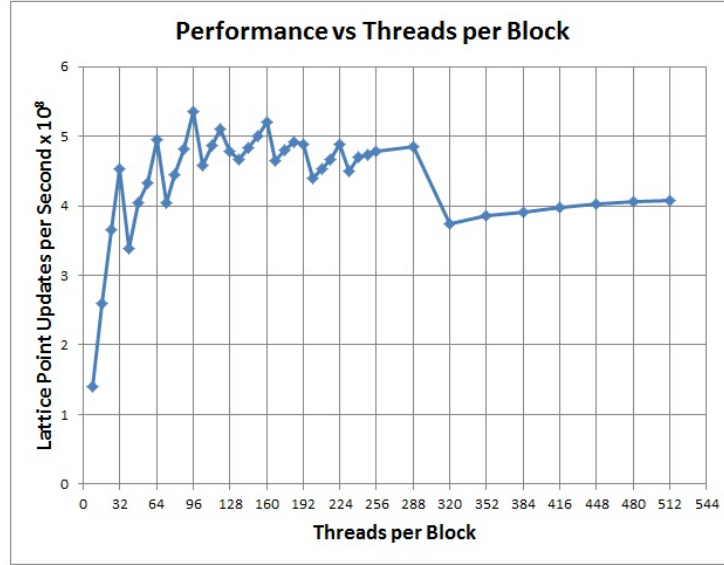


Figure 39: LBM performance on GTX-580 for three-dimension lid-driven cavity as a function of threads per block.

These limits are important and must be respected, but they do not help select the best thread configuration within those limits.

As an experiment, the three-dimensional lid-driven cavity problem is run with a series of one-dimensional thread blocks arranged in a one-dimensional grid. A D3Q15 lattice structure was selected with LBGK collision operator and a $64 \times 64 \times 64$ lattice was used for a total of 262,144 lattice points. The simulation was run on a GTX-580 GPU. The threads per block was varied and the performance for each thread block size is shown in Figure 39. Notice that most of the peaks in the performance plot occur when the number of threads per block is a multiple of 32. This number is important because it implies that all warps within the block will be fully associated with useful work and makes possible fully coalesced global memory reads.

The general trend is lower performance for very small thread blocks and also lower performance for very large thread blocks. For the small thread block sizes performance suffers because, with a limitation of only 8 blocks assigned to each SM, an insufficient number of total threads is kept in flight to hide data access latencies and exploit

the full parallelism of the GPU. With very large thread blocks the reduced performance is a combination of a reduced number of blocks per SM due to register resource limitations resulting in an overall reduction in the number of threads in flight and accompanying loss of parallel performance. With an intermediate number of threads which is also a multiple of 32, more blocks are assigned to each SM, more total threads are kept in flight, SMs have adequate resources to service the threads that are assigned to them.²

Though this was just one example case, the general trends are the same for other LBM solvers developed for this work. As a summary for thread block selection, the following summary is offered for use as a guideline.

- Choose thread block size that is a multiple of 32. This will ensure all thread warps are associated with useful work and allow for efficient memory access.
- Choose a thread block size that is large enough to ensure enough threads are in flight to hide memory access latencies.
- Choose a thread block size is not too large so that an individual SM has adequate resources to execute at least one block at a time.
- For most problems, a good starting point is 128 threads per block.

These guidelines may be effective as a starting point for testing, but not as a rule that may be used blindly. Ultimately, there does not appear to be an alternative to experimentation to find the thread block size that is best for a given implementation of a given problem.

D. PERFORMANCE BENCHMARK–3D LID-DRIVEN CAVITY

In order to compare the effectiveness of the implementation strategies adopted for this work, a three-dimensional lid-driven cavity problem was selected as a benchmark.

²The main concern with too many threads is register spillage. If there are more register variables declared in a kernel than can be accommodated by the register file, these excess variables are “spilled” to local memory. Local memory is private memory to each thread block but physically it is located on device global memory. Despite the use of level 1 and level 2 caching on new generation GPUs, performance is degraded when this happens.

Device	GTX-260	GTX-295	GTX-480	GTX-580
Number of CUDA cores	192	240×2	480	512
Global Memory (MB)	896	896×2	1536	1536
Memory Bandwidth (GB/s)	111.9	111.9×2	177.4	192.2
Estimated Peak Performance (Gflops)	805	805×2	1345	1581

Table 5: Properties of GPU devices used in benchmark computations in Figure 40

Three comparable works recently published in the literature will be used as comparisons [49], [50] and [45]. In order to make a more fair comparison between all of the results, the reported performance figures will be normalized for memory bandwidth capability for the GPU device on which each comparable result was computed. The relevant characteristics of these devices are listed in Table 5. The normalized performance is shown in Figure 40.

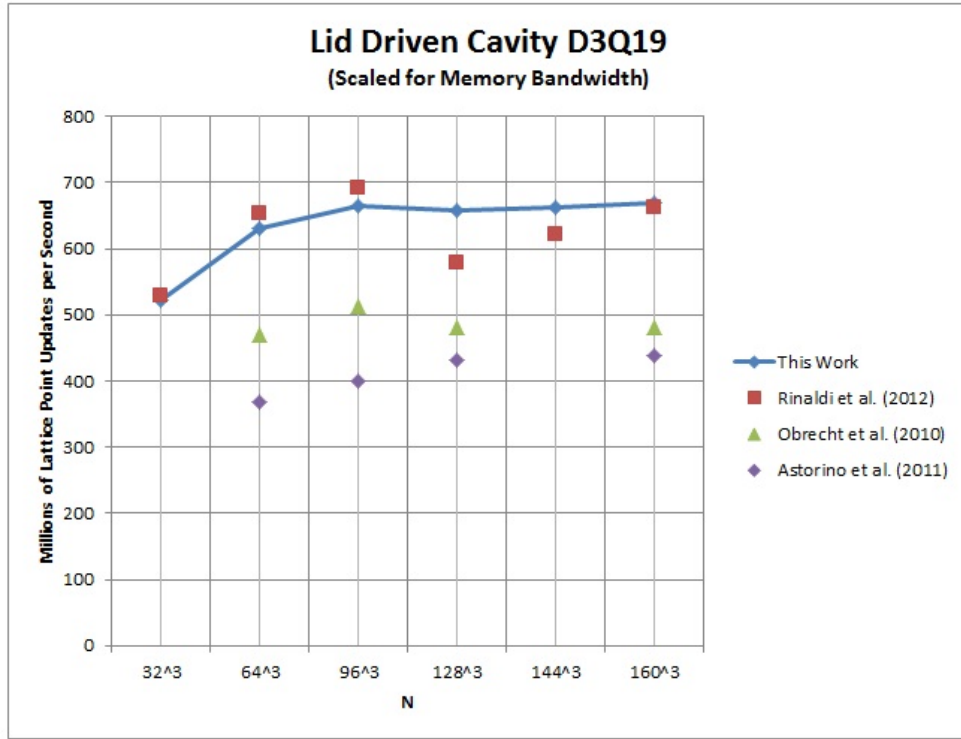


Figure 40: Performance benchmark for LBM on a 3D lid-driven cavity scaled for device memory bandwidth.

It can be seen from Figure 40 that the result of this work is comparable to or better than other recently reported implementations. It is somewhat surprising that the results reported by Astorino et al. in [50] are so poor. In their paper, emphasis is made on the modularity and generality of the C++ implementation. While most implementations, including this work, combine all elements of a LBM time step within a single kernel, the work described in [50] is modular in the sense that computations concerning boundary conditions, collision and streaming are separated into separate kernels that can be individually maintained. While it is conceded in this work that software engineering considerations such as maintainability and ease of future expansion are laudable, those considerations often take a back seat to performance due to the higher demands on memory bandwidth due to the need to store intermediate variables.

In order to achieve the best performance for each problem size, the number of threads per block must be adjusted accordingly. The dependence of execution performance on the thread block size is illustrated in Figure 41. Using 96 threads per block performs well for all problem sizes, while the use of 256 threads in a block performs very poorly for all problem sizes.

E. HYBRID PARALLEL LBM

Though excellent execution performance on LBM problems can be achieved when the program is executed on a GPU, it is inevitable that the need will arise to perform simulations for which the basic data variables are too numerous to store in the global memory of a single GPU. The programs ultimately have to scale to multiple devices. For this work, the GPU-based implementation with CUDA on an NVIDIA GPU is coupled with traditional parallel programming methodologies. First, the GPU-accelerated LBM code will be augmented with OpenMP directives to allow execution on multiple GPUs installed on a single workstation. Second, the GPU-accelerated code will instead be employed within a distributed programming environment using MPI.

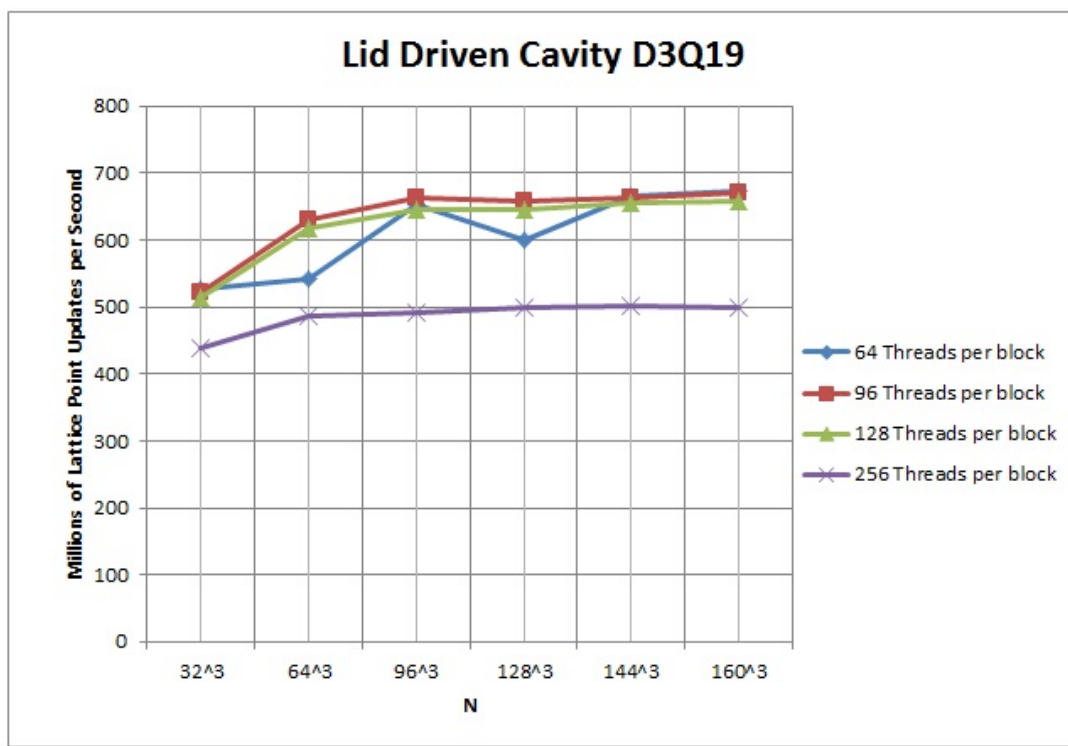


Figure 41: LBM on a 3D lid-driven cavity with various number of threads per block.

1. CUDA with OpenMP

When multiple GPUs are used, it may be taken to imply that a distributed memory programming model must be employed. Since none of the devices are capable of handling the entire domain, it is logical that the domain must be partitioned with relevant data distributed among the devices.³ However, for workstations equipped with multiple GPUs, the use of CUDA alongside of OpenMP is an attractive option. Since all of the devices are physically located on the same machine, it is convenient to use the shared-memory paradigms of OpenMP rather than explicitly dealing with the message passing API of MPI.

For this work, a workstation equipped with six NVIDIA C2070 GPUs is employed to execute the three-dimensional lid-driven cavity problem with both CUDA and OpenMP. The problem domain is partitioned geometrically among the available devices and inter-partition boundary data is exchanged between the devices in a peer-to-peer mode. Though the bandwidth capability of the PCIe bus is still a limitation, the demand is comparatively low since only boundary data is exchanged.

Performance results for the three-dimensional lid driven cavity problem is shown in Figure 42. For the simulation a D3Q15 lattice was used with LBGK collision operator. The lattice size was set to 500x500x500 lattice for a total of 125 million lattice points. It can be seen that the scaling is somewhat less than linear. This is attributed primarily to the fact that this particular multi-GPU implementation that does not overlap computations with peer-to-peer communications. Future CUDA/OpenMP will incorporate this optimization and is expected to improve scalability.

2. CUDA with MPI

Though using CUDA in conjunction with OpenMP makes it possible to employ multiple GPUs to bring larger problem sizes into reach, this solution still has limitations in

³Strictly speaking, this is not true. With recent GPUs operating computers with sufficient physical memory and a 64-bit operating system, it is possible to maintain the entire problem in the (usually larger) CPU system memory with each sub domain logically mapped to the GPU that will be assigned to carry out its computations. Unfortunately, the memory transfer overhead across the comparatively slow 8 GB/sec PCIe bus from the CPU memory to the GPU renders this convenient programming technique impractical.

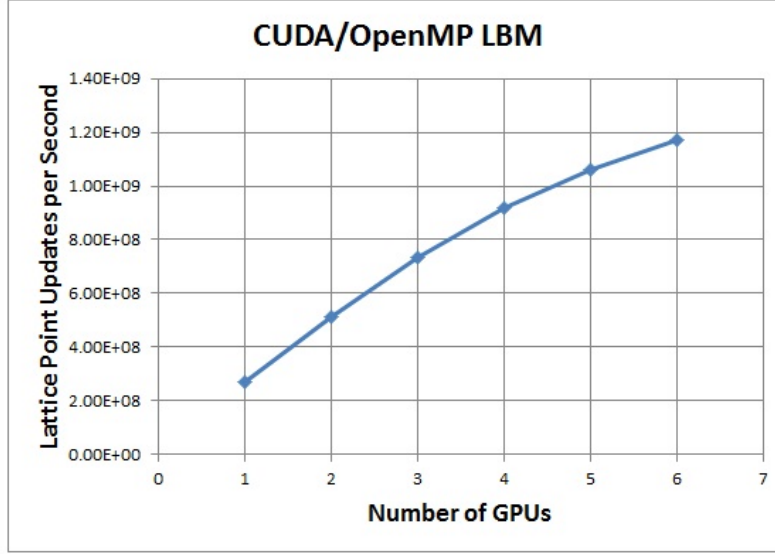


Figure 42: Lid-driven cavity using a D3Q15 lattice with 500^3 points using CUDA and OpenMP.

scalability. While it is conceivable that workstations will be constructed capable of hosting more than six GPUs and that each GPU will gradually increase its memory size thus be capable of handling larger problems, the need currently exists to model fluid problems using LBM that require billions of lattice points and must be simulated for millions of time steps. In order to scale to these problem sizes, it is necessary to develop LBM codes that can be deployed cooperatively on an arbitrarily large number of nodes.

The standard programming paradigm for programs of this type is to use a distributed parallel programming model based on MPI. When developing a program that uses MPI it is critically important that the algorithm is implemented such that necessary computations are interleaved with any communication requirements that may exist for the problem. In addition to high-performance CPUs, the other key feature that the hardware on which the code is to run must possess is high-speed interconnects. For this work, a test code that used only MPI with CPUs was developed to analyze three-dimensional Poiseuille flow. The lattice points throughout the domain were partitioned geometrically and distributed as evenly as possible to all available processors.

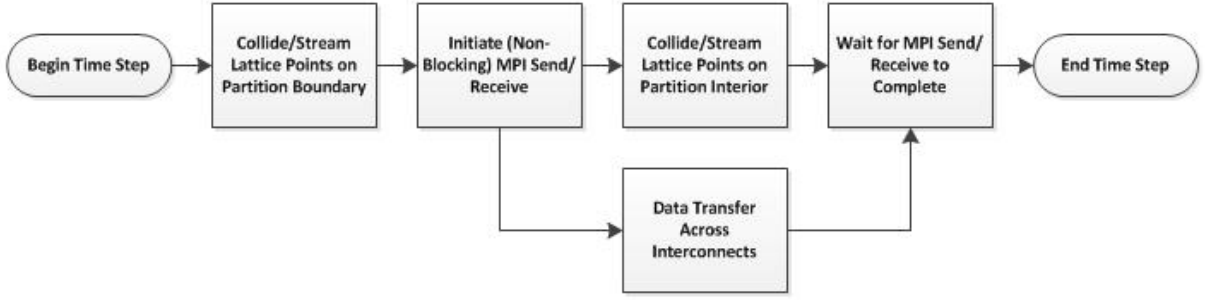


Figure 43: Schematic LBM time step for distributed computing with MPI. Scalability is achieved by interleaving communication with computation.

To allow for scalability, the lattice points assigned to each processor were further partitioned into boundary points and interior points. The LBM time step computations were performed for the boundary points in each sub domain first. Once these computations were complete, the values of f_α that are streamed out of each sub domain, and correspondingly streamed in to neighboring sub domains, are exchanged using non-blocking MPI communication protocols. Concurrent with this communication process, all processors executed the computations for the LBM time step on their interior lattice points. The overall process is illustrated in Figure 43. The performance results for *weak scaling* are presented in Figure 44. For each test case, the lattice size was adjusted to maintain a constant 40x40x16 lattice size for each MPI process.

A notable result that can be drawn from Figure 44 is that a large number of CPU cores are required to achieve performance comparable with a single high-performance GPU. Recalling that the LBM is a memory-bandwidth constrained problem, the explanation for the large number of CPU cores required is the comparatively limited memory bandwidth that each CPU core has available to it. The hardware on which this test was run was a cluster containing 32 dual quad-core Xeon processors. Though they were interconnected with high speed interconnects, each pair of CPUs shared an aggregate memory bandwidth of only approximately $8 \frac{\text{GB}}{\text{s}}$. Comparing this with the $192 \frac{\text{GB}}{\text{s}}$ memory band-

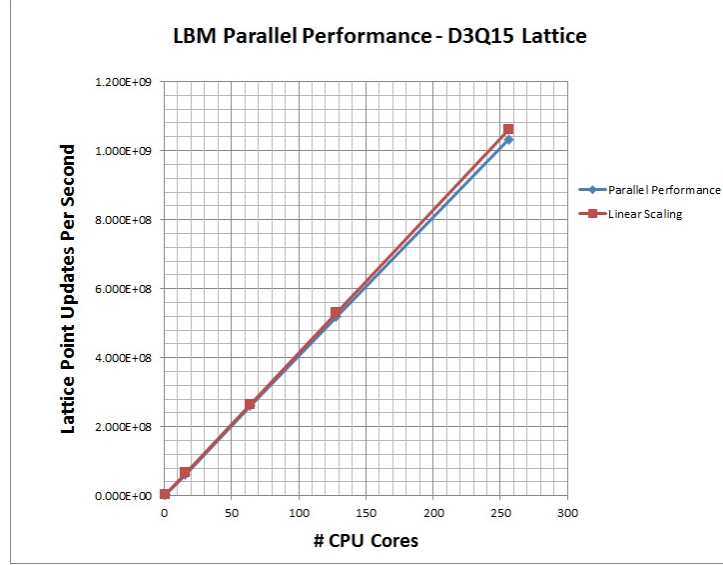


Figure 44: Weak scaling using MPI for LBM simulation of three-dimensional Poiseuille flow.

width of an NVIDIA GTX-580 GPU, having a memory bandwidth advantage of 24 to 1. In this light, it is not surprising that nearly 200 CPU cores were required. It is conceded that higher performance computer systems would have yielded better CPU results.

The key insight that this work seeks to demonstrate is that the GPU brings *concentrated* scalable performance. A collection of GPUs which individually have high memory bandwidth, coupled with high-speed interconnects, can effectively combine their aggregate memory bandwidth and compute capability using fewer devices than is necessary with CPUs. This will only remain true so long as GPUs maintain their overwhelming superiority in memory bandwidth. When that advantage is lost, the GPUs will also have lost their advantage for high performance scientific computing.

To demonstrate the scalability of a hybrid parallel LBM implementation with CUDA and MPI, the same three-dimensional Poiseuille flow was tested on a system with two nodes and two GPUs per node. The results are presented in Figure 45. In this instance, the results are not as encouraging as that obtained using CUDA and OpenMP. This is attributed at least in part to the fact that the CUDA/OpenMP case was able to take advantage of highly

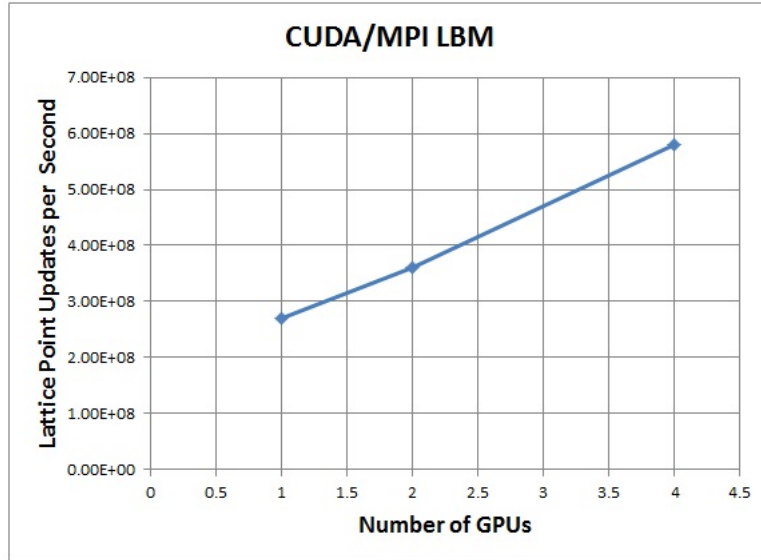


Figure 45: Weak scaling using CUDA and MPI for LBM simulation of three-dimensional Poiseuille flow.

efficient peer-to-peer memory transfers to exchange boundary data. Future revisions to the CUDA API are expected to inter-operate with “CUDA-aware” MPI implementations that will allow, at least from a programmer’s perspective, seamless peer-to-peer memory transfers among GPU devices associated with different MPI processes. It is expected that this feature will improve the scalability of CUDA/MPI hybrid parallel programs.

V. FLUID-STRUCTURE INTERACTION WITH LBM

The principle goal of this research is to investigate the use of LBM for FSI. With a working collection of LBM tools to model a variety of flow conditions in both two and three dimensions it is necessary to couple these tools with the requisite structural models to analyze FSI. Following a brief literature review, the coupled FSI problem will be explored in turn for the 2D and 3D case. The chief products of these investigations are:

- A collection of example problems to be compared with previous work and established benchmarks. Each example problem illustrates qualitatively the coupled interaction between the fluid flow and a linear elastic structure with small displacements.
- A novel algorithm for exploiting task-level parallelism inherent in the FSI problem that exploits both the CPU as well as the GPU to make best use of computational resources and achieve high performance.

Despite these advances, significant work remains to be done in this area in order to allow reliable and effective FSI over a range of interesting problem domains. In particular, geometric and material nonlinearity must be incorporated into the material model in order to quantitatively match benchmark data. Additionally, in order to accommodate the large structural displacements, the LBM model must be further expanded to account for lattice points transitioning from the fluid domain to that subdomain covered by the solid when the structure undergoes large displacements.

A. INTRODUCTION AND LITERATURE REVIEW

The interaction of fluid flow with elastic structures and suspended particles are commonly encountered problems in many practical engineering applications. Use of the LBM for the fluid modeling is common, nonetheless to the best the author's knowledge no substantial work has been done to apply LBM to solve the equations of structural dynamics.

Consequently, several methods have been proposed to couple the LBM with more traditional structural dynamics solvers in order to collectively capture both the fluid and structural dynamics aspects FSI problems.

Some recent authors, such as [59], [60] and [61], have used the immersed boundary (IB) method along with LBM. In an IB method, the fluid problem is solved over a fixed Eulerian grid that covers the entire domain. The immersed boundary is solved on a moving Lagrangian array of points overlying a portion of the Eulerian grid. The force that the fluid exerts on the moving boundary is projected onto the Lagrangian node points by use of the Dirac delta function as described in [62]. This solution procedure has been extensively used for studying FSI applications, particularly for biological flows [63].

While the IB method has been popular for modeling of highly flexible structures, a common methodology for multibody coupling with the LBM is the discrete element method (DEM). This method combines problems addressed by the coupled IB and LBM solvers, and indeed, use the same methods for hydrodynamic coupling between the fluid and solid, but also account for the solid body-to-body interactions and has been extensively used for particle and granular flow problems. A succinct review of the use of LBM and DEM is provided in [64]. As a few examples, this approach has found use in investigation of sedimentation of particles in fluid at low Reynolds numbers [65], particulate flows [66], and particle transport in turbulent fluid flows [67].

The FEM has a long history of use for problems in both structural and fluid dynamics. As can be expected, the FEM has also been applied to FSI problems where the FEM is used in both the fluid and solid domains [68], [69] and [70], for example. In this work, the advances in coupling LBM with FEM for structural dynamics presented in [28] will be used as a starting point for further FSI studies.

B. FORCE EVALUATION

All aforementioned approaches to coupled FSI problems share the issue of needing to determine how forces and momentum inputs from one domain are to be transmitted into

the other. For monolithic approaches, such as using FEM both for the fluid and structural domains, the transfer of this data may be a natural part of the discretization and satisfaction of continuity equations. For the coupled LBM and FEM approach undertaken in this work, it is necessary to obtain the force that the fluid imparts upon this structure at the fluid-solid interface. Two approaches will be discussed in this section:

1. Stress Integration Approach; and
2. Momentum Response Approach

1. Stress Integration Approach

This method was introduced by He and Doolen in [71], where they evaluated the forces on a cylinder in channel flow by integrating the total stresses on the surface of the cylinder by evaluating Equation 45,

$$\mathbf{F} = \int \mathbf{n} \cdot \left[p\mathbf{I} + \rho\nu \left(\nabla\mathbf{u} + (\nabla\mathbf{u})^T \right) \right] dA \quad (45)$$

where \mathbf{F} is the force vector, \mathbf{n} is the outward facing normal of a the solid surface, and ν is the kinematic viscosity.

The first term of Equation 45 is easy to evaluate within the LBM framework using the simple relation of Equation 13 from Chapter II. The second term in Equation 45 is the deviatoric stress for incompressible flow as given in Equation 46.

$$\tau_{ij} = \rho\nu \left(\nabla\mathbf{u} + (\nabla\mathbf{u})^T \right) \quad (46)$$

Equation 46 can be evaluated by computing the macroscopic velocity throughout the domain using Equation 12, then a using a discrete differencing scheme to compute the spatial partial derivatives and evaluate τ_{ij} with given values of viscosity. This methodology does not sit well with the general theme of LBM whereby computations should be performed locally to a single lattice point. In keeping with the general theme of locality, in LBM τ_{ij} is

computed using the non-equilibrium portion of the particle density distribution function; $f_{\alpha}^{\text{neq}} = f_{\alpha} - f_{\alpha}^{\text{eq}}$. In the case for a D2Q9 lattice, at each lattice point this is done using Equation 47

$$\tau_{ij} = \left(1 - \frac{1}{2\tau}\right) \sum_{\alpha=1}^8 [f_{\alpha}(\mathbf{x}, t) - f_{\alpha}^{\text{eq}}(\mathbf{x}, t)] \times \left(\mathbf{e}_{\alpha i} \mathbf{e}_{\alpha j} - \frac{1}{2} \mathbf{e}_{\alpha} \cdot \mathbf{e}_{\alpha} \delta_{ij}\right) \quad (47)$$

Once the integrand for Equation 45 is computed, executing the integral can be done numerically with, for the D2Q9 lattice with Equation 48.

$$\mathbf{F} = \sum_{\alpha=1}^4 \mathbf{e}_{\alpha} \cdot \left[p \mathbf{I} + \rho \nu \left(\nabla \mathbf{u} + (\nabla \mathbf{u})^T \right) \right] \delta x \quad (48)$$

In summary, to use the stress integration approach for evaluating fluid forces on a structure, given fluid viscosity and the current set of density distribution functions f_{α} :

1. Compute density using Equation 11.
2. With this density, compute pressure using Equation 13.
3. Compute macroscopic velocity using Equation 12.
4. Compute f_{α}^{eq} using Equation 10.
5. Compute local deviatoric stress via Equation 47.
6. Compute force from surface stress with Equation 48.

2. Momentum Response Approach

Instead of the stress integration method, a momentum exchange method, developed by Ladd in [72], can be used to compute the fluid force on closed surfaces suspended in the flow field. In this method, the total force acting on a solid body is obtained by Equation 49,

$$\mathbf{F} = \sum_{\text{all } x_b} \sum_{\alpha=1}^{N_d} \mathbf{e}_{\bar{\alpha}} [f_{\alpha}(\mathbf{x}_b, t) + f_{\bar{\alpha}}(\mathbf{x}_b + \mathbf{e}_{\bar{\alpha}}\delta t, t)] \quad (49)$$

where $\mathbf{e}_{\bar{\alpha}}$ is the lattice direction opposite of \mathbf{e}_{α} .

One disadvantage of the momentum response as shown in Equation 49 is that it makes use of values of f_{α} from neighboring lattice points. This non-locality can complicate parallel implementation. For problems with a large number of lattice points on fluid/solid boundaries, the need to access additional values of f_{α} can add to the overall memory bandwidth demand and thus degrade performance for this memory bandwidth-bound application.

C. COUPLING PROCEDURE

Once the relevant forces have been computed on the fluid domain, they must be satisfactorily transferred to the discrete representation of the structural domain on which they will be imparted. Respectively, once the equations of motion have been solved on the structural domain, the inputs relevant to the coupled fluid problem must be passed to the fluid domain. This straight-forward problem can become complicated due to the possibility that the discrete representation of the fluid and solid may not conform exactly at the interface. In cases where the meshes do not conform, some form of interpolation will be required in order to map forces applied in one domain to degrees of freedom in the other.

For this work, problems were restricted to those where the fluid and structural discretizations would conform at domain boundaries. This approach greatly simplifies communication of information between domains at the cost of severely restricting the types of problems that can be analyzed. Specifically, the geometric non-linearity of a moving solid mesh covering and uncovering fluid lattice points is not addressed within the scope of the

present work; data-flow between the meshes will be addressed as in Equation 50.

$$\begin{aligned} p_{\text{fluid}}(\mathbf{x}, t) &\rightarrow p_{\text{solid}}(\mathbf{x}, t) \\ \mathbf{u}_{\text{solid}}(\mathbf{x}, t) &\rightarrow \mathbf{u}_{\text{fluid}}(\mathbf{x}, t) \end{aligned} \tag{50}$$

Once the data has been transferred between the fluid and solid domain meshes, procedures appropriate for each domain are applied to apply those boundary conditions to the discrete model. Future implementations will address this shortcoming and implement appropriate interpolation and extrapolation schemes for boundary data communication.

D. FLUID-STRUCTURE INTERACTION IN TWO DIMENSIONS

All FSI simulations conducted in two dimensions use the D2Q9 lattice for the LBM solution to the fluid domain. For all structural components modeled within the two-dimensional FSI problem, Euler-Bernoulli beam elements with linear elastic constitutive models are used for the discrete structural model.

1. Structural Model

A formulation of the Euler-Bernoulli beam type is presented in [73]; a schematic is given in Figure 46. There are two degrees of freedom per node; displacement v and rotation θ . The beam materials to be used are listed in Table 6.



Figure 46: Euler-Bernoulli Beam.

Material	$\rho \left(\frac{\text{kg}}{\text{m}^3} \right)$	$E \left(\frac{\text{kg}}{\text{m}^2} \right) \times 10^6$
steel	7,800	210,000
cork	180	32
PVC	1,400	1,500

Table 6: Selected structural material properties used for FSI simulations.

Fluid	$\rho \left(\frac{\text{kg}}{\text{m}^3} \right)$	$\nu \left(\frac{\text{m}^2}{\text{sec}} \right) \times 10^{-6}$
ethyl alcohol	790	1.4
vegetable oil	920	76.1
water	1000	1.14
blood	1035	4
glycerin	1260	1127
Mercury	13594	0.0114

Table 7: Selected fluid properties for FSI simulations.

2. Fluid Models

The FSI simulations performed for this work were repeated for a selected combination of fluid and structural properties. The goal is to obtain insight as to how the combined systems would behave with various combinations of either highly viscous and dense fluids like honey as compared to fluids of very low viscosity such as liquid Mercury. Though this leads to an admittedly qualitative analysis, this author asserts that the results can still be useful for building intuition and confirming the overall efficacy of the software tools. The relevant properties of the fluids used in these simulations are summarized in Table 7.

3. Converging-Diverging Channel

This problem, inspired by similar work reported in [74], is a 2D FSI problem of flow in a converging and diverging duct. A schematic of the problem domain is shown in Figure 47. No-slip boundary conditions are used on the rigid portions of the upper and lower boundary. In the LBM problem, the structure is modeled as a moving solid domain and in the FEM structural dynamics problem it is modeled as a Euler-Bernoulli beam with clamped boundary conditions on both ends.

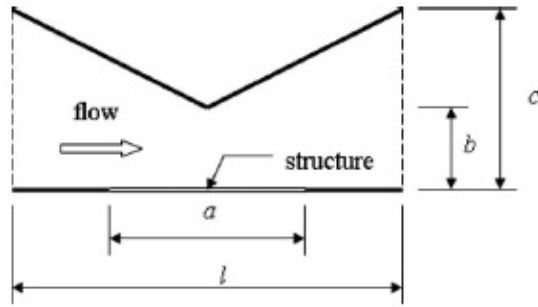


Figure 47: Schematic of 2D converging and diverging duct.

A series of simulations were run with glycerin as the baseline fluid; chosen for its comparative high density and viscosity. The flexible structure is composed of cork; chosen for its comparative low density and low modulus of elasticity. The flow Reynolds number is set at 5 based on inlet width. Results for displacement, velocity and acceleration at the beam midpoint are given in Figure 48 for the first 72 seconds of simulation time. Note that no damping was included in the material model, but that nonetheless the beam motion is gradually damped to a constant downward displacement as expected. The relative phases of displacement, velocity and acceleration are displayed in Figure 49.

It is possible to gain intuitive insight into the important FSI parameters even with this comparatively crude implementation. Consider the case where the viscosity of the fluid is changed. In Figure 50, a comparison can be made for beam displacement where the fluid viscosity is varied. It is clear that fluid viscosity is an important parameter in ultimate damping of beam oscillations where more viscous liquids offer more resistance to structural velocities. We do a similar exercise with beam elasticity by varying the elastic modulus. Results for this are given in Figure 51. The more pliant material is damped by the fluid more quickly than the relatively stiff beam.

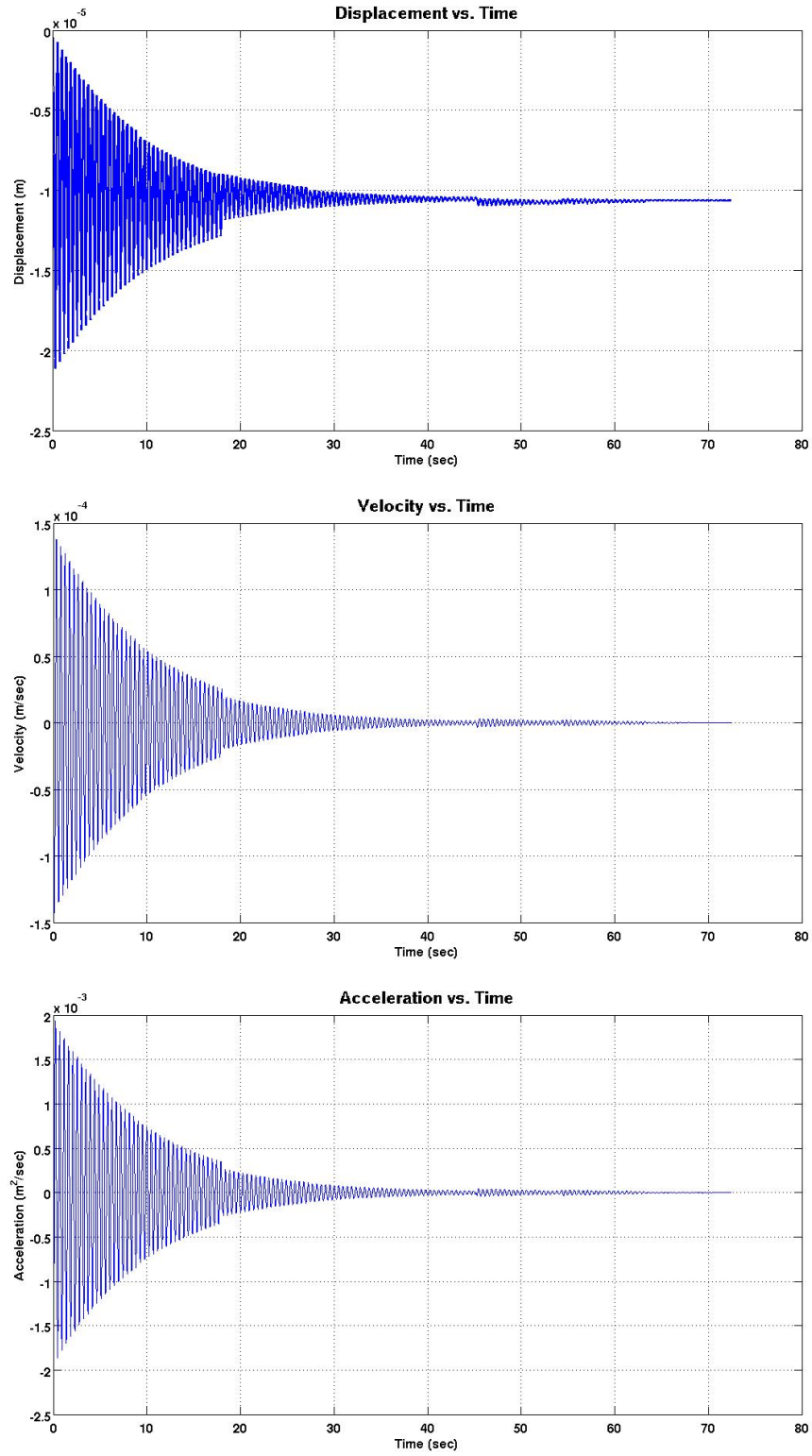


Figure 48: Converging and diverging duct displacement, velocity and acceleration at beam midpoint. $Re = 5$, glycerin with cork beam.

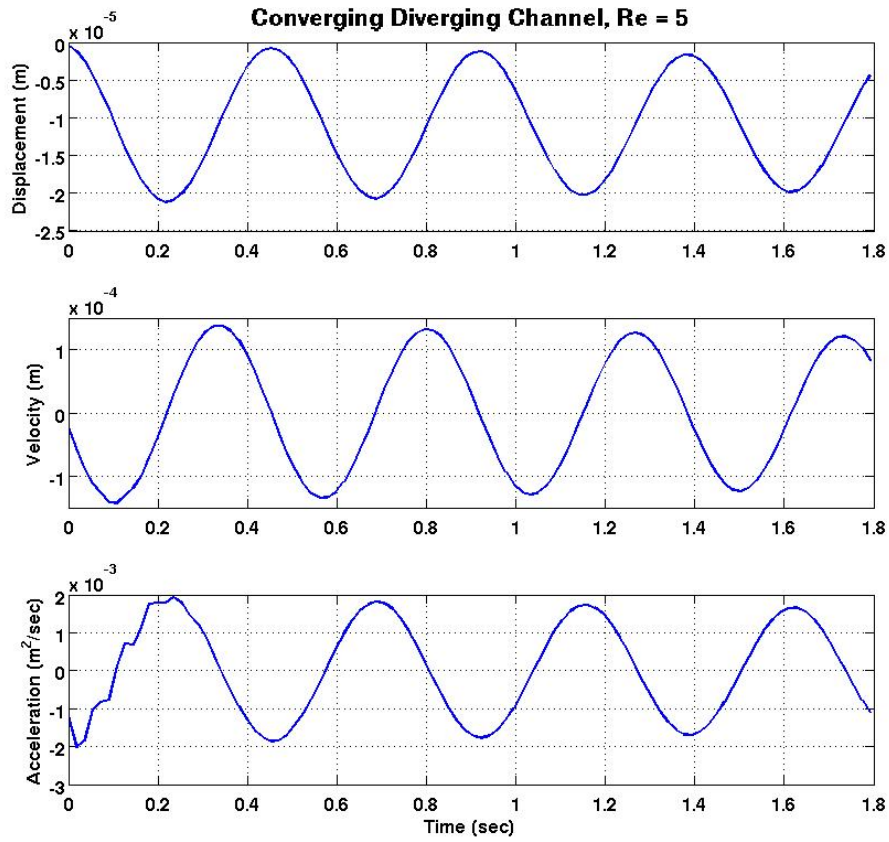


Figure 49: Converging and diverging duct with combined beam response. $\text{Re}=5$, glycerin with cork beam.

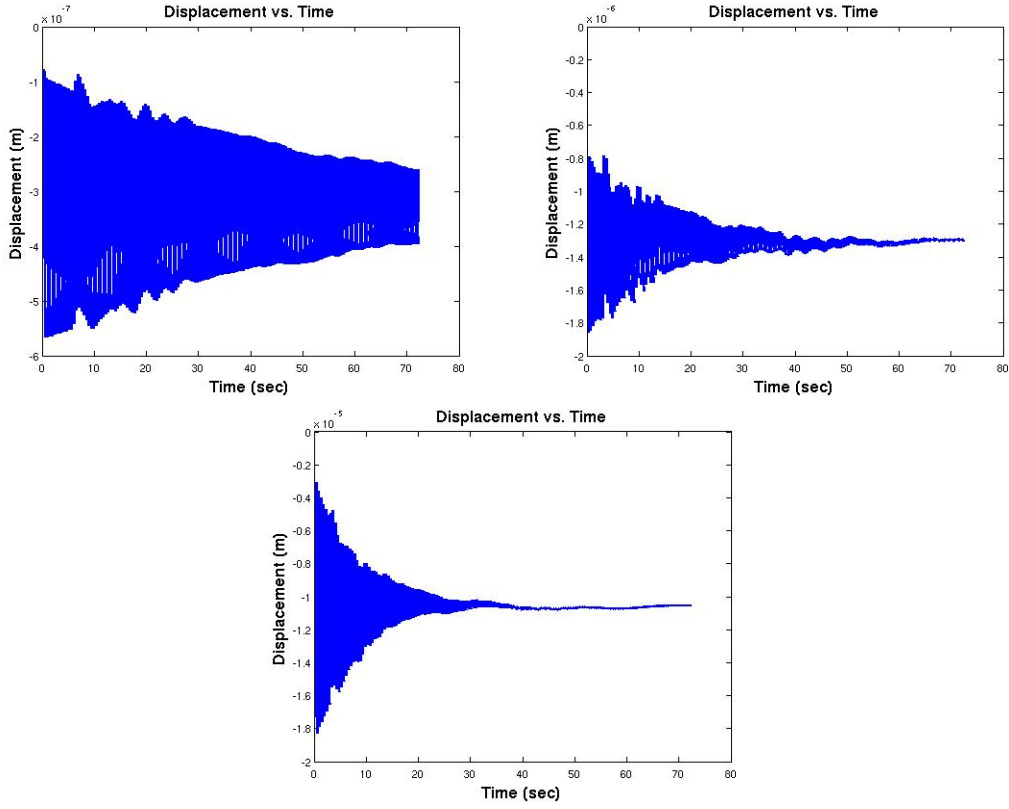


Figure 50: Converging and diverging duct with varying fluid viscosity. Starting from top left, fluid viscosity is $\frac{\nu_{\text{glycerin}}}{4}$, $\frac{\nu_{\text{glycerin}}}{2}$ and ν_{glycerin}

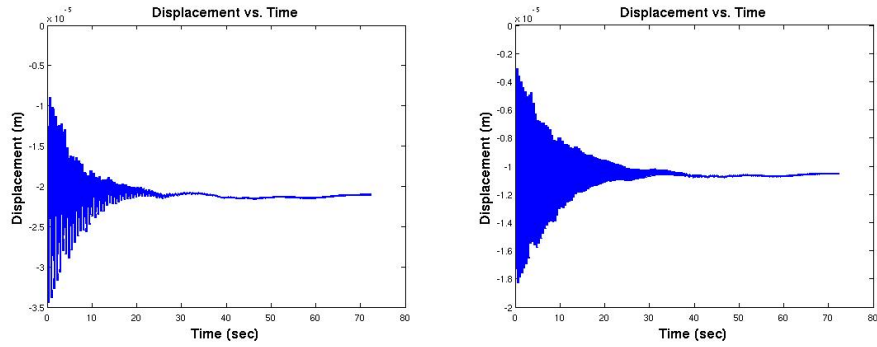


Figure 51: Converging and diverging duct with varying beam elastic modulus. From left to right elastic modulus is $\frac{E_{\text{cork}}}{2}$ and E_{cork} .

4. Lid-Driven Cavity

The lid-driven cavity FSI simulation uses the geometry illustrated schematically in Figure 52. The top wall will be modeled using the Regularized boundary condition for imposed velocity, the bottom wall will be modeled as an elastic moving boundary and the left and right walls will be modeled as no-slip boundaries. The elastic bottom wall will use the Euler-Bernoulli beam with clamped boundary conditions on both ends.

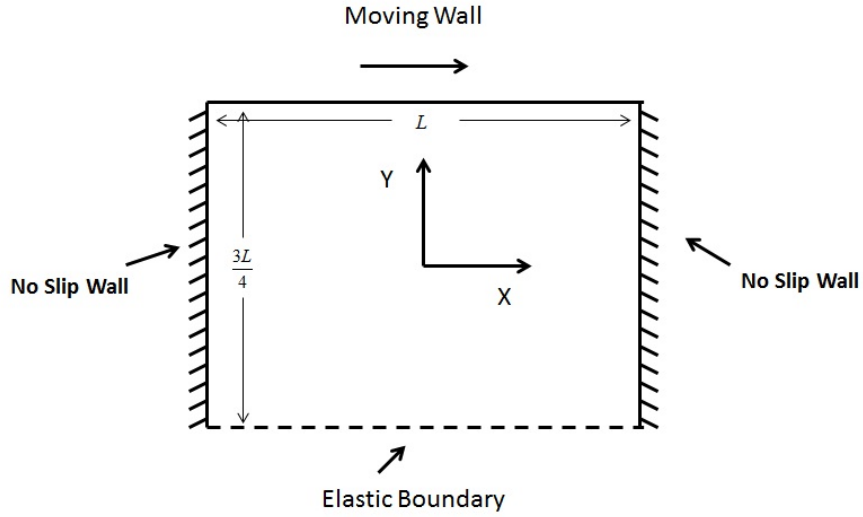


Figure 52: Schematic diagram of lid-driven cavity FSI problem geometry.

The results for the simulation are presented in Figure 53. The streamlines are shown as well as a vector representation of final displacement. A plot of the final elastic boundary displacement is provided in Figure 54. The fluid for the simulation was glycerin and the material used for the elastic boundary was PVC with material properties as listed in Table 6. In this instance, Rayleigh damping was applied to the material model to limit spurious oscillatory behavior of the structure. This damping was applied by selecting parameters α and β in Equation 51 where for this equation \mathbf{M} is the structural mass matrix and \mathbf{K} is the structural stiffness matrix. These parameters are set so as to generate a damping matrix \mathbf{C} that generates acceptable beam dynamic behavior.

$$\mathbf{C} = \alpha \mathbf{M} + \beta \mathbf{K} \quad (51)$$

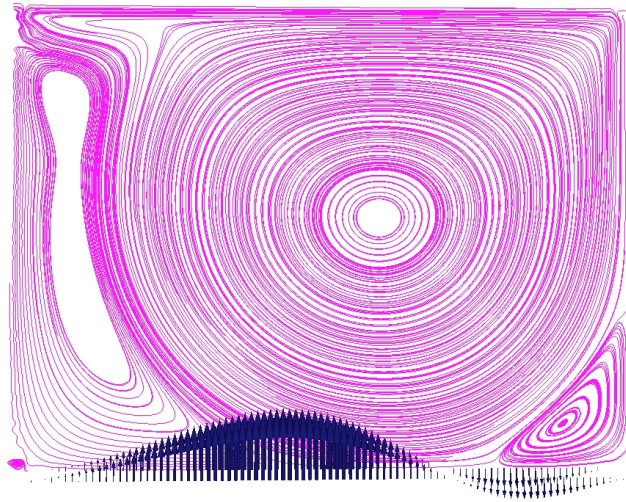


Figure 53: Results for two-dimensional lid-driven cavity.

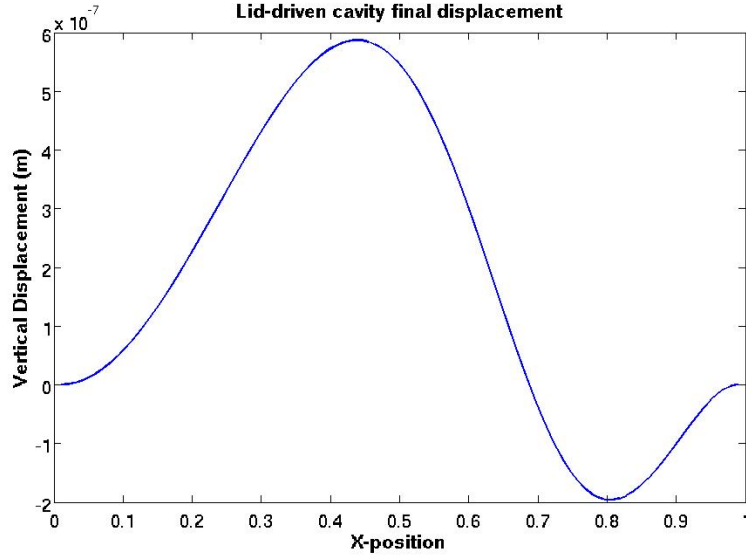


Figure 54: Final bottom displacement.

5. Cylinder with Fin Benchmark

For this example simulation, the two-dimensional variation of the cylinder with elastic fin benchmark proposed in [75]. The inlet boundary condition is a parabolic velocity profile, the outlet is modeled as a constant pressure boundary condition. The top and bottom of the domain is modeled as no-slip boundaries. The flow Reynolds number, based on cylinder diameter, is set to 200. In this flow condition, periodic vortex shedding is expected from the top and bottom of the cylinder.



Figure 55: Cylinder with elastic fin benchmark

The resulting pressure fluctuations from the vortex shedding imposes a periodic excitation on the elastic fin. The elastic fin is modeled as an Euler-Bernoulli beam. The displacement, velocity and acceleration at the beam tip is presented in Figure 56.

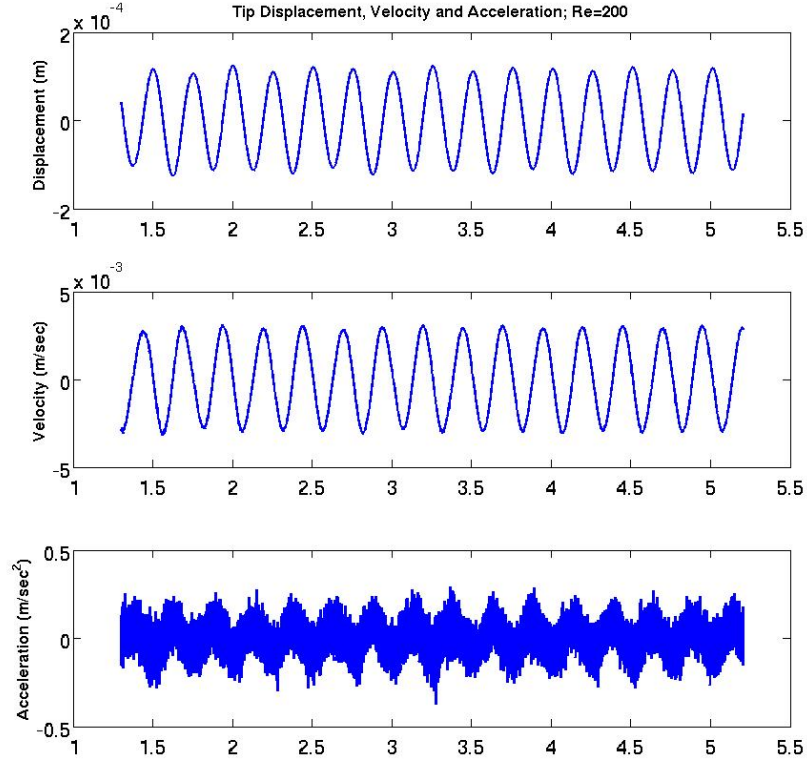


Figure 56: Results for two-dimensional cylinder with elastic trailing fin at $Re=200$.

E. FLUID-STRUCTURE INTERACTION IN THREE DIMENSIONS

In this section, the cylinder with elastic fin benchmark presented previously is repeated in three dimensions. The fluid is represented using a D3Q19 lattice along with a MRT collision operator; both choices made in the interest of maximizing fluid simulation stability while minimizing the required number of lattice points. The structural model is composed of a single Mindlin-Reissner plate. A detailed formulation of this plate is presented in [73].

The inlet boundary condition is a parabolic velocity profile and the outlet boundary condition is constant pressure. No-slip boundaries are established on the upper and lower boundaries of the domain as well as on the surface of the rigid cylinder. The inlet velocity is modeled with regularized boundary conditions as is the constant pressure outlet. The elastic fin is modeled with clamped boundary conditions at the attachment point to the cylinder with free boundary conditions on the free end. The surface of the elastic fin is represented in the fluid domain as a moving boundary.

In order to ensure representative results, an initialization phase is performed where the LBM system is iterated until the expected time-periodic flow condition is established. This condition is confirmed by sampling the vertical velocity component in the channel center-line downstream of the cylinder/fin obstacle; a stable periodic oscillation indicates the system is ready to initiate FSI.

Results are shown in Figure 57. The oscillation frequency of the beam tip is 3.8 sec^{-1} . For the geometry and fluid properties used in this simulation this corresponds to a Strouhal number of 0.19 which matches well with experimentally measured values for vortex shedding for flow of a cylinder with Reynolds number equal to 200.

F. HETEROGENEOUS PARALLEL IMPLEMENTATION

The computational requirements for three-dimensional two-way FSI is significant with both the structural and fluid models requiring a large amount of memory and processor resources. The GPU used for this research had sufficient memory resources to handle

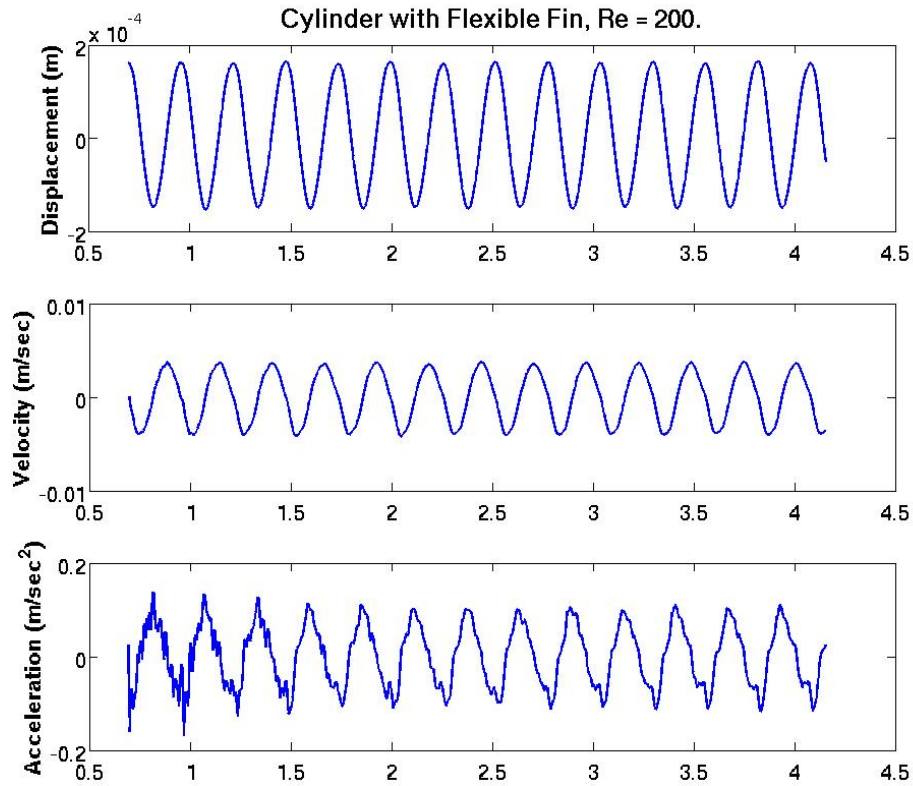


Figure 57: Displacement, velocity and acceleration for cylinder with elastic fin. Re=200.

only one of these problems. Therefore all of the FSI examples presented in this work use the strategy of employing the GPU for the LBM simulation while relying on the CPU for the structural dynamics simulation. The rationale for this choice is that in each case the structural model is dimensionally reduced relative to the fluid model; two-dimensional fluid models interact with Euler-Bernoulli beam structural models that are logically one-dimensional. Similarly, for the three-dimensional FSI example, the three-dimensional fluid model is coupled with a structural model that uses a plate that is logically two-dimensional. With the GPU being the most capable computational device, it was assigned to the largest portion of the work. The task-level decomposition for the FSI simulation between the GPU and CPU is illustrated in Figure 58.

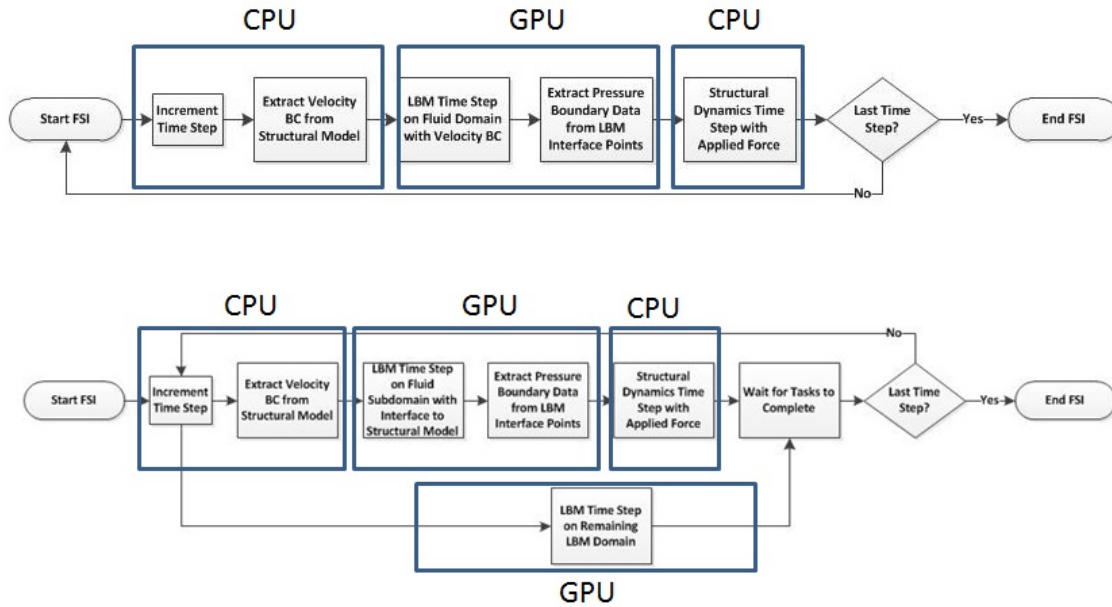


Figure 58: Illustration of task-level decomposition in parallel implementation of FSI problem. In the lower figure, a further level of task-level parallelism is exploited by overlapping the structural dynamics computation on the CPU with LBM calculations on domain areas remote from the elastic structure on the GPU.

Two implementations were prepared for this work. In the first case, the fluid domain was considered as a whole with the GPU performing an LBM time step on the entire domain before passing pressure boundary conditions to the CPU for the structural simulation.

When the CPU completed the structural time-step, velocity boundary conditions are passed back to the GPU. In the second case, the fluid domain is partitioned as illustrated in Figure 59. With this decomposed domain, the GPU would execute an LBM time step in a region of the domain immediately surrounding the elastic structure. When the time step is complete, updated fluid forces are transferred to the CPU memory so that the structural time step can be executed. Concurrently, immediately upon passing its boundary conditions, the GPU commences execution of the LBM time step on the remaining fluid domain. In this way, the overall computation time is reduced by exploiting this extra level of concurrency. The performance improvement that is realized by using this strategy is highly variable; depending both on the problem as well as the relative performance characteristics of the GPU and CPU as well as the implementation details of both the LBM and structural dynamics simulation model. Nonetheless, for this research, using an Intel i5 quad-core CPU running at 3.6 GHz combined with a NVIDIA GTX-580, a performance improvement of 23% was obtained using this procedure as shown in Table 8.

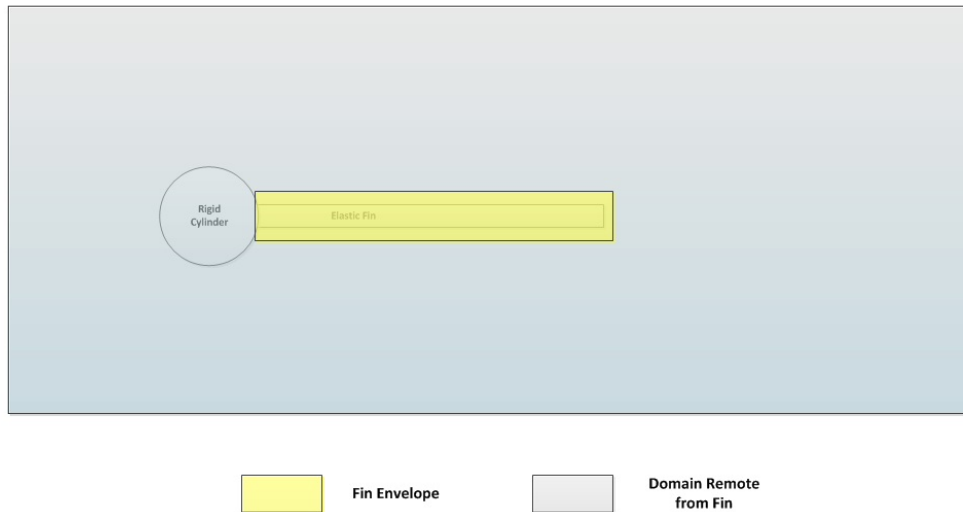


Figure 59: Decomposition of FSI problem domain for task-level heterogeneous parallelism.

Method	Average time per time-step (sec)	Percent Speedup
Non-Overlapped	0.0305	-
Overlapped	0.0234	23%

Table 8: Performance improvement from using overlapped execution depicted in lower half of Figure 58 versus the non-overlapped scheme in the top half of Figure 58. The lattice was $22 \times 337 \times 526$ D3Q19 using MRT collision operator. The structural model was a sheer-deformable plate with 2883 degrees of freedom.

VI. HYBRID LATTICE BOLTZMANN METHOD

A. INTRODUCTION AND LITERATURE REVIEW

As a fluid flow solver, the LBM is particularly effective in scenarios where conventional methods like FDM, CVM and FEM have difficulty. Cases with highly complex geometry such as are encountered in porous flow problems [76] where it is difficult or impractical to fully discretize the domain are particularly suitable to LBM. Simulations involving multi-component or multi-phase flows where it is very hard to accurately model fluid interfaces and to capture fluid phase and component interactions are also examples where LBM has found good use [77]-[79].

Despite these advantages, the LBM in its classical formulation (CLBM) has challenges of its own. In order to describe the transport of particle velocity distributions through the domain, the CLBM calls for a coupled space and time domain discretization that is realized in the form of a uniform and regular set of lattice points across which particles “stream.” For practical problems which often contain objects with curved or complex surfaces it may be necessary to use a highly refined lattice to describe the geometry. This often leads to non-complex regions of the domain populated with a needlessly dense lattice.

Several methods have been developed to alleviate this issue and provide greater geometric flexibility and adaptability to the lattice mesh. These approaches include development of a finite volume formulation of the LBM [80] as well as finite difference formulations [81], [82], multigrid lattice methods [83] finite element LBM (FELBM) [84], [74], and spectral element discontinuous Galerkin LBM [85]-[87] among others. These methods obtain this benefit of geometric flexibility at the expense of a relative increase in the computational effort required per lattice point in the problem domain.

In this dissertation, we describe a hybrid LBM (HLBM) where the FELBM derived in [74] is combined with the CLBM over one or more sub-domains. This new method exploits the geometric flexibility of the FELBM to mesh complex surfaces with fewer lattice

points than the CLBM while leveraging the CLBM to model geometrically simple regions of the problem domain with greater computational efficiency. The result is a method that benefits from both approaches.

In the following section, the derivation of FELBM is outlined. Next, the coupling procedure of the HLBM is illustrated followed by numerical results and conclusions.

B. FINITE ELEMENT LBM

The FELBM borrows almost everything from the CLBM theory. The formulation and implementation can be summarized as very similar to CLBM with the exception of the “streaming” procedure at the end of each time step which the FELBM does not do. Instead, an equivalent operator is developed to “advect” the particle density distribution functions along each of the characteristic lattice directions. This feature is what allows the FELBM to use a non-uniform grid and the interpolative nature of the advection operator is common among non-classical LBM procedures.

Starting with the discrete Boltzmann equation, we expand f_α within a space of interpolating polynomials defined on finite elements:

$$f_\alpha = \sum_{i=1}^n H^i f_\alpha^i = [H]\{f_\alpha\} \quad (52)$$

where n is the number of nodes in an element as well as the number of interpolating polynomials H^i .

This relation is substituted into Equation 8 using the BGK collision operator of Equation 9 and the result is re-expressed in residual form:

$$R = [H] \frac{\partial f_\alpha}{\partial t} + \mathbf{e}_\alpha \cdot [\nabla H] \{f_\alpha\} + \frac{1}{\tau} [H] \left(\{f_\alpha\} - \{\tilde{f}_\alpha\} \right). \quad (53)$$

Using the Galerkin formulation of the Method of Weighted Residuals, the given residual is multiplied by the interpolating functions H^i and integrated over all elemental domains. This results in the following set of linear equations:

$$[M] \frac{\partial \{F_\alpha\}}{\partial t} + [K] \{F_\alpha\} + [C] \{F_\alpha\} - [C] \{\tilde{F}_\alpha\} = 0 \quad (54)$$

where, with Ω_e being the elemental domain for the e -th finite element, the linear operators are defined as:

$$[M] = \sum_e \int_{\Omega_e} [H]^T [H] d\Omega \quad (55)$$

$$[K] = \sum_e \int_{\Omega_e} [H]^T (\mathbf{e}_\alpha \cdot [\nabla H]) d\Omega \quad (56)$$

$$[C] = \sum_e \int_{\Omega_e} \frac{1}{\tau} [H]^T [H] d\Omega \quad (57)$$

$$\{F_\alpha\} = \sum_e \{f_\alpha^e\}. \quad (58)$$

This is now a first-order differential equation in time which describes the advection of particle distribution functions along the characteristic lattice directions.

Herein lies the difficulty of the FELBM. While the CLBM is able to accomplish the particle “advection” by streaming between neighboring lattice points which can be effected by simple copy and assignment operations, the FELBM must accomplish the same task by evaluating this discrete linear advection equation. Whatever time integration method is used, it is obvious that it will always be more demanding than the CLBM streaming and, unlike the logical streaming method, is subject to the usual dissipative and dispersive approximation errors associated with the numerical time-integration method employed.

Numerical dissipation and dispersion can be mitigated by reducing time-step size and refining the spatial mesh, but both of those methods require more computational work. In a similar way, dispersive errors can be mitigated by using higher-level time integration

schemes such as explicit multi-stage Runge Kutta methods, or implicit methods such as Backward Euler, Trapezoidal or Crank-Nicolson techniques but these methods also require additional work.

The hybrid method introduced in the next section seeks to reduce the additional computational workload associated by employing the FELBM over only those sub-domains where the geometric flexibility is needed. The remainder of the domain is modeled with CLBM and a coupling procedure is introduced to allow the solution to proceed concurrently on all sub-domains.

C. HYBRID CLBM/FELBM METHODOLOGY

In order to mitigate the computational demands of the FELBM while retaining the ability to model a domain with complex and irregular shapes without an unnecessarily dense lattice, the hybrid CLBM/FELBM (HLBM) methodology is developed.

All of the theoretical machinery from the CLBM and FELBM formulations are preserved and the logical sequence of computations is maintained on each individual sub-domain. A typical HLBM time-step is portrayed schematically in Figure 60.

To couple disjoint sub-domains, an interface layer is provided. Computationally, the streaming process of the CLBM domain and the advection process of the FELBM domain can be executed concurrently with each sub-domain retaining a “halo” of depth 1 into the adjoining sub-domain. Within each sub-domain, the outermost layer of lattice points represents the halo and as shown in Figure 61 and Figure 62.

While this coupling scheme is conceptually very simple, great care must be taken with the time and space integration methods used for advecting particle density data on the FELBM sub-domain. First-order time integration schemes tend to have too much dissipation error while second order schemes suffer from dispersion errors; both of which propagate onto the CLBM sub-domain and impacts solution quality and stability everywhere. For the results discussed in this paper, simple bi-linear elements are used for the spatial discretization and a 4-stage 3rd order explicit time integration method shown in Equation

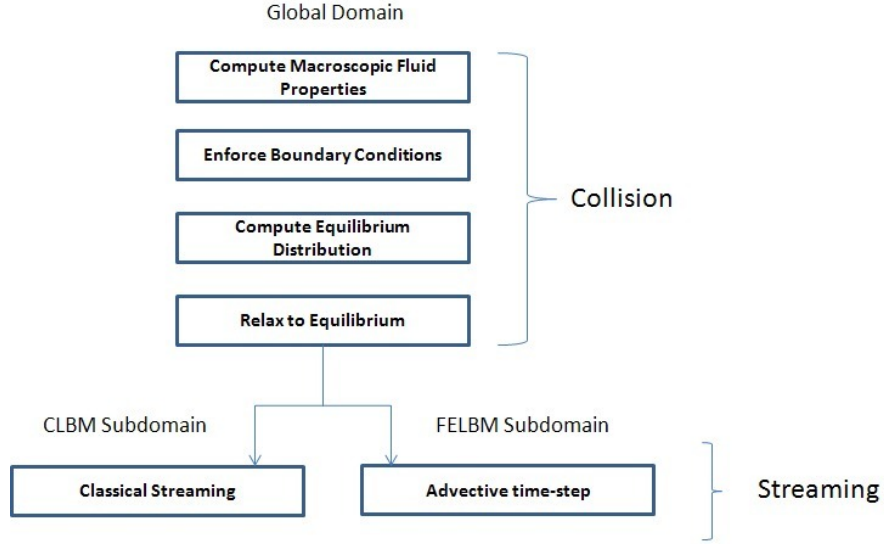


Figure 60: Schematic of Hybrid LBM time step. Methodology differs only in implementation of the particle streaming phase.

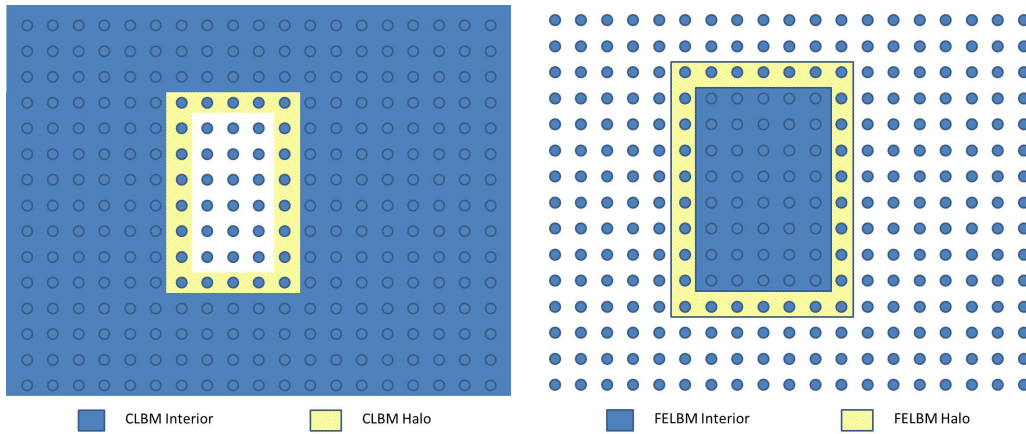


Figure 61: Schematic Hybrid Lattice on regular domain. Assignment following streaming in the CLBM domain and advection in the FELBM domain is only made to the interior of each respective sub-domain. Data drawn from the lattice points on the halo facilitates communication between each sub-domain.

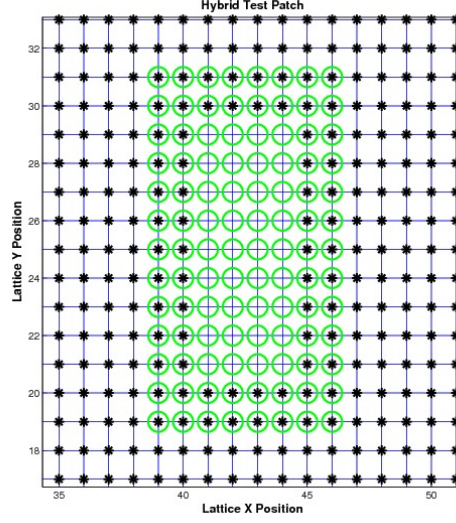


Figure 62: Interface region for CLBM and FELBM domains on a uniform mesh. Lattice points with both the asterisk and circle belong to the interface.

59 is used for temporal integration. This method effectively controls both dissipation and dispersion errors during the advection process and allows a single FELBM advection time step for every CLBM streaming step. The CLBM sub-domain undergoes the classical LBM streaming to adjacent neighbors restricted to only destination lattice points that lay within the CLBM interior as indicated in Equation 60.

$$\begin{aligned}
 F(U) &= \text{FEM advection operator on FELBM sub-domain elements} \\
 U^n &\leftarrow \text{fOut}^n|_{\text{FELBM sub-domain}} \\
 U^{(1)} &= U^n + \frac{1}{2}\Delta t F(U^n), \\
 U^{(2)} &= U^{(1)} + \frac{1}{2}\Delta t F(U^{(1)}), \\
 U^{(3)} &= \frac{2}{3}U^n + \frac{1}{3}U^{(2)} + \frac{1}{6}\Delta t F(U^{(2)}), \\
 U^{n+1} &= U^{(3)} + \frac{1}{2}\Delta t F(U^{(3)}), \\
 U^{n+1} &\rightarrow \text{fIn}^{n+1}|_{\text{FELBM interior}}
 \end{aligned} \tag{59}$$

$$\text{fOut}^n|_{\text{CLBM sub-domain}} \xrightarrow{\text{streaming}} \text{fIn}^{n+1}|_{\text{CLBM interior}} \quad (60)$$

Geometrically simple portions of the domain are discretized with a uniform, regular lattice for the CLBM. Sub-domains containing complex or irregular shapes are identified and discretized with the FELBM. For example, in simulations such as those requiring fluid-structure interaction, in the case of flow past a heat exchanger tube bundle, it would suffice to employ the FELBM only in a region around the actual tubes. This area could employ a mesh with isoparametric elements to efficiently describe the shape of the tube and be used with the FELBM, while the remainder of the domain could use a uniform, regular lattice and the CLBM. The resulting HLBM could accurately capture the flow properties while reducing the total number of lattice points required significantly.

D. NUMERICAL RESULTS AND DISCUSSION

In all numerical examples provided, four-node linear isoparametric elements are used for FELBM analysis as well as in the FELBM sub-domains of a hybrid method. For CLBM analysis and in the associated sub-domains of hybrid models, the D2Q9 lattice is used with the single relaxation time BGK collision operator. The linear advection equation on the FELBM domain is solved using a four-stage third order Strong Stability Preserving Runge-Kutta method. This more robust method was essential to minimize the impact of diffusive errors arising from the advection operator implemented with bi-linear finite element methods. Numerous alternative integration schemes are possible however if advective sub-steps are allowed on the FELBM sub-domain.

As the first example, a simple Poiseuille flow problem is simulated using the HLBM with a simple 20x50 lattice-point FELBM patch embedded in a 200x50 lattice point CLBM domain. The goal of this test is to prove the effectiveness of the coupling procedure. The simulation in all cases show good agreement with the well-known exact solution as shown in Figure 63.

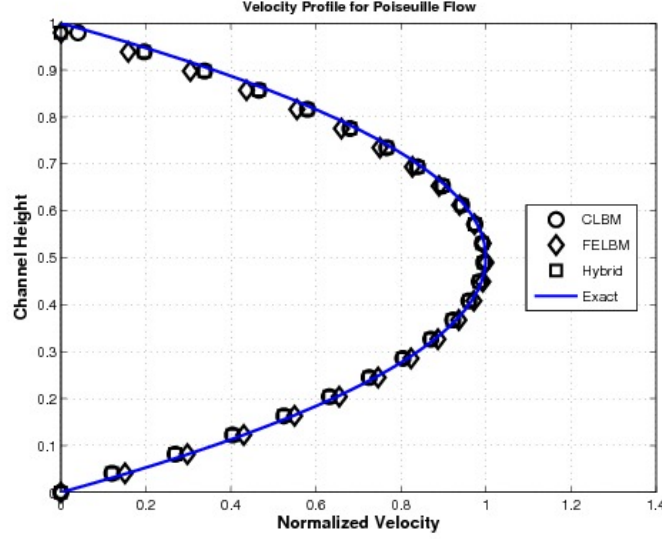


Figure 63: Mid-channel normalized velocity profile for Poiseuille flow using CLBM, FELBM and HLBM.

The next numerical test is channel flow with a circular obstacle. The obstacle size and boundary conditions are selected such that a flow condition corresponding to Reynolds number of 5 is achieved. The CLBM, FELBM and HLBM methods are employed to simulate the fluid flow, but a regular, uniform lattice is maintained in all cases. The obstruction is placed at $\frac{L}{5}$ where L is the length of the channel.

The last numerical test employs a mixed mesh around the same circular obstacle. A schematic of the mesh used in the vicinity of the obstacle is shown in Figure 64. As indicated by the contour plots of both the CLBM and HLBM simulations, both schemes give results that are in good agreement throughout the computational domain.

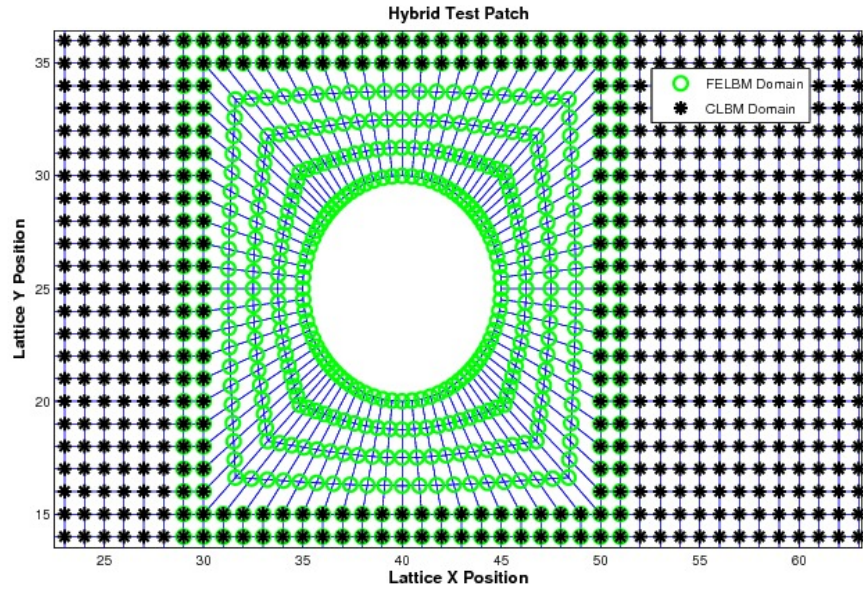


Figure 64: Hybrid lattice mesh around a circular obstacle. Lattice points with asterisk are in the CLBM sub-domain, those circled are in the FELBM sub-domain. Those with both markings are members of the interface halo of the two regions.

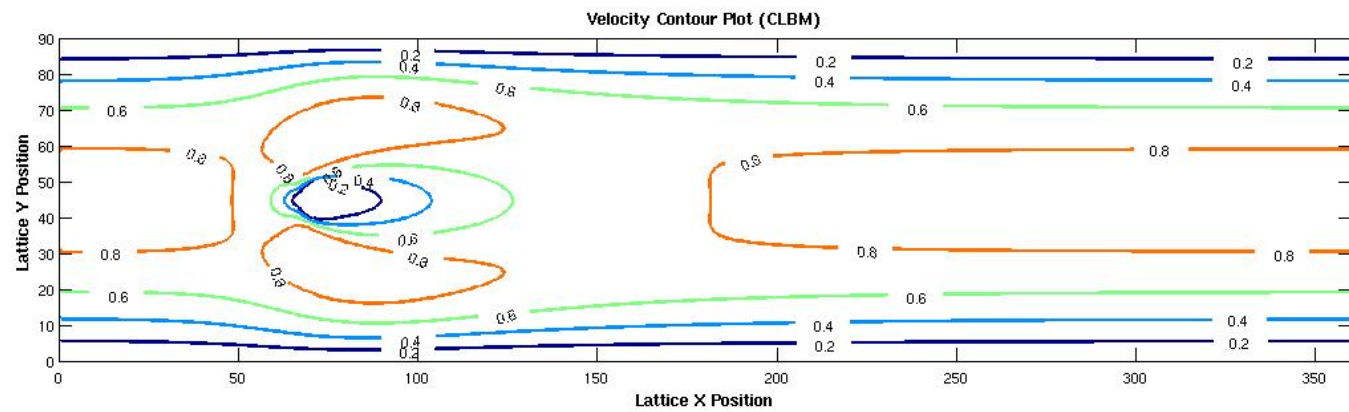


Figure 65: Normalized velocity contour plot for fluid flow around circular obstacle at Reynolds number = 5 using CLBM

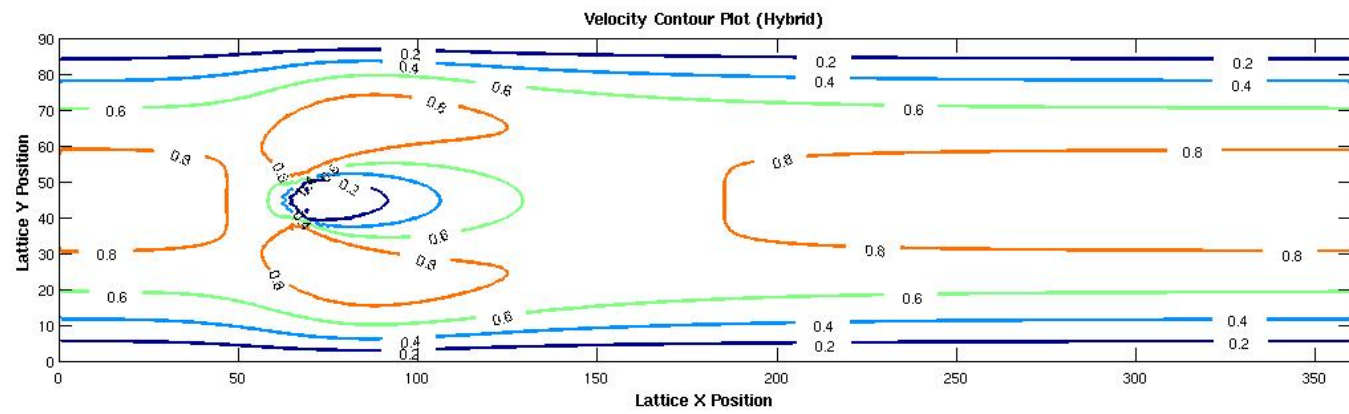


Figure 66: Normalized velocity contour plot for fluid flow around circular obstacle at Reynolds number = 5 using Hybrid LBM.

Method	Relative Execution time per Lattice Point
CLBM	1.0
FELBM	7.9

Table 9: Performance comparison of CLBM and FELBM.

Additionally, the velocity profile is compared for all three methods at different channel positions. The performance of each method is implementation dependent, but for the

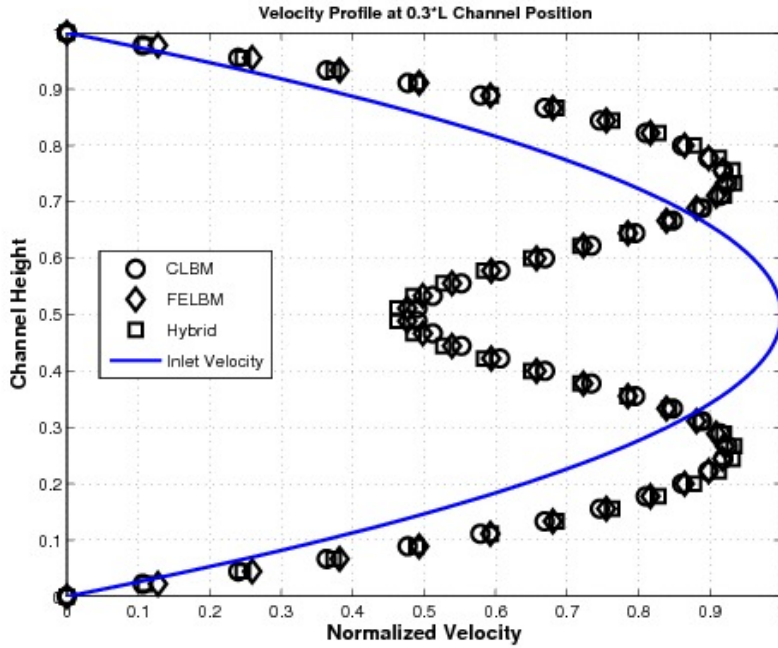


Figure 67: Normalized velocity profile at 30 percent channel length, Reynolds number = 5.

numerical studies done in support of this research, performance results are listed in Table 9.

Roughly speaking, the performance of CLBM and FELBM are independent of problem size. Consequently a simulation employing HLBM is expected in general to exhibit performance characteristics intermediate between CLBM and FELBM; problems with relatively small FELBM sub-domains will result in execution times correspondingly closer to that of CLBM while the opposite is true for larger FELBM sub-domains.

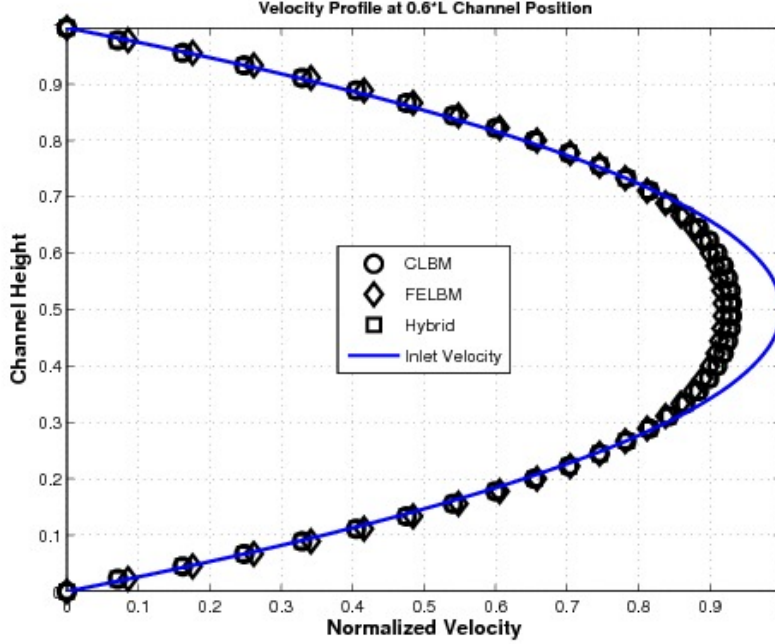


Figure 68: Normalized velocity profile at 60 percent channel length, Reynolds number = 5.

Problems of practical interest introduce non-trivial complexities into this performance analysis. Applications using HLBM as an alternative to CLBM are expected to utilize significantly fewer lattice points and thus require significantly less time. In addition to reducing required run-time for a given simulation, this feature will allow for a more detailed simulations to be conducted on a workstation-size computer.

As an illustration of the potential benefit for curved or irregular boundaries, consider the discretization of the surface of the circular obstruction considered in this dissertation in Figure 69. The HLBM code used for this analysis required 10,210 lattice points for both sub-domains. Comparably realistic depiction of the curved boundary requires significantly more lattice points in a uniform, regular lattice over the entire domain.

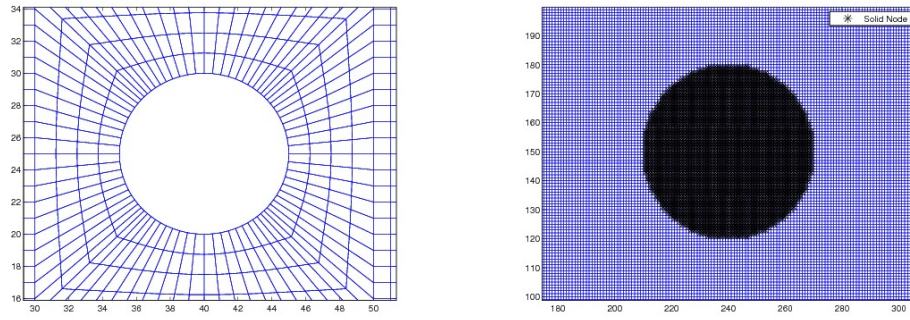


Figure 69: Schematic Hybrid Lattice on regular domain. Assignment following streaming in the CLBM domain and advection in the FELBM domain is only made to the interior of each respective sub-domain. Data drawn from the lattice points on the halo facilitates communication between each sub-domain.

VII. LBM FOR MULTI-COMPONENT FLUIDS

The results and associated discussion presented thus far in this work have focused solely on single-phase, single-component fluid models. One of the strengths of LBM lies in its natural amenability to multicomponent fluids. In this chapter, the main features of the leading multi-component LBM fluid models will be outlined and example applications will be presented for two-dimensional single-phase multi-component flows.

A. MULTI-COMPONENT FLUID MODELS

There are four main multi-component fluid models in LBM theory. The color-fluid model [88], the inter-particle-potential model [89], the free-energy model [90] and the mean-field theory model [91]. The methods can all be compared based on the way in which the surface tension of the component interface is taken into account in the evolution of the particle distribution functions and how the location of this interface is determined. Excellent surveys of multi-component fluid flows are provided in [14]-[16]. In this work, the inter-particle potential model is used, so this method will be discussed in greater detail; the other methods will only be briefly reviewed.

1. Color-Fluid Model

The color fluid model was introduced with the publication of [88] to allow the simulation of immiscible binary fluids in two dimensions. It is based on the two-component cellular-automata model introduced in [92] and modified for use with LBM. The method is referred to as the color-fluid model due to the convention of referring to the binary fluid mixture in terms of “red” particles and “blue” particles. The LBM is carried out for each fluid species and the surface-tension effect on particle distributions is emulated with an additional perturbation term appended to the collision operator. This term, in combination with a “recoloring” step—a correction based on the local color gradient that forces to shift to a direction leading to other like-colored particles—locally places the interface as well

as implements the surface-tension effect with the momentum of each particle distribution. This method is frequently criticized in the literature for the “artificial” recoloring process ([16], [93]) though, as will be seen, each of the multi-component models have some heuristic elements that can be subjected to the same criticism; the resulting spurious velocities exhibited in the vicinity of fluid interfaces is common. More importantly, the recoloring step is executed based on a costly and time-consuming calculation of local color gradients that requires considerably more information sharing between neighboring particles than for other methods.

2. Free-Energy Model

The free-energy model proposed in [90] takes a different approach. Instead of maintaining density distributions for each phase, a single density function ρ is used along with a density difference $\Delta\rho$ as the simulation parameters. Despite the terminology, which lends one to believe that the method was intended mainly for single-component multi-phase flow, the method was originally introduced to model phase separation in non-ideal one- and two-component fluids. The free-energy model gets its name through the use of the so-called Cahn-Hilliard’s approach for non-equilibrium thermodynamics [94]. In this approach, the form of the pressure tensor is defined based on a non-local pressure and a parametrized van der Waals equation of state. This pressure tensor is added to an expanded equilibrium distribution function which produces the desired interfacial effect. This approach has been used to simulate Rayleigh-Taylor instability [95], bubble motion [96] and simulation of spontaneous emulsification of liquid droplets in oil-water-surfactant systems [97].

3. Mean-Field Theory Model

The mean field theory was introduced in [91] for non-ideal gas flow. In this method two distribution functions are used. The first distribution function is used to calculate the pressure and velocity fields of an incompressible liquid. The second is an index function that is used to locate the interface. The model is so-named because the inter-particle interactions are treated using a mean-field approximation in the same way that the Coulomb

interaction among charged particles of a plasma is treated in the Vlasov equation [98], [99]. As several authors have pointed out, this approach is similar to the traditional CFD methods for interface capturing and is the LBM analogy to the level-set [100] and volume of fluid methods [101]. This model has been successfully used to model Rayleigh-Taylor and Kelvin-Helmholtz instabilities [102], [103] with non-ideal dense fluids among other applications.

4. Inter-Particle Potential Model

The inter-particle potential model was proposed in [89] as a simple means to simulate multi-phase and multi-component fluids. The fundamental idea is that the surface tension effects which conventional CFD methods attempt to account for in multi-component flows is microscopic in origin; the same effect could be incorporated into the LBM via these same inter-particle potential forces. In this model, only the nearest neighbor particle densities are considered and they are introduced as follows in Equation 61:

$$\mathbf{F}(\mathbf{x}, t) = -G\psi(\mathbf{x}, t) \sum_{\alpha=1}^{q-1} w_{\alpha} \psi(\mathbf{x} + \mathbf{e}_{\alpha} \Delta t, t) \mathbf{e}_{\alpha}. \quad (61)$$

where \mathbf{x} is particle position, G is a parameter indicating interaction strength, $\psi(\mathbf{x}, t)$ is a function describing the interaction potential, w_{α} is the lattice weight for direction α and \mathbf{e}_{α} is the corresponding lattice velocity. The form of the potential function can be varied to obtain the desired inter-particle potential behavior. For multiphase flow, ψ is commonly expressed as in Equation 62:

$$\psi(\rho) = \psi_0 \exp\left(-\frac{\rho_0}{\rho}\right). \quad (62)$$

where ψ_0 and ρ_0 are arbitrary parameters selected so as to achieve appropriate dynamics for a selected fluid system. The multicomponent fluids systems used in this work are only qualitatively correlated with real fluid systems in that only density and viscosity are set and scaled consistently with the LBM. The parameter G is set so as to generate a desired level of immiscibility while maintaining simulation stability. The potential function is set as

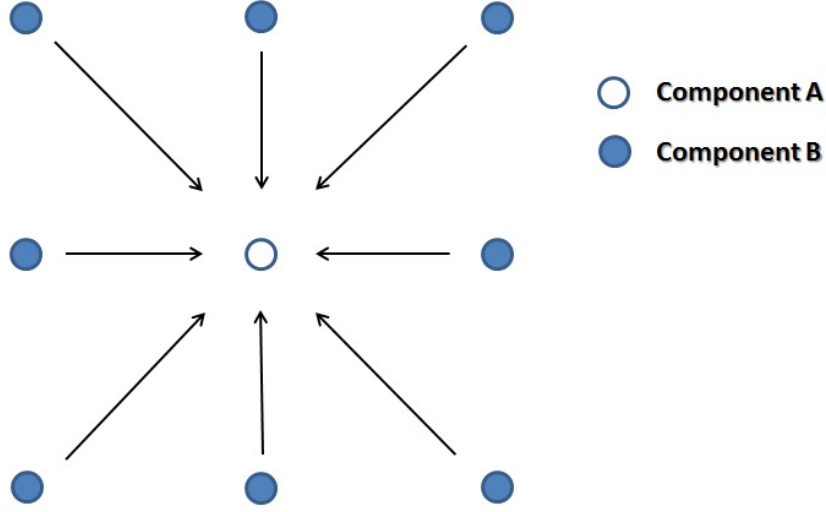


Figure 70: Illustration of inter-particle forces in the nearest neighborhood of a lattice point.

$\psi(\mathbf{x}, t) = \rho(\mathbf{x}, t)$. Notice that Equation 61 specifies a weighted summation of the value of ψ for each lattice position in the neighborhood of a given lattice particle. This is illustrated schematically in Figure 70.

B. IMMISCIBLE MULTI-COMPONENT LBM PROCEDURES

The basic LBM process with multiple components is similar in most ways to that used for single-component systems as illustrated in Figure 10. The obvious difference is that there are now two sets of distribution functions; as before f_α and for a second component that will conventionally be referred to as g_α . Along with the physical domain, both fluids are scaled according to the scaling rules discussed in Chapter II. A second difference is that, as discussed in the preceding paragraphs, the inter-particle force must be calculated in accordance with Equation 61 and incorporated into the calculation of macroscopic velocity used for computing f^{eq} and g^{eq} using Equation 35 and Equation 36. The biggest and most fundamental difference is the need to structure the computations so as to account for

the fact that, due to the desired macroscopic dynamic evolution of the system, some lattice sites will have zero density for one or the other component; only the interfaces will have a significant mixture.

1. Time Stepping

In order to be as explicit as possible, the immiscible multicomponent LBM time-step for fluid lattice points is carried out for this work was implemented as follows:

1. Compute macroscopic density of each fluid:

$$\rho_f = \sum_{\alpha=0}^{q-1} f_{\alpha}$$

$$\rho_g = \sum_{\alpha=0}^{q-1} g_{\alpha}$$

2. Compute macroscopic momentum of each fluid:

$$\rho_f \mathbf{u}_f = \sum_{\alpha=0}^{q-1} \mathbf{e}_{\alpha} f_{\alpha}$$

$$\rho_g \mathbf{u}_g = \sum_{\alpha=0}^{q-1} \mathbf{e}_{\alpha} g_{\alpha}$$

3. Compute a weighted combined macroscopic density and velocity:

$$\rho\omega = \rho_f\omega_f + \rho_g\omega_g$$

$$\mathbf{u} = \frac{\rho_f \mathbf{u}_f \omega_f + \rho_g \mathbf{u}_g \omega_g}{\rho\omega}$$

where we recall $\omega = \frac{1}{\tau}$.

4. Compute inter-particle force using Equation 61 setting G to a constant, and $\psi(\mathbf{x}, t) = \rho$:

$$\mathbf{F}_f = -G\rho_g \sum_{\alpha=1}^{q-1} w_\alpha \rho_g (\mathbf{x} + \mathbf{e}_\alpha \Delta t, t)$$

$$\mathbf{F}_g = -G\rho_f \sum_{\alpha=1}^{q-1} w_\alpha \rho_f (\mathbf{x} + \mathbf{e}_\alpha \Delta t, t)$$

5. Apply these inter-particle forces as momentum inputs to each respective lattice population:

$$\mathbf{u}_f^{eq} = \mathbf{u}_f - \tau_f \mathbf{F}_f$$

$$\mathbf{u}_g^{eq} = \mathbf{u}_g - \tau_g \mathbf{F}_g$$

6. Complete the usual LBGK collision and streaming steps using \mathbf{u}_f^{eq} and \mathbf{u}_g^{eq} and corresponding macroscopic density for computation of f^{eq} and g^{eq} accordingly.

2. Boundary Conditions

For this work, three types of boundary conditions have so far been used: periodic boundaries, bounce-back boundaries and moving boundaries. The bounce-back and periodic boundary conditions for multi-component LBM is the same as for ordinary LBM. Solid nodes bounce-back by swapping the density distribution function across opposite directions as illustrated in Figure 5 in Chapter II. It should be noted that the density distribution values resident on solid nodes do not contribute to the nearest-neighbor force calculation given in Equation 61. The moving boundary condition is employed in the same way as with single-component fluid models using the weighted macroscopic velocity given in step 3 of the above procedure.

C. EXAMPLE APPLICATIONS

In order to get a qualitative feel for how different immiscible multicomponent systems behave using the LBM, some simple cases were implemented for experimentation.

1. Component Separation

This is probably the simplest possible multi-component LBM example. The domain is periodic in both spatial dimensions so there are only periodic boundary conditions. The initial condition is a random distribution between the phases with each lattice point set with a slightly higher or lower proportion of each fluid. The parameter G is set to -1.2 to model strongly repulsive components and the simulation is set to run. The results for selected time steps is presented in Figure 71.

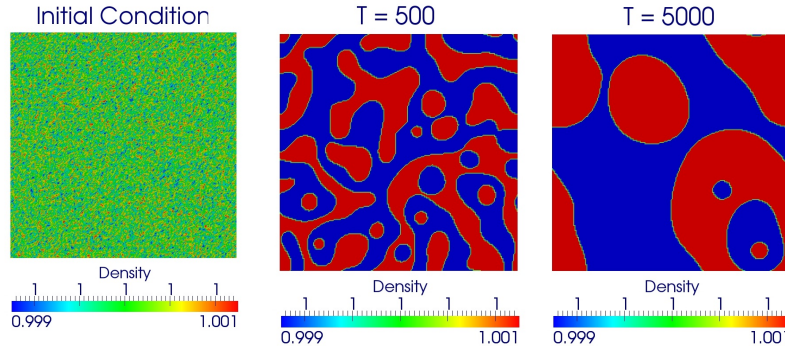


Figure 71: Two immiscible components. $G = -1.2$

This behavior can be compared with less strongly repulsive components by setting the parameter G to -0.2. The results for this simulation are presented in Figure 72. In this case, almost no component separation occurs and the two components as modeled are fully miscible.

2. Lid-Driven Cavity

In order to obtain a multicomponent simulation with recognizable dynamics, the lid-driven cavity problem is used as a model. For this problem two immiscible fluids are initially configured with fluid 1 (corresponding to f density distributions) at the top half

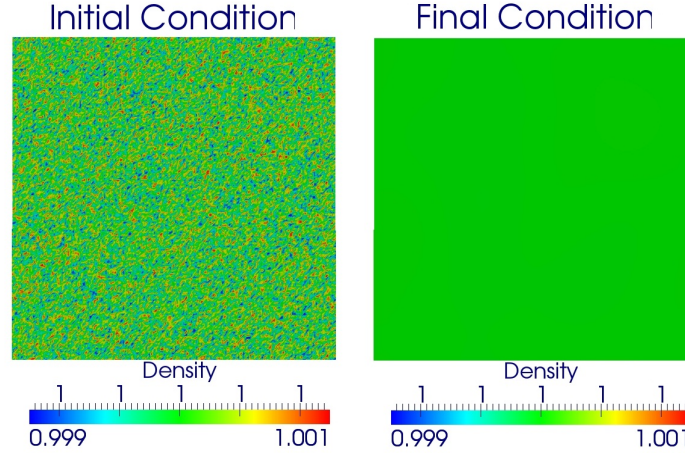


Figure 72: Two immiscible components. $G = -0.2$. Note that the weak interaction parameter renders the fluids miscible.

of the domain and fluid 2 (corresponding to g density distribution functions) at the bottom half of the domain as shown in Figure 73. Two cases will be considered for this problem:

1. Lid-driven cavity with two immiscible fluids of equal density and viscosity.
2. Lid-driven cavity with two immiscible fluids with $\rho_1 = \frac{\rho_2}{2}$ and $\nu_1 = \frac{\nu_2}{4}$. Additionally, a gravitational body force, as described in Chapter II.E, will be added to accentuate the significance of the differing densities.

a. Case 1

As specified above, the fluid density and viscosity are set to be equal; the only difference is the repulsion effect. As the flow develops, the combined forces of the lid, which is driving the flow, and the inter-particle repulsive forces take effect on the particle density distributions. For these strongly repulsive fluids of equal density and viscosity, the result for Fluid 1 is as we would intuitively expect and is shown in Figure 74.

Density for Fluid 1

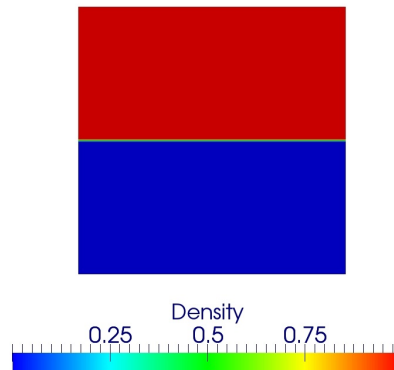


Figure 73: Density for Fluid 1 of a two-component immiscible fluid flow in a lid-driven cavity. Initial configuration.

b. Case 2

Here, the fluid properties are not equal and additionally, there is a gravitational body force applied to both fluids. The system begins in the same initial configuration as shown for Case 1. Time evolution of the density for the two-component system is presented in Figure 75. The momentum evolution for Fluid 1 is presented in Figure 76.

3. Lid-Driven Cavity with FSI

In order to investigate the application of FSI tools to multi-component flow, a simple problem is demonstrated. The problem domain is depicted schematically in Figure 77. A vertical elastic beam is included in a lid-driven cavity. The length of the beam is equal to one-third the cavity depth and it is modeled as an Euler-Bernoulli beam with a clamped boundary where the beam intersects with the bottom of the cavity and free on the other end. Proportional damping was applied to the beam to prevent excessive oscillations that would inhibit a stable fluid simulation. The initial fluid condition is the same as the previous problem, with fluid 1 on the top half and fluid 2 on the bottom half. The lid is set to a constant speed so as to generate a flow field corresponding to $Re=1000$ based on the cavity width.

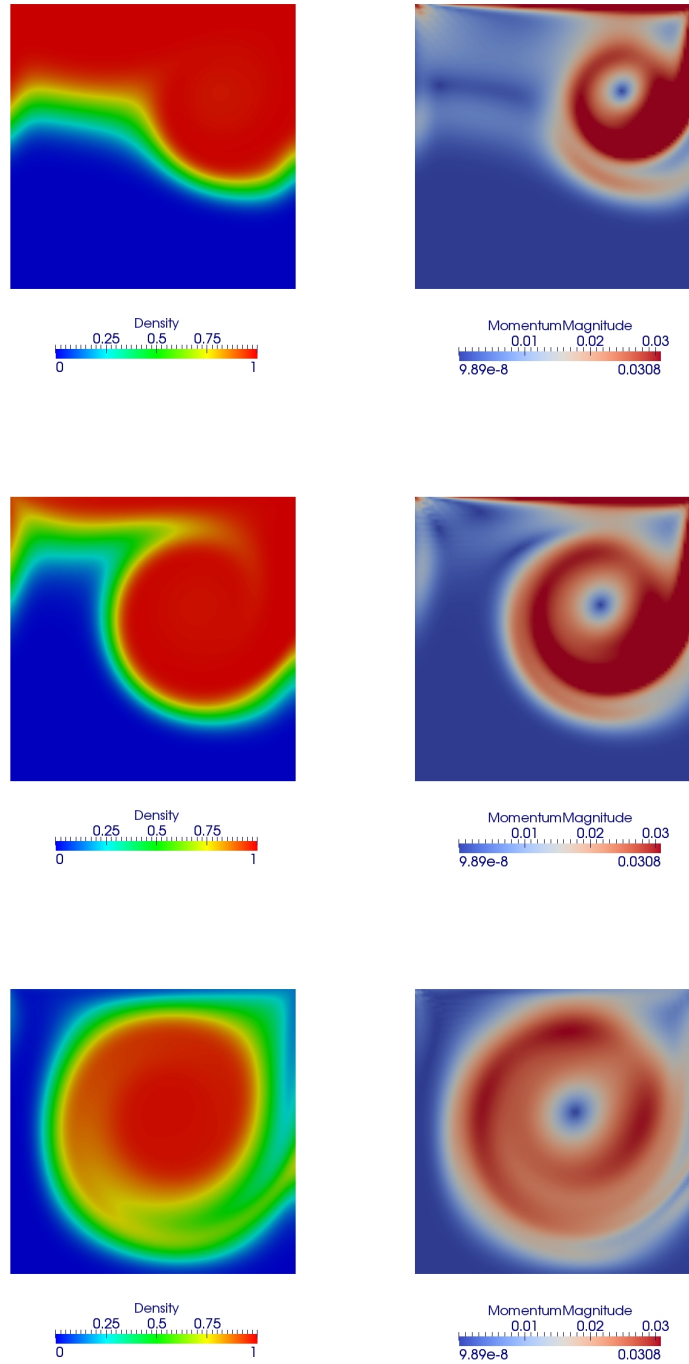


Figure 74: Fluid 1 results for a two-component immiscible fluid flow in a lid-driven cavity. Sequence of images shows flow progression from top to bottom corresponding respectively to early in the simulation to its final steady state.

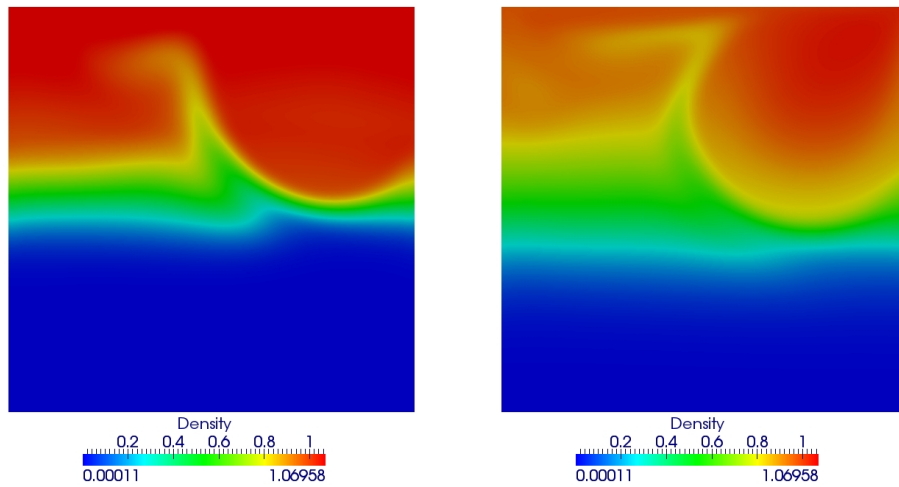


Figure 75: Fluid 1 results for a two-component immiscible fluid flow in a lid driven cavity. The higher viscosity and density of fluid 2 results in its confinement in the bottom-half of the cavity domain.

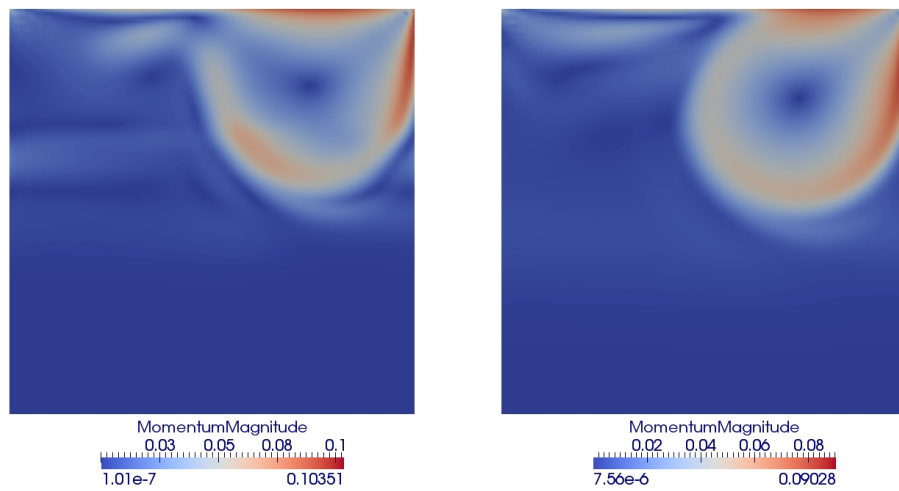


Figure 76: Fluid 1 results for a two-component immiscible fluid flow in a lid driven cavity. The higher viscosity and density of fluid 2 results in its confinement in the bottom-half of the cavity domain.

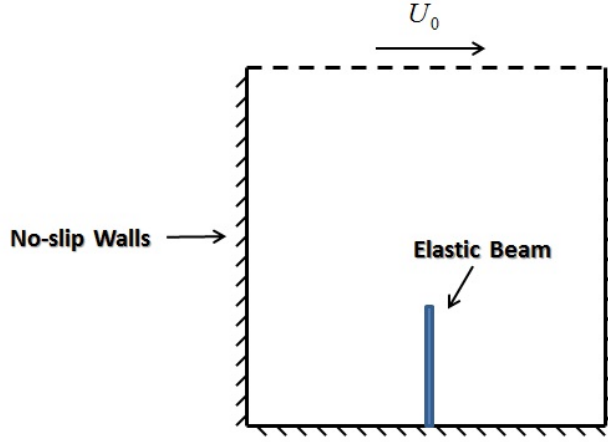


Figure 77: Schematic representation of a lid-driven cavity with an elastic beam attached to the lower surface.

The fluid parameters used for this simulation are identical to those used for Case 1 above. The fluids both have the same density and viscosity but a repellent interpartical potential promotes the immiscibility of the binary fluid. A single-component fluid simulation was carried out with the problem geometry and boundary conditions in order to develop some intuition for what flow conditions are expected within the cavity. The results of this computation are presented in Figure 78

The FSI tools and procedures were used as in the previous section with the modification that the fluid forces were computed as a sum of forces due to each fluid component. Similarly, the velocity boundary condition was inserted as a momentum input to both fluids using the moving surface boundary condition. As with the previous simulations, no accounting was made for material or geometric nonlinearities. Consequently, the simulation was arranged so that displacements would be small in comparison to the underlying discretization in both the fluid and solid domains.

The final momentum and density of fluid 1 is presented in Figure 79. As expected, the fluid initially in the upper half of the cavity—fluid 1—is ultimately concentrated in the

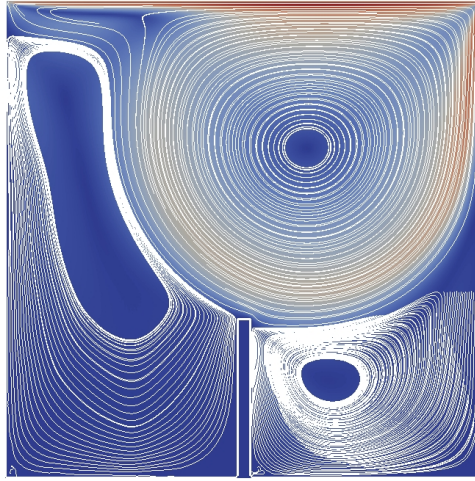


Figure 78: Single-component fluid flow in cavity with beam. Streamlines show development of three distinct vortex regions.

main vortex in the upper right-hand portion of the cavity. There is a smaller vortex region in the lower right corner where fluid 1 and fluid 2 circulate and mix. The large bean-shaped circulating region on the left portion of the cavity is a mixture of both fluids as well, with fluid 2 concentrating in the lower left region where it is trapped against the beam and the lower domain boundary.

The resulting displacement, velocity and acceleration of the beam tip is presented in Figure 80. A depiction of the final displacement of the entire beam is presented in Figure 81.

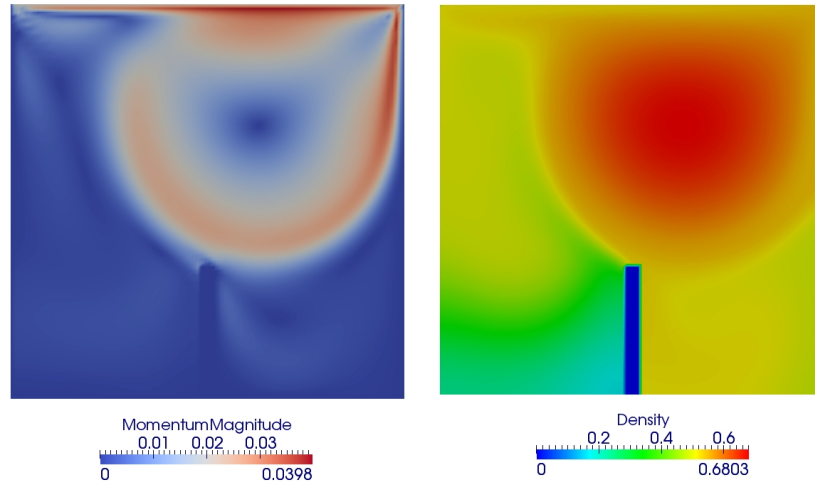


Figure 79: Momentum and density fields for fluid 1 at steady-state; $Re=1000$.

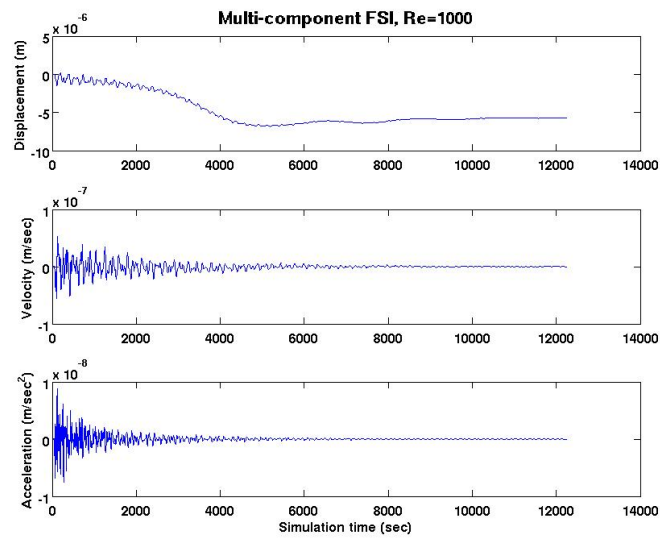


Figure 80: Plot of displacement, velocity and acceleration at the tip of the elastic beam.

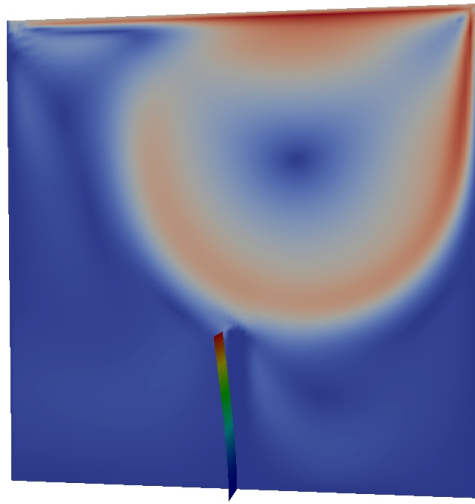


Figure 81: Final beam displacement for multi-component FSI. Beam displacement is magnified 10 times for clarity.

THIS PAGE INTENTIONALLY LEFT BLANK

VIII. CONCLUSIONS AND FUTURE WORK

A. CONCLUSIONS

The primary objective of this thesis is to investigate the use of LBM to model viscous incompressible flow and model the interactions that flow has with surrounding structures. In accomplishing this goal, several outcomes have been achieved:

1. A body of software has been developed to allow LBM modeling of single-component incompressible flow in two and three dimensions.
 - (a) This software was validated against a selection of two- and three-dimensional benchmark problems and shown to accurately model low and moderate Reynolds number fluid flows
 - (b) It was shown that the expected quadratic convergence properties of LBM can be lost for single-precision computations and a new mixed-precision implementation was demonstrated to extend the range of quadratic convergence at less computational expense than carrying out computations in full double precision.
 - (c) The software performance was compared to other single-GPU implementations reported in the recent literature and it was shown that the implementation presented for this thesis outperforms all others over certain problem sizes and is highly competitive for all problem sizes.
2. The LBM software tools were extended to incorporate structural interactions thus allowing FSI simulations.
 - (a) FSI simulations were demonstrated for both two- and three-dimensional single-component fluid flow problems.

- (b) A novel heterogeneous parallel implementation was described where task-level parallelism inherent in the FSI problem is parceled among both the CPU and GPU on a single workstation. It was shown that by decomposing the problem domain that performance can be improved by over 23 percent for some problems.
 - (c) A simple two-dimensional FSI simulation was presented for multi-component fluid flows.
3. A novel method for combining CLBM and FELBM into a HBLM was developed. This allows the efficient description of curved domain boundaries while minimizing the computational expense of FELBM.

B. FUTURE WORK

Much work remains to be done for future research in LBM for fluid flows. For single-component fluid flows, the software tools presented in this work only accommodate flows for Reynolds number up to approximately 10,000. Current research in entropic and thermal LBM along with single and multi-parameter turbulence models can be incorporated to extend the range of simulation up through at least the range of incompressible fluid flow. Further research needs to be done to include some capability for compressible flow modeling. Accomplishment of these goals will greatly expand the range of applicability of the LBM models presented here and open the door to a multitude of interesting research applications.

The multi-component fluid flow modeling capability is also in need of much work. Current implementations are restrictive in the range of fluid density and viscosity ratios that can be stably simulated. Additionally, more physical fidelity is required in the inter-particle potential modeling to allow predictive rather than merely qualitative simulations to be conducted.

For successful application of improved LBM models to more realistic problem types, the need exists to further extend the performance and scalability of the software

tools. As implemented for this work, excellent performance was obtained for software run on a single GPU or a small number of GPUs attached to a single workstation. The scaling achieved for multiple GPUs over multiple platforms was less well developed for this work. To accommodate future scaling, improved partitioning strategies must be included and incorporated into the software platform in a way that allows efficient scaling to an arbitrarily large set of computational resources. Additionally, software components such as solid modelers and mesh generators must be adopted and interfaced with existing tools to assist with LBM problem formulation and setup.

In order to employ lattice Boltzmann fluid models for future FSI research on more physically relevant problems, extensive work is also required for both the structural models as well as the LBM computational routines. Of highest priority for the structural model is the need to incorporate geometric and material non-linearity into the dynamic models. FSI problems of practical interest involve deformations that are *not* small and strains that *are* large. Consequently, linear elastic structural dynamics models are overly restrictive in the range of problems for which they will provide a satisfactory answer. Future research efforts will be directed towards meeting this need with a full range of non-linear material constitutive models and FEM technology to accommodate moving and deforming meshes. On the fluid modeling front, it is imperative that extensions be developed to admit moving solid boundaries that displace over an arbitrary number of lattice points. Methods must be implemented to properly initialize and update lattice points that are either entering or emerging a non-fluid domain. Alternately, non-classical LBM formulations such as FELBM and HLBM must be further developed so that both the fluid and solid domain can be consistently described in a Lagrangian manner within a given FSI simulation over a more broad range of problems.

THIS PAGE INTENTIONALLY LEFT BLANK

LIST OF REFERENCES

- [1] Z. Guo and T. S. Zhao, “Lattice Boltzmann model for incompressible flows through porous media,” *Phys. Rev. E*, vol. 66, p. 036304, Sep 2002.
- [2] G. H. Tang, W. Q. Tao, and Y. L. He, “Gas slippage effect on microscale porous flow using the lattice Boltzmann method,” *Phys. Rev. E*, vol. 72, p. 056301, Nov 2005.
- [3] M. Yoshino and T. Inamuro, “Lattice Boltzmann simulations for flow and heat/mass transfer problems in a three-dimensional porous structure,” *International Journal for Numerical Methods in Fluids*, vol. 43, no. 2, pp. 183–198, 2003.
- [4] T. Inamuro, T. Ogata, S. Tajima, and N. Konishi, “A lattice Boltzmann method for incompressible two-phase flows with large density differences,” *Journal of Computational Physics*, vol. 198, no. 2, pp. 628 – 644, 2004.
- [5] G. Hzi, A. R. Imre, G. Mayer, and I. Farkas, “Lattice Boltzmann methods for two-phase flow modeling,” *Annals of Nuclear Energy*, vol. 29, no. 12, pp. 1421–1453, 2002.
- [6] Y. Yan and Y. Zu, “A lattice Boltzmann method for incompressible two-phase flows on partial wetting surface with large density ratio,” *Journal of Computational Physics*, vol. 227, no. 1, pp. 763–775, 2007.
- [7] G. Breyiannis and D. Valougeorgis, “Lattice kinetic simulations in three-dimensional magnetohydrodynamics,” *Phys. Rev. E*, vol. 69, p. 065702, Jun 2004.
- [8] M. Pattison, K. Premnath, N. Morley, and M. Abdou, “Progress in lattice Boltzmann methods for magnetohydrodynamic flows relevant to fusion applications,” *Fusion Engineering and Design*, vol. 83, no. 4, pp. 557–572, 2008.
- [9] J. Carter and L. Oliker, “Performance evaluation of lattice-Boltzmann magnetohydrodynamics simulations on modern parallel vector systems,” in *High Performance Computing on Vector Systems* (M. Resch, T. Bnisch, K. Benkert, W. Bez, T. Furui, and Y. Seo, eds.), pp. 41–50, Springer Berlin Heidelberg, 2006.
- [10] B. H. Elton, “A lattice Boltzmann method for a two-dimensional viscous Burgers equation: Computational results.,” in *Supercomputing*, pp. 242–252, 1991.
- [11] G. Yan and J. Zhang, “A higher-order moment method of the lattice Boltzmann model for the Korteweg-de Vries equation,” *Math. Comput. Simul.*, vol. 79, pp. 1554–1565, January 2009.
- [12] N. S. Martys, “Improved approximation of the Brinkman equation using a lattice Boltzmann method,” *Phys. Fluids*, vol. 13, no. 6, pp. 1807–1810, 2001.

- [13] L. Zhong, S. Feng, P. Dong, and S. Gao, “Lattice Boltzmann schemes for the non-linear Schrödinger equation,” *Phys. Rev. E*, vol. 74, p. 036704, Sep 2006.
- [14] S. Chen and G. D. Doolen, “Lattice Boltzmann method for fluid flows,” *Annual Review of Fluid Mechanics*, vol. 30, no. 1, pp. 329–364, 1998.
- [15] C. K. Aidun and J. R. Clausen, “Lattice-Boltzmann method for complex flows,” *Annual Review of Fluid Mechanics*, vol. 42, no. 1, pp. 439–472, 2010.
- [16] R. Nourgaliev, T. Dinh, T. Theofanous, and D. Joseph, “The lattice Boltzmann equation method: theoretical interpretation, numerics and implications,” *International Journal of Multiphase Flow*, vol. 29, pp. 117–169, JAN 2003.
- [17] S. Wolfram, “Cellular automaton fluids 1: Basic theory,” *Journal of Statistical Physics*, vol. 45, pp. 471–526, 1986.
- [18] U. Frisch, B. Hasslacher, and Y. Pomeau, “Lattice-gas automata for the Navier-Stokes equation,” *Phys. Rev. Lett.*, vol. 56, pp. 1505–1508, Apr 1986.
- [19] S. Wolfram, *Theory and Applications of Cellular Automata*. Singapore: World Scientific Publication, 1986.
- [20] D. Helbing and M. Schreckenberg, “Cellular automata simulating experimental properties of traffic flow,” *Phys. Rev. E*, vol. 59, pp. R2505–R2508, Mar 1999.
- [21] J. Molofsky, “Population dynamics and pattern formation in theoretical populations,” *Ecology*, vol. 75, no. 1, pp. 30–39, 1994.
- [22] J. Huang, G. Narkounskaia, and D. L. Turcotte, “A cellular-automata, slider-block model for earthquakes ii. demonstration of self-organized criticality for a 2-d system,” *Geophysical Journal International*, vol. 111, no. 2, pp. 259–269, 1992.
- [23] G. R. McNamara and G. Zanetti, “Use of the Boltzmann equation to simulate lattice-gas automata,” *Phys. Rev. Lett.*, vol. 61, pp. 2332–2335, Nov 1988.
- [24] D. d’Humières, “Generalized lattice-Boltzmann equations,” in *Rarefied gas dynamics - Theory and simulations; Proceedings of the 18th International Symposium on Rarefied Gas Dynamics*, (University of British Columbia, Vancouver, Canada), July 1992.
- [25] P. Lallemand and L.-S. Luo, “Theory of the lattice Boltzmann method: Dispersion, dissipation, isotropy, Galilean invariance, and stability,” *Phys. Rev. E*, vol. 61, pp. 6546–6562, Jun 2000.
- [26] D. P. Ziegler, “Boundary conditions for lattice Boltzmann simulations,” *Journal of Statistical Physics*, vol. 71, pp. 1171–1177, 1993.

- [27] R. Mei, W. Shyy, D. Yu, and L.-S. Luo, "Lattice Boltzmann method for 3-D flows with curved boundary," *Journal of Computational Physics*, vol. 161, no. 2, pp. 680 – 699, 2000.
- [28] Y. W. Kwon, "Coupling of lattice Boltzmann and finite element methods for fluid-structure interaction application," *Journal of Pressure Vessel Technology*, vol. 130, no. 1, p. 011302, 2008.
- [29] J. Latt, B. Chopard, O. Malaspinas, M. Deville, and A. Michler, "Straight velocity boundaries in the lattice Boltzmann method," *Phys. Rev. E*, vol. 77, p. 056703, May 2008.
- [30] Q. Zou and X. He, "On pressure and velocity flow boundary conditions and bounce-back for the lattice Boltzmann BGK model," *Contributions to Mineralogy and Petrology*, pp. 11001–+, Nov. 1996.
- [31] J. Latt, *Hydrodynamic limit of lattice Boltzmann equations*. PhD dissertation, University of Geneva, 2007.
- [32] Q. Zou and X. He, "On pressure and velocity boundary conditions for the lattice Boltzmann BGK model," *Phys. Fluids*, vol. 9, June 1997.
- [33] D. Yu, R. Mei, L.-S. Luo, and W. Shyy, "Viscous flow computations with the method of lattice Boltzmann equation," *Progress in Aerospace Sciences*, vol. 39, no. 5, pp. 329 – 367, 2003.
- [34] B. F. Armaly, F. Durst, and J. C. F. Pereira, "Experimental and theoretical investigation of backward-facing step flow," *Journal of Fluid Mechanics*, vol. 127, pp. 473–496, 1983.
- [35] U. Ghia, K. Ghia, and C. Shin, "High-Re solutions for incompressible flow using the Navier-Stokes equations and a multigrid method," *Journal of Computational Physics*, vol. 48, no. 3, pp. 387 – 411, 1982.
- [36] O. Botella and R. Peyret, "Benchmark spectral results on the lid-driven cavity flow," *Computers and Fluids*, vol. 27, no. 4, pp. 421 – 433, 1998.
- [37] C.-H. Bruneau and M. Saad, "The 2D lid-driven cavity problem revisited," *Computers and Fluids*, vol. 35, no. 3, pp. 326 – 348, 2006.
- [38] H. Zhou, G. Mo, F. Wu, J. Zhao, M. Rui, and K. Cen, "GPU implementation of lattice Boltzmann method for flows with curved boundaries," *Computer Methods in Applied Mechanics and Engineering*, vol. 225228, no. 0, pp. 65 – 73, 2012.
- [39] W. Li, X. Wei, and A. Kaufman, "Implementing lattice Boltzmann computation on graphics hardware," *The Visual Computer*, vol. 19, pp. 444–456, 2003. 10.1007/s00371-003-0210-6.

- [40] D. Calhoun, “A Cartesian grid method for solving the two-dimensional streamfunction-vorticity equations in irregular regions,” *Journal of Computational Physics*, vol. 176, no. 2, pp. 231 – 275, 2002.
- [41] S. Xu and Z. J. Wang, “An immersed interface method for simulating the interaction of a fluid with moving boundaries,” *Journal of Computational Physics*, vol. 216, no. 2, pp. 454 – 493, 2006.
- [42] D. Russell and Z. J. Wang, “A Cartesian grid method for modeling multiple moving objects in 2D incompressible viscous flow,” *Journal of Computational Physics*, vol. 191, no. 1, pp. 177 – 205, 2003.
- [43] L. Ong and J. Wallace, “The velocity field of the turbulent very near wake of a circular cylinder,” *Experiments in Fluids*, vol. 20, pp. 441–453, 1996. 10.1007/BF00189383.
- [44] A. L. E. Silva, A. Silveira-Neto, and J. Damasceno, “Numerical simulation of two-dimensional flows over a circular cylinder using the immersed boundary method,” *Journal of Computational Physics*, vol. 189, no. 2, pp. 351 – 370, 2003.
- [45] C. Obrecht, F. Kuznik, B. Tourancheau, and J.-J. Roux, “A new approach to the lattice Boltzmann method for graphics processing units,” *Computers and Mathematics with Applications*, vol. 61, no. 12, pp. 3628 – 3638, 2011.
- [46] J. Tölke, “Implementation of a lattice Boltzmann kernel using the compute unified device architecture developed by NVIDIA,” *Comput. Vis. Sci.*, vol. 13, pp. 29–39, Nov. 2009.
- [47] P. Bailey, J. Myre, S. Walsh, D. Lilja, and M. Saar, “Accelerating lattice Boltzmann fluid flow simulations using graphics processors,” in *Parallel Processing, 2009. ICPP '09. International Conference on*, pp. 550 –557, sept. 2009.
- [48] M. Bernaschi, M. Fatica, S. Melchionna, S. Succi, and E. Kaxiras, “A flexible high-performance lattice Boltzmann GPU code for the simulations of fluid flows in complex geometries,” *Concurr. Comput. : Pract. Exper.*, vol. 22, pp. 1–14, Jan. 2010.
- [49] P. Rinaldi, E. Dari, M. Vnere, and A. Clausse, “A lattice-Boltzmann solver for 3D fluid simulation on GPU,” *Simulation Modelling Practice and Theory*, vol. 25, no. 0, pp. 163 – 171, 2012.
- [50] M. Astorino, J. B. Sagredo, and A. Quarteroni, “A modular lattice Boltzmann solver for GPU computing processors,” Tech. Rep. MATHICSE-TR-06-2011, Mathematics Institute of Computational Science and Engineering, Lucerne, Switzerland, July 2011.

- [51] K. Mattila, J. Hyvluoma, J. Timonen, and T. Rossi, “Comparison of implementations of the lattice-Boltzmann method,” *Computers and Mathematics with Applications*, vol. 55, no. 7, pp. 1514 – 1524, 2008.
- [52] NVIDIA Corporation, *NVIDIA CUDA C Programming Guide*, 4.2 ed., April 2012.
- [53] V. W. Lee, C. Kim, J. Chhugani, M. Deisher, D. Kim, A. D. Nguyen, N. Satish, M. Smelyanskiy, S. Chennupati, P. Hammarlund, R. Singhal, and P. Dubey, “Debunking the 100x GPU vs. CPU myth: an evaluation of throughput computing on CPU and GPU,” *SIGARCH Comput. Archit. News*, vol. 38, pp. 451–460, June 2010.
- [54] W. H. D.B. Kirk, *Programming Massively Parallel Processors: A Hands-on Approach*. Burlington, MA: Morgan Kaufmann, 2010.
- [55] E. K. J. Sanders, *CUDA by Example: An Introduction to General-Purpose GPU Programming*. Burlington, MA: Morgan Kaufmann, 2010.
- [56] R. Farber, *CUDA Application Design and Development*. Burlington, MA: Morgan Kaufmann, 2011.
- [57] NVIDIA Corporation, *CUDA C Best Practice Guide*, 4.0 ed., May 2011.
- [58] A. Caiazzo, “Analysis of lattice Boltzmann initialization routines,” *Journal of Statistical Physics*, vol. 121, pp. 37–48, 2005.
- [59] J. Hao and L. Zhu, “A lattice Boltzmann based implicit immersed boundary method for fluidstructure interaction,” *Computers and Mathematics with Applications*, vol. 59, no. 1, pp. 185 – 193, 2010.
- [60] Y. Cheng and H. Zhang, “Immersed boundary method and lattice Boltzmann method coupled FSI simulation of mitral leaflet flow,” *Computers and Fluids*, vol. 39, no. 5, pp. 871 – 881, 2010.
- [61] L. Zhu, G. He, S. Wang, L. Miller, X. Zhang, Q. You, and S. Fang, “An immersed boundary method based on the lattice Boltzmann approach in three dimensions, with application,” *Comput. Math. Appl.*, vol. 61, pp. 3506–3518, June 2011.
- [62] C. S. Peskin, “The immersed boundary method,” *Acta Numerica*, vol. 11, pp. 479–517, 2002.
- [63] H. Luo, R. Mittal, X. Zheng, S. A. Bielałowicz, R. J. Walsh, and J. K. Hahn, “An immersed-boundary method for flow-structure interaction in biological systems with application to phonation,” *J. Comput. Phys.*, vol. 227, pp. 9303–9332, Nov. 2008.

- [64] D. R. J. Owen, C. R. Leonardi, and Y. T. Feng, "An efficient framework for fluid-structure interaction using the lattice Boltzmann method and immersed moving boundaries," *International Journal for Numerical Methods in Engineering*, vol. 87, no. 1-5, pp. 66–95, 2011.
- [65] N. N-Q, "Sedimentation of hard-sphere suspensions at low Reynolds number," *Journal of Fluid Mechanics*, vol. 525, pp. 73–104, 2005.
- [66] Z.-G. Feng and E. E. Michaelides, "Proteus: a direct forcing method in the simulations of particulate flows," *Journal of Computational Physics*, vol. 202, no. 1, pp. 20–51, 2005.
- [67] Y. T. Feng, K. Han, and D. R. J. Owen, "Coupled lattice Boltzmann method and discrete element modelling of particle transport in turbulent fluid flows: Computational issues," *International Journal for Numerical Methods in Engineering*, vol. 72, no. 9, pp. 1111–1134, 2007.
- [68] O. C. Zienkiewicz, D. K. Paul, and E. Hinton, "Cavitation in fluid-structure response (with particular reference to dams under earthquake loading)," *Earthquake Engineering and Structural Dynamics*, vol. 11, no. 4, pp. 463–481, 1983.
- [69] R. Newton, "Finite element study of shock induced cavitation," in *ACSE Spring Conference*, (Portland, OR), 1980.
- [70] Y. Kwon and P. M. McDermott, "Effects of void growth and nucleation on plastic deformation of plates subjected to fluid-structure interaction," *ASME J. of Pressure Vessel Technol.*, vol. 123, pp. 480–485, 2001.
- [71] X. He and G. D. Doolen, "Lattice Boltzmann method on a curvilinear coordinate system: Vortex shedding behind a circular cylinder," *Phys. Rev. E*, vol. 56, pp. 434–440, Jul 1997.
- [72] A. Ladd, "Numerical simulations of particulate suspensions via a discretized Boltzmann equation part ii. numerical results," Tech. Rep. UCRL-JC-113349, Lawrence Livermore National Laboratory, June 1993.
- [73] Y. Kwon and H. Bang, *The Finite Element Method Using MATLAB*. New York, New York: CRC Press, 2000.
- [74] Y. W. Kwon and J. C. Jo, "Development of weighted residual based lattice Boltzmann techniques for fluid-structure interaction application," *Journal of Pressure Vessel Technology*, vol. 131, no. 3, p. 031304, 2009.

- [75] S. Turek and J. Hron, “Proposal for numerical benchmarking of fluid-structure interaction between an elastic object and laminar incompressible flow,” in *Fluid-Structure Interaction* (H.-J. Bungartz, M. Schfer, T. J. Barth, M. Griebel, D. E. Keyes, R. M. Nieminen, D. Roose, and T. Schlick, eds.), vol. 53 of *Lecture Notes in Computational Science and Engineering*, pp. 371–385, Springer Berlin Heidelberg, 2006.
- [76] H. Bai, P. Yu, S. H. Winoto, and H. T. Low, “Lattice Boltzmann method for flows in porous and homogenous fluid domains coupled at the interface by stress jump,” *International Journal for Numerical Methods in Fluids*, vol. 60, no. 6, pp. 691–708, 2009.
- [77] M. E. McCracken and J. Abraham, “Multiple-relaxation-time lattice-Boltzmann model for multiphase flow,” *Phys. Rev. E*, vol. 71, p. 036701, Mar 2005.
- [78] A. S. Joshi and Y. Sun, “Multiphase lattice Boltzmann method for particle suspensions,” *Phys. Rev. E*, vol. 79, p. 066703, Jun 2009.
- [79] X. Shan and H. Chen, “Lattice Boltzmann model for simulating flows with multiple phases and components,” *Phys. Rev. E*, vol. 47, pp. 1815–1819, Mar 1993.
- [80] G. Peng, H. Xi, C. Duncan, and S.-H. Chou, “Finite volume scheme for the lattice Boltzmann method on unstructured meshes,” *Phys. Rev. E*, vol. 59, pp. 4675–4682, Apr 1999.
- [81] Z. Guo and T. S. Zhao, “Explicit finite-difference lattice Boltzmann method for curvilinear coordinates,” *Phys. Rev. E*, vol. 67, p. 066709, Jun 2003.
- [82] V. Sofonea, A. Lamura, G. Gonnella, and A. Cristea, “Finite-difference lattice Boltzmann model with flux limiters for liquid-vapor systems,” *Phys. Rev. E*, vol. 70, p. 046702, Oct 2004.
- [83] S. Succi, O. Filippova, G. Smith, and E. Kaxiras, “Applying the lattice Boltzmann equation to multiscale fluid problems,” *Computing in Science Engineering*, vol. 3, pp. 26–37, nov/dec 2001.
- [84] Y. Li, E. J. LeBoeuf, and P. K. Basu, “Least-squares finite-element lattice Boltzmann method,” *Phys. Rev. E*, vol. 69, p. 065701, Jun 2004.
- [85] M. Min and T. Lee, “A spectral-element discontinuous Galerkin lattice Boltzmann method for nearly incompressible flows,” *Journal of Computational Physics*, vol. 230, no. 1, pp. 245–259, 2011.
- [86] X. Shi, J. Lin, and Z. Yu, “Discontinuous Galerkin spectral element lattice Boltzmann method on triangular element,” *International Journal for Numerical Methods in Fluids*, vol. 42, no. 11, pp. 1249–1261, 2003.

- [87] A. Dster, L. Demkowicz, and E. Rank, “High-order finite elements applied to the discrete Boltzmann equation,” *International Journal for Numerical Methods in Engineering*, vol. 67, no. 8, pp. 1094–1121, 2006.
- [88] A. K. Gunstensen, D. H. Rothman, S. Zaleski, and G. Zanetti, “Lattice Boltzmann model of immiscible fluids,” *Phys. Rev. A*, vol. 43, pp. 4320–4327, Apr 1991.
- [89] X. Shan and G. Doolen, “Multicomponent lattice-boltzmann model with interparticle interaction,” *Journal of Statistical Physics*, vol. 81, pp. 379–393, 1995.
- [90] M. R. Swift, E. Orlandini, W. R. Osborn, and J. M. Yeomans, “Lattice boltzmann simulations of liquid-gas and binary fluid systems,” *Phys. Rev. E*, vol. 54, pp. 5041–5052, Nov 1996.
- [91] X. He, X. Shan, and G. D. Doolen, “Discrete Boltzmann equation model for nonideal gases,” *Phys. Rev. E*, vol. 57, pp. R13–R16, Jan 1998.
- [92] D. H. Rothman and J. M. Keller, “Immiscible cellular-automaton fluids,” *Journal of Statistical Physics*, vol. 52, pp. 1119–1127, 1988.
- [93] J. I. Q. Chang and D. Alexander, *Application of Lattice Boltzmann Method, Thermal Multiphase Fluid Dynamics*. Saarbrücken, Germany: Verlag Dr. Müller, 2000.
- [94] J. Kahn and J. E. Hilliard, “Free energy of a nonuniform system. i. interfacial free energy,” *J. Chem. Phys.*, vol. 28, 1958.
- [95] X. Nie, Y.-H. Qian, G. D. Doolen, and S. Chen, “Lattice Boltzmann simulation of the two-dimensional Rayleigh-Taylor instability,” *Phys. Rev. E*, vol. 58, pp. 6861–6864, Nov 1998.
- [96] N. Takada, M. Misawa, A. Tomiyama, and S. Hosokawa, “Simulation of bubble motion under gravity by lattice Boltzmann method,” *J. Nucl. Sci. Technol.*, vol. 38, p. 330, 2001.
- [97] G. G. A. Lamura and J. Yeomans, “A lattice Boltzmann model of ternary fluid mixtures,” *Europhysics Letters*, vol. 45, 1999.
- [98] P. L. Bhatnagar, E. P. Gross, and M. Krook, “A model for collision processes in gases. i. small amplitude processes in charged and neutral one-component systems,” *Phys. Rev.*, vol. 94, pp. 511–525, May 1954.
- [99] J. Rowlinson and B. Widom, *Molecular Theory of Capillarity*. Dover Books on Chemistry, Mineola, New York: Dover Publications, 2003.
- [100] J. Sethian, *Level Set methods and Fast Marching Methods: Evolving Interfaces in Computational Geometry, Fluid Mechanics, Computer Vision and Materials Sciences*. Cambridge, England: Cambridge University Press, 1999.

- [101] C. Hirt and B. Nichols, “Volume of fluid (VOF) method for the dynamics of free boundaries,” *Journal of Computational Physics*, vol. 39, no. 1, pp. 201 – 225, 1981.
- [102] X. He, S. Chen, and R. Zhang, “A lattice Boltzmann scheme for incompressible multiphase flow and its application in simulation of RayleighTaylor instability,” *Journal of Computational Physics*, vol. 152, no. 2, pp. 642 – 663, 1999.
- [103] X. H. et al., “On the three-dimensional Rayleigh-Taylor instability,” *Phys. Fluids*, vol. 11, no. 5, 1999.

THIS PAGE INTENTIONALLY LEFT BLANK

INITIAL DISTRIBUTION LIST

1. Defense Technical Information Center
Ft. Belvoir, Virginia
2. Dudley Knox Library
Naval Postgraduate School
Monterey, California
3. Dr. Young Kwon
Naval Postgraduate School
Monterey, California
4. Dr. Garth Hobson
Naval Postgraduate School
Monterey, California
5. Dr. Josh Gordis
Naval Postgraduate School
Monterey, California
6. Dr. Francis Giraldo
Naval Postgraduate School
Monterey, California
7. Dr. Clyde Scandrett
Naval Postgraduate School
Monterey, California